NTNU – Trondheim
Norwegian University of
Science and Technology

Rapid Directional Recrystallisation of SiGe Fibres

David Andre Coucheron

Nanotechnology
Submission date: June 2015
Supervisor: Ursula Gibson, IFY

Norwegian University of Science and Technology
Department of Physics

Abstract

Recrystallisation of molten-core drawn SiGe fibres with inhomogeneous composition was performed by two different techniques: Slow cooling in a tube furnace and travelling melt zone recrystallisation by a CO_2 laser. Two different cooling rates of 1.5 °C min^{-1} and 5 °C min^{-1} were used in the tube furnace with both horizontal and vertical sample placement. Homogeneous and inhomogeneous composition were found by scanning electron microscopy in cross-sections for both cooling rates, with no apparent trends on resulting Ge distribution based on cooling rate and sample placement. For CO_2 laser annealing, two different composition fibres ($\approx 5at\%$ and $\approx 40at\%$ Ge) with core diameters of approximately 105 µm and 210 µm, respectively, were treated at several scan velocities. The experimentally determined critical growth velocity for homogeneous growth for the large core fibres were in good agreement with the theoretically calculated value of 348.23 µm s^{-1} for the low Ge content sample and 29.4 µm s^{-1} for the high Ge content. Redrawn fibres with a core diameter of approximately 8 µm were also tested for both composition, and by reducing the fibre diameter the critical growth rate was increased by up to a magnitude ≈ 10. For the redrawn low Ge content fibres, homogeneous fibres were produced at a rates as high as 1000 µm s^{-1}. Similar radius fibres of higher Ge content were of homogeneous composition at rates of 100 µm s^{-1}, but inhomogeneous at 1000 µm s^{-1}. Investigation by electron backscattered diffraction was performed on cross-sections of an untreated sample, an inhomogeneous tube-furnace annealed with very abrupt compositional changes, and a homogeneous CO_2 laser annealed sample. The entire cross-sections were determined to be single crystalline, even for the untreated sample with severe compositional inhomogeneity. X-ray tomography measurements confirmed that the entire CO_2 laser annealed regions were homogeneous, and preliminary X-ray diffraction results indicate that the entire region is single crystalline as well. µ-Raman mapping was performed on the same samples, revealing strain associated to the high Ge-content areas of inhomogeneous, untreated fibres, but no strain in the treated samples, homogeneous and inhomogeneous alike.

Sammendrag

Fibre av SiGe fremstilt ved flytende kjerne-trekking har blitt rekrystallisert ved bruk av to forskjellige teknikker: Sakte kjøling i en tubeovn og bevegende smeltesone-rekrystallisering med en CO_2-laser. To forskjellige kjølerater, 1.5 og $5\,^{\circ}\mathrm{C}\,\mathrm{min}^{-1}$, ble testet i tubeovnen med både vertikal og horisontal prøveplassering. Homogen og inhomogen komposisjon ble observert med sveipeelektronmikroskopi i tverrsnitter av prøvene fra begge kjølerater, men ingen åpenbare trender mellom Ge-distribusjon og prøveplassering ble funnet. Fibre av to forskjellige komposisjoner ($\approx 5at\%$ og $\approx 40at\%$ Ge) ble behandlet med CO_2-laseren ved forskjellige skannehastigheter. De eksperimentelt bestemte kritiske vekstratene for homogen vekst i fibrene med stor kjerne, var i god overenstemmelse med de teoretisk beregnede verdiene: $348.23\,\mu\mathrm{m}\,\mathrm{s}^{-1}$ for prøvene med lite Ge og $29.4\,\mu\mathrm{m}\,\mathrm{s}^{-1}$ for prøvene med mye Ge. Omdratte fibre med en radius på omtrent $8\,\mu\mathrm{m}$ ble også testet for begge komposisjoner og en økning i kritisk veksthastighet med opp til ≈ 10 ganger ble funnet ved reduksjon i fiberdiameteren for begge komposisjoner. For de omdratte fibrene med lite Ge ble det rekrystallisert homogene fibre ved hastigheter opp til og med $1000\,\mu\mathrm{m}\,\mathrm{s}^{-1}$. De omdratte fibrene med mye Ge var homogene opp til $100\,\mu\mathrm{m}\,\mathrm{s}^{-1}$, men inhomogene ved $1000\,\mu\mathrm{m}\,\mathrm{s}^{-1}$ Krystalliniteten til én ubehandlet prøve, én inhomogen tubeovnbehandlet prøve og én homogen laserbehandlet prøve ble undersøkt med tilbakespredt elektrondiffraksjon. Tverrsnittene til de tre prøvene var alle nkrystallinske, selv prøvene med store komposisjonsvariasjoner. Røntgentomografi bekrefter at CO_2-laserbehandlede prøver var av homogen komposisjon over hele det behandle område og foreløpige røntgendiffraksjonsresultater antyder at hele området er en énkrystall. Kartlegging av spenning ved µ-Ramanspektroskopi fant spenning tilknyttet de Ge-rike områdene i den ubehandlede prøven, men ingen spenning i verken de homogene eller inhomogene behandlede prøvene.

Preface

This master's thesis was written as the conclusion of my master's degree in nanotechnology at the Norwegian University of Science and Technology, NTNU. The thesis work was done at the Department of Physics during the spring of 2015 under the supervision of professor Ursula Gibson. I would like to extend my sincere gratitude to Ursula Gibson for her support and enthusiasm with the project, as well as her knowledge and experimental help.

I would also like to thank assistant professor Michael Fokine at KTH, Stockholm, for letting me visit and assisting tirelessly with the use of his laser set-up for the recrystallisation experiments. Professor Dag W. Breiby, Dr. Nilesh Patil and engineer Ole Tore Buset are acknowledged for assisting with x-ray measurements and their interest in the experiments. Most of the characterisation was performed at NTNU NanoLab and the staff is greatly acknowledged for their assistance. Also, the Research Council of Norway is acknowledged for the support to NTNU NanoLab through the Norwegian Micro- and Nano-Fabrication Facility, NorFab (197411/V30). Finally, I would like to thank Fredrik Martinsen and Benjamin Smeltzer for their experimental assistance and theoretical input.

Contents

1 Introduction **1**

2 Theory and Background **5**
- 2.1 Solidification . . . 6
  - 2.1.1 Phase Transformations . . . 6
  - 2.1.2 Thermodynamic and Kinetic Treatment of Nucleation . . . 8
  - 2.1.3 Crystal Growth . . . 11
    - 2.1.3.1 Undercooling and Supersaturation . . . 11
    - 2.1.3.2 Directional Solidification . . . 12
    - 2.1.3.3 Interface Stability . . . 15
    - 2.1.3.4 Critical Growth Velocity . . . 16
    - 2.1.3.5 Solidification Structure . . . 17
  - 2.1.4 Growth of Si_xGe_{1-x} . . . 18
    - 2.1.4.1 Slow Freezing . . . 19
    - 2.1.4.2 Czochralski . . . 20
    - 2.1.4.3 Bridgeman . . . 20
    - 2.1.4.4 Other Growth Methods . . . 20
  - 2.1.5 Recrystallisation Techniques . . . 21
    - 2.1.5.1 Slow Freezing With Homogeneous Cooling . . . 21
    - 2.1.5.2 Zone Melting . . . 21
- 2.2 Characterisation Techniques . . . 22
  - 2.2.1 Scanning Electron Microscope (SEM) . . . 22
    - 2.2.1.1 Electrons and Matter . . . 22
    - 2.2.1.2 Scanning Electron Microscope Instrumentation . . . 28
    - 2.2.1.3 Electron Dispersive X-Ray Spectroscopy (EDS) . . . 30
    - 2.2.1.4 Electron Backscatter Diffraction (EBSD) . . . 31
  - 2.2.2 X-ray Tomography (XRT) . . . 31
    - 2.2.2.1 X-rays and Matter . . . 32

2.2.2.2 XRT Working Principles 33
2.2.3 µ-Raman 34
2.2.3.1 The Origin of Molecular Vibrations 34
2.2.3.2 The Raman Effect 35
2.2.3.3 Raman Spectroscopy 37

3 Experimental Methods 39
3.1 Fibre Drawing 39
3.1.1 Samples Overview and Nomenclature 39
3.1.2 Clemson Fibres 40
3.1.3 NTNU Fibres 42
3.2 Heat Treatments 45
3.2.1 Tube Furnace 45
3.2.2 CO$_2$-laser 46
3.3 Characterisation Techniques 49
3.3.1 Sample Preparation 49
3.3.2 SEM+EDS 49
3.3.3 Electron Backscattered Diffraction 50
3.3.4 X-Ray Tomography 51
3.3.5 µ-Raman 51
3.3.5.1 Experimental Procedure 51
3.3.5.2 Strain-analysis by µ-Raman 51
3.3.5.3 Standards 53
3.3.5.4 Strain Calibration in SiGe 55
3.3.5.5 Spot Size Measure 56
3.4 Data Analysis 57
3.4.1 Compositional Analysis 57
3.4.1.1 Examples 59
3.4.2 Peak Fitting 60

4 Results and Discussion 63
4.1 Compositional Distribution 63
4.1.1 Tube-Furnace 65
4.1.1.1 Program A - Slow Cooling 65
4.1.1.2 Program B - Fast Cooling 66
4.1.1.3 Discusison 67
4.1.2 CO$_2$-Laser 70
4.1.2.1 CAL 70

4.1.2.2 CRL 74
4.1.2.3 NAL 75
4.1.2.4 NRL 75
4.1.3 Calculated Critical Velocity 79
4.1.3.1 Clemson Cane 79
4.1.3.2 NAL 84
4.1.3.3 Error in Calculations 85
4.1.4 Discussion 85
4.2 EDS analysis 88
4.3 Crystallinity 91
4.3.1 Untreated Sample 91
4.3.2 CAO2B 92
4.3.3 CAL100-2 92
4.3.4 Recrystallisation Effect on Crystallinity 92
4.4 Strain 93
4.4.1 Untreated Sample 94
4.4.2 CAO2B 98
4.4.3 CAL100-2 100
4.4.4 Strain Reduction 100

5 Conclusion 103

Appendices

A MatLab Code 115
A.1 Analysis.m 115
A.2 BlackBody.m 123

B SEM Images 127
B.1 Tube Furnace Annealed 127
B.1.1 CAO1 127
B.1.2 CAO2 127
B.1.3 CAO3 128
B.1.4 CAO4 129
B.1.5 CAL 130
B.2 NRL 130

C EDS Quantification Area Error 133

D Critical Velocity of NAL **135**

List of Figures

1.1 Plot of resulting composition for several experimentally grown SiGe crystals, based on growth velocity and Ge-content. 3

2.1 Graph illustrating the free energy a solid and a liquid phase with respect to temperature. 6
2.2 A simple isomorphous alloy phase diagram. 7
2.3 Total free energy change for formation of a nucleus with respect to the nucleus radius. 9
2.4 Distribution coefficient illustrated in a binary alloy. 12
2.5 Distribution of solute in when crystallisation occurs in equilibrium (a) and at an faster rate (b). 13
2.6 Illustration of solute concentration in a growing solid and the liquid . 14
2.7 Schematic of a solid rod after directional solidification, with a graph illustrating the concentration profile along the rod. 15
2.8 Transition between different growth structures depending on $\frac{\nabla T}{V}$ and solute concentration (C_0). 17
2.9 Schematic illustration showing the resulting solidification structure depending on thermal gradient across the growth interface. 18
2.10 Phase diagram of SiGe. 19
2.11 Schematic of zone melting by translating heaters. 22
2.12 Schematic of the interaction volume of the primary electrons. 24
2.13 Kinetic energy distribution of electrons escaping the sample. 25
2.14 Illustration of different scattering events in a material. 26
2.15 Illustration of BSE yield and SE yield as a function of atomic number. 27
2.16 X-Ray spectrum captured by EDS for SiGe. 28
2.17 Schematic overview of the image generation in an SEM. 29
2.18 Kikuchi pattern from an untreated SiGe fibre. 32
2.19 A typical XRT set-up with a rotating sample stage. 34

2.20 Absorption of a laser photon and the three relaxation types relevant for Raman spectroscopy. 37

3.1 BSE SEM image of the untreated CA cross-section used for EDS analysis (a) and the resulting spectrum (b). 40
3.2 BSE SEM micrograph of a representative untreated section of a CA fibre and EDS elemental maps. 41
3.3 Cross-sectional LA-BSE micrograph of a clemson fibre redrawn into a quartz capillary. 42
3.4 BSE SEM micrograph of a reresentative untreated section of a NA fibre and corresponding elemental EDS maps. 44
3.5 Cross-sectional micrograph of an NR fibre. 44
3.6 Temperature profiles for program A (a) and program B (b). 46
3.7 Schematic of the different sample placements on the ceramic boat for the tube furnace experiments. 47
3.8 Schematic of the annealing set-up for travelling zone recrystallisation by use of a CO_2 laser. 48
3.9 Image captured using the camera in the CO_2 set-up. 49
3.10 Raman spectrum of a SiGe sample. 52
3.11 Raman spectra for the pure Ge window and pure Ge fibre. 54
3.12 Raman spectra for the pure Si window and pure Si fibre. 54
3.13 Image of the quantified region of sample CAL100-1 used for strain calibration (a) and the corresponding EDS spectrum (b). 55
3.14 Raman spectrum for the CAL100-1 sample (blue) and a fitted curve (red). 56
3.15 Phase diagram of SiGe 57
3.16 Cropped and blurred image of untreated fibre input into *Anaylysis.m* (a) and the detected edge and centre (b). 58
3.17 BSE SEM micrographs of an untreated sample (a), an inhomogeneous treated sample (b) and a homogeneous treated sample (c). 60
3.18 Radial (a) and angular (b) distribution for the three examples presented in figure 3.17. 61

4.1 XRT slice of an untreated CA fibre. 64
4.2 XRT slice of an untreated SiGe fibre with $20at\%$ Ge. 64
4.3 Radial (a) and angular (b) distribution of Ge in batch CAO1. 65
4.4 Radial (a) and angular (b) distribution of Ge in batch CAO2. 66
4.5 Radial (a) and angular (b) distribution of Ge in batch CAO3. 67
4.6 Radial (a) and angular (b) distribution of Ge in batch CAO4. 67

4.7 Radial (a) and angular (b) SLS versus cooling rate for all tube-furnace annealed sample. 68
4.8 BSE SEM micrographs of samples CAO1R (a), CAO1RC (b), CAO2B (c) and CAO3B (d). 69
4.9 BSE SEM micrographs from the sample CAO4B, separated by approximately 400 µm. 70
4.10 Radial (a) and angular (b) distribution of Ge for samples CAL10-1, CAL100-1 and CAL1000-1. 71
4.11 Radial (a) and angular (b) distribution of Ge for samples CAL10-2, CAL50-1, CAL100-2 and CAL3000. All samples are homogeneous, except for CAL3000-1. 71
4.12 Radial (a) and angular (b) SLS for the CAL samples. 72
4.13 BSE SEM micrograph of the samples CAL200-1 and CAL1000-1. . . 73
4.14 XRT slice of the sample CRL2, placed on top of the untreated standard. 73
4.15 LA-BSE SEM micrographs of an untreated CR sample (a), CRL10 (b), CRL100 (c) and CRL1000 (d). 74
4.16 Cross-sectional BSE image of NAL10 (a) and NAL100(B). 75
4.17 Images captured during laser annealing of the sample NAL10. 76
4.18 Radial (a) and angular (b) distribution of the NRL samples. 77
4.19 SLS for the radial (a) and angular (b) distribution of Ge in batch NRL. 77
4.20 LA-BSE SEM micrographs of the samples NRL100 (a) and NRL1000 (b). 78
4.21 Image showing melt zone in the CAL100-2 sample. 79
4.22 Cross-section of CAL100-2 with EDS quantification area marked by yellow circle (a) and the corresponding EDS spectrum (b). 80
4.23 514 nm-Filtered image of the melt zone in the fibre (a) and greyscale intensity plot (b) along the red line in image (a). 81
4.24 635 nm-Filtered image of the melt zone in the fibre (a) and greyscale intensity plot (b) along the red line in image (a). 82
4.25 Comparison of the greyscale profile of the melt zone using a 635 nm filter (a) and the unfiltered melt zone (b). 83
4.26 Unfiltered image of the melt zone in fibre NAL10 (a) and the greyscale intensity plot (b) along the red line in image (a). 84
4.27 BSE SEM micrograph of the untreated CA smaple, with the area investigated by EBSD marked by the yellow rectangle (a) and a microstructural map captured by EBSD (b). 91

4.28 BSE SEM micrograph the CAO2B sample, with the area investigated by EBSD marke in yellow (a) and a microstructural map captured by EBSD (b). 92
4.29 BSE SEM micrograph the CAL100-2 sample, with the area investigated by EBSD marke in yellow (a) and a microstructural map captured by EBSD (b). 93
4.30 BSE SEM micrograph of line scanned by µ-Raman for an untreated sample. 94
4.31 Raman spectra for the line scan marked in figure 4.30. 96
4.32 Peak fitted spectrum from the initial Ge-rich section in the line scan of the untreated CA sample. 97
4.33 Micrograph of the CAO2B sample, with the line scanned with µ-Raman marked by the red arrow. The scan covers three regions of different composition. 98
4.34 Plots of the shift, integrated area and FWHM of the Si−Si peak of the spectra from the scanned line in 4.34. 99
4.35 BSE SEM image of a homogeneous sample (a), and with a Raman mapping layered on top of the SEM image (b). 100

B.1 BSE SEM micrograph of a reresentative untreated section of clemson fibre (a) and corresponding elemental EDS maps. 127
B.2 BSE SEM micrograph of a reresentative untreated section of clemson fibre (a) and corresponding elemental EDS maps. 128
B.3 BSE SEM micrograph of a reresentative untreated section of clemson fibre (a) and corresponding elemental EDS maps. 128
B.4 BSE SEM micrograph of a reresentative untreated section of clemson fibre (a) and corresponding elemental EDS maps. 129
B.5 BSE SEM micrograph of a reresentative untreated section of clemson fibre (a) and corresponding elemental EDS maps. 130
B.6 BSE SEM micrograph of a reresentative untreated section of clemson fibre (a) and corresponding elemental EDS maps. 131

C.1 BSE SEM micrographs of samples A (a), B (b) and C (c) with quantification area used in EDS marked by the yellow circles. 134

D.1 Baseline corrected greyscale intensity plot across melt zone of the NAL sample. 135

List of Tables

3.1 Composition of Clemson fibres. 41
3.2 Parameters used for the production of the source alloy used for drawing of the NA fibres. 43
3.3 Composition of an NTNU drawn fibre. 43
3.4 Summary of the two different heating procedure used in the tube-furnace. The time is how long spent from steps $i-1$ and i. 46
3.5 Summary of the different scan velocities tested for the different samples. Each velocity tested will be marked by the sample name, and velocities not tested are marked by ”-”. 48
3.6 Peak position and FWHM for the main peaks of all the calibration samples. 53
3.7 Calculated sum of least squares for the angular and radial distributions of the samples in figure 3.17. 59

4.1 EDS results for several untreated and treated samples. Each measurement is done at a random cross-section, thus variations in composition for the inhomogeneous samples are expected to be significant. 89
4.2 Average composition and standard deviation for the treated CA samples compared to untreated CA. 89
4.3 Average composition and standard deviation for the treated NA samples compared to untreated NA. 90
4.4 Peak parameters of the fitted peaks in figure 4.32 94

C.1 Composition measured by EDS for the three different quantification areas marked in figure C.1. It is clear that an area close to the core measuredan increased oxygen content, which is due to the extent of the interaction volume into SiO_2. 133

List of Abbreviations

BSE Backscattered Electron

CVD Chemical Vapour Deposition

CZ Czochralski

EBSD Electron Backscatter Diffraction

EDS Electron Dispersive X-Ray Spectroscopy

FWHM Full Width at Half Maximum

LA-BSE Low-Angle Backscattered Electrons

RMG Rapid Melt Growth

SE Secondary Electron

SEM Scanning Electron Microscope

SLS Sum of Least Squares

XRT X-Ray Tomography

YAG Yttrium Aluminium Garnet

Chapter 1

Introduction

The advent of semiconductor technology has truly changed the world in many ways. Semiconductors are central to modern electronics, optoelectronics [1] and thermoelectric devices [2]. The corner-stone of the electronics industry, the transistor, was first fabricated in 1947 using Ge [3]. Today, however, the semiconductor market is completely dominated by Si, accounting for 97% of the integrated circuit market [4]. The material properties of Si, such as electrical conductivity, are only mediocre for semiconductor applications, but the ease of integration with the insulators SiO_2 and SiN made it preferable for the first integrated circuits [4]. Today, Si retains its dominant positions due to extremely high availability [1] and highly mature process technique due to 50 years of industrial development. The extremely low cost of Si wafer is achieved by a highly optimised Czochralski single crystal growth with growth rates around $50\,\mathrm{mm\,h^{-1}}$. Other semiconductor materials like GaAs and InP dominate small niche markets, such as radio frequency amplifiers, where material properties are imperative. However, the applications remain very limited due to the difficulty of integration with the existing Si integrated circuits, as well as much higher prices due to e.g. difficult manufacturing and material availability. As Si is so dominant in the semiconductor market, it is of great interest to find materials that have better material properties than elemental Si and that can be integrated into existing integrated circuits and mature production methods. A promising material that can allow for easy integration with Si devices, and open up for advanced tailoring of materials properties is SiGe. SiGe has already filled small markets with the introduction of heterojunction bipolar transistors [5], but the applications have been very limited due to fabrication difficulties. However, the introduction of bandgap tailoring by strain engineering has spurred a renewed interest in SiGe/Si heterostructures and SiGe in general [4] [6], especially on improving SiGe growth. What makes SiGe so appealing in the electronics industry is that it, through compositional variations and strain engineering, combines both excellent material properties with seamless integration with existing Si technology. This combinations makes it interesting for both high-end use, but also to improve e.g. Si CMOS technology. Additionally, lattice constant tailoring of SiGe can allow for it to be used as lattice matched substrate buffer layers between a Si chip and III-IV semiconductor devices [**?**], applied in e.g. GaAs solar cells [7].

Up until two decades ago, the application of SiGe was mainly restricted to high-end thermoelectric applications [8] [9]. The large difference in mass between Si and Ge effectively scatters phonons, resulting in a poor thermal conductivity. This, coupled with the excellent thermopower and electrical conductivity makes it an excellent thermoelectric material [2]. Recently, the thermoelectric properties have been further increased by nanostructuring of SiGe [10]. Another interesting field of appliation where SiGe is of great interest is in optoelectronics. Today, Si is also used extensively for optoelectronic purposes, but the rigid indirect bandgap is a major handicap, limiting it to e.g. passive photonic devices. SiGe is very promising for optoelectronic applications, as the bandgap can be altered both by composition and strain. Tuning the bandgap can increase the absorption range for e.g. solar cell applications [7]. As band gap is a function of composition, SiGe could be used as tunable intrinsic photodetectors [8]. With silicon, on-chip fabrication of low-loss waveguides has been demonstrated, and semiconductor-core fibres are being developed, particularly for mid-infrared applications. SiGe is of interest as an alternative material in this wavelength range. For both thermoelectric and optoelectronic properties, rapid at controlled growth of SiGe is of interest.

SiGe was first shown to be a fully miscible alloy at all compositions by Stöhr and Klemm in 1939 [11], and only a few extra points have been added to the phase diagram [12]. There are two ways that the SiGe can be used in electronics applications - as bulk single crystals, analogous to silicon substrates, or by depositing and annealing thin films. Both require understanding of the equilibrium states and the kinetics of crystal formation. There are several challenges with growth of SiGe, but the most fundamental challenge is the large separation of the liquidus and solidus of the system, requiring very slow cooling rates to compositional inhomogeneity. For a long time, no separation between homogeneous composition and single crystalline material was made for SiGe [8], as growth has been very application-based. Controlled and rapid growth of homogeneous, single crystalline SiGe would be very beneficial for the electronic industry. As substrate applications require excellent crystal quality and large single crystals, much effort is spent on growing suitable crystals. As of today, growing single crystals is very time consuming, with growth rates on the order of mm/h [8] [13]. The rates are simply to slow for most commercial applications. Growth of SiGe was initially done by slow freezing of melts, successfully growing macroscopic, homogeneous crystalline regions for a low Si content [14]. The first advanced method applied in order to grow SiGe single crystals was horizontal float zone recrystallisation [15] [16]. The resulting crystals suffered from very long initial transient and limited composition to a low Si content [8]. One of the most widespread growth techniques for SiGe single crystals today is the Czochralski method [17] [18] [19]. The method works well, but again, the growth velocity is limited to mm/h [20] [21] [22], much slower than for pure Si. Liquid phase diffusion has also been investigated, but growth rates are less than $1\,\mathrm{mm\,h^{-1}}$ [23]. A major limiting factor for most growth techniques is that the low thermal gradient imposed in the liquid phase only allow for slow growth rates in order to avoid constitutional undercooling [8]. A critical growth velocity can be defined for an alloy as the growth velocity where the resulting solid is has an inhomogeneous composition rather than homogeneous. According to Tiller *et al.*, the critical growth velocity increases with increasing thermal gradient in the melt [24]. Some growth experiments are summarised by Schilz and Romanenko in figure 1.1 [8], with calculated maximum growth velocities at thermal gradients of 20 °C cm^{-1} and 40 °C cm^{-1}. Recently, Koh *et al.* have demonstrated CMOS-compatible growth of small

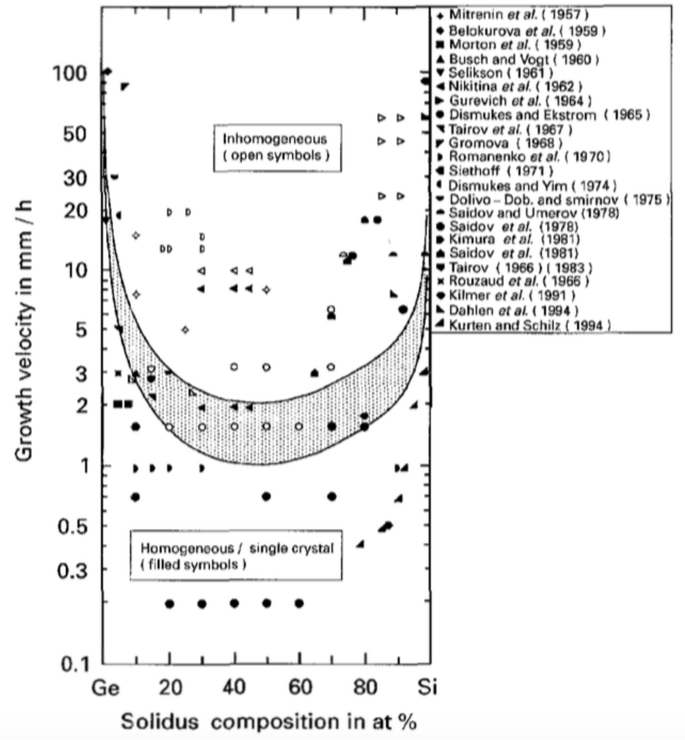

Figure 1.1: Plot of several experimentally grown SiGe crystals, with full symbols representing homogeneous/single crystalline samples, and empty symbols representing inhomogenoeus crystals. The two lines separated by the grey area marks the calculated critical velocities of single crystalline growth for two gradients. The figure is based on [8].

dimension SiGe by rapid melt growth [25] [26]. This has allowed for faster growth rates, but as the phase front is uncontrolled in the process, it does not offer control on composition.

The scope of this project is to investigate CO_2 laser-induced directional recrystallisation of SiGe and compared the results to conventional oven annealing. Fibres were produced by the molten core fibre drawing technique [27]. These fibres serve as a model system for testing existing theories on critical growth velocities as a function of size, composition and thermal gradient, and could find direct application as optical waveguides. The technique induces very high thermal gradients in the melt, and allows direct control over the interface velocity via the rate at which the laser is scanned across the fibre. The thesis investigates whether the high thermal gradient in the melt will suppress constitutional undercooling and allow for much higher growth rates than previously reported. according to the theory of Mullins and Sekerka [28], growth at reduced dimensions will see an increased growth interface stability due to capillarity. Thermal diffusion ought to further increase the stability at extreme thermal gradients [29]. This work will therefore investigate if reducing the dimensions of the fibre stabilises the growth interface, allowing for even higher growth rates. The aim is to demonstrate a growth technique allowing for liquid phase growth at rapid rates, with control of the growth interface.

Chapter 2

Theory and Background

Solidification and crystal formation from a liquid is based on nucleation and growth of solid nuclei. An understanding of the crystallisation process is important in order to design suitable recrystallisation schemes, as well as for the interpretation of the resulting materials. The theory will be separated into two main sections: Section 2.1 will cover the theory behind solidification of SiGe, and section 2.2 presents relevant theory for the characterisation techniques used. The chapter will start up with a very general introduction to phases and phase transformations, as it forms the basis for solidification. Section 2.1.2 will then cover the thermodynamics and kinetics of nucleation and growth of a new phase during a phase transition. Important factors for crystal growth will then be discussed in section 2.1.3. The following section will then discuss solidification of the $\mathrm{Si_xGe_{1\text{-}x}}$ system, focusing on both growth of SiGe, as well as recrystallization techniques.

Following the theory of solidification, relevant background for characterisation techniques used in the thesis will be presented. It starts with an introduction to how electrons interact with matter, as these interactions are the basis of most characterisation techniques used in this thesis. Section 2.2.1.2 will discuss how electron interactions with solids can be used to image a material with a scanning electron microscope. Microcompositional analysis through electron dispersive X-ray spectroscopy will be discussed in section 2.2.1.3. A simple introduction to microstructural crystallographic analysis by electron backscattered diffraction will be given in section 2.2.1.4.

Section 2.2.2.1 will explain the different interactions of X-rays with matter. The use of photoelectric absorption in X-ray tomography, and the production of 3D images of a sample, will be explained in section 2.2.2. Finally, an introduction to the Raman effect will be given. This is put in context with the use of µ-Raman spectroscopy as an analytical technique.

2.1 Solidification

2.1.1 Phase Transformations

Phase transformations are an essential part of materials science, and a thorough introduction is thus essential. Several definitions of a phase exist, but it can in general be defined as any area of a thermodynamic system wherein all physical parameters are the same. Examples of phases can the traditional solid, liquid and gaseous. However, it can also be e.g. a paramagnetic or a ferromagnetic phase in a perovskite. Thermodynamics can be used to determine equilibrium phase transformations, but not the rates of transformation, as they are governed by the kinetics of the system. A phase transformation can occur when the change in Gibbs free energy is negative for the transformation. The Gibbs free energy, G, is a thermodynamic parameter defined by equation 2.1 [30].

$$G = H - TS \tag{2.1}$$

Where H is the enthalpy of a phase, S the entropy and T the temperature. The Gibbs free energy of a phase depends on temperature, pressure and quantity of the substance [31]. Transformation between phases can occur when the Gibbs free energy of one phase is lower than the initial phase. Figure 2.1 sketches the Gibbs free energy at constant pressure versus temperature for the liquid and the solid phase of a material A. The intersection of the free energy curves mark the melting point, as temperature above T_m will favour the liquid state and temperature below favour the solid state. This is clearly seen, as the entropy term is dependent on temperature a more entropic phase will be favourable at higher temperatures.

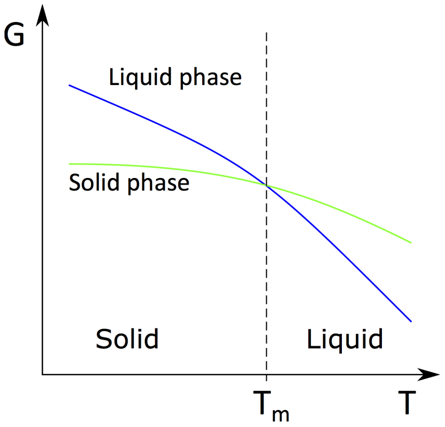

Figure 2.1: Graph illustrating the free energy a solid and a liquid phase with respect to temperature. The thermodynamically favoured phase will be the one with the lowest free energy at the given temperature, therefore T_m marks the phase transition.

A standard single component phase diagram can be made by defining the melting point and evaporation point for all pressures (P) and plotting it in a T-P diagram. For binary systems, a temperature versus composition phase diagram is of great interest. Controlling the microstructure and properties of a binary alloy requires knowledge of its phase diagram. Such a diagram will show what phase or phases are present at a given pressure, temperature and composition of the material. Figure 2.2 shows the simplest binary phase diagram of a fully miscible solid solution [32], common for many binary alloys such as SiGe. The gap between the solid and the liquid phase is due to the fact that melting in isomorphous binary alloys occurs over a range of temperatures. The coexistence of both a solid and liquid phase is thermodynamically favourable over a certain temperature range because the change in entropy by introducing a bit of the new phase is greater than the change in enthalpy of instantaneous transformation to the new phase at certain temperatures [32].

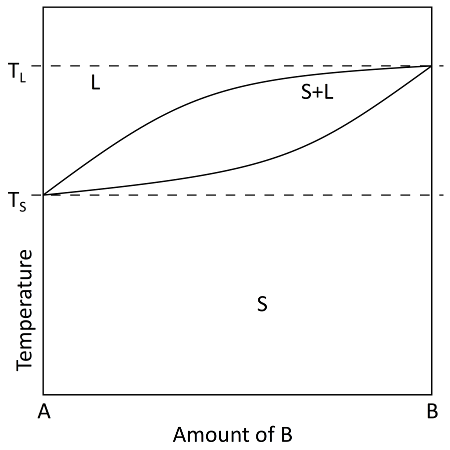

Figure 2.2: A simple isomorphous alloy phase diagram. The alloy can either be in a binary liquid phase (L), a solid solution phase (S) or the two phases can coexist (L+S) over a given range of temperature and composition. The line separating L and S+L is termed the liquidus and the line separating L+S and S is the solidus.

Even though a phase transition is thermodynamically favourable, it might be kinetically hindered, preventing a phase change form occurring in practice. A well known example of such a phase change is the thermodynamically favourable transition for carbon from diamond to graphite, which occurs extremely slowly due to the high activation energy. The following section will present the thermodynamic theory of solidification in term of nucleation and growth, and discuss the activation energy and kinetics related to the phase change.

2.1.2 Thermodynamic and Kinetic Treatment of Nucleation

Formation of a crystalline solid can occur in several ways, but solidification from a melt is by far the most common [30]. Solidification from a melt is a phase transformation from a liquid to a solid. Such a transformation can only occur when the change in Gibbs free energy of the system is negative [30]. Solidification occurs by the formation of a solid phase nucleus, and proceeds by growth of the stable nucleus under favourable conditions. The thermodynamics of crystallisation will be given in the following section.

Crystallisation can occur in a system if the free energy of the transformation is negative. From elementary statistical thermodynamics, the free energy of transformation of a melt is negative when the system is below the melting point, meaning that the solubility is then too low to stay in solution. However, crystallisation often requires a lower temperature as the new phase is kinetically hindered by a required minimum nucleus size for stability. Nucleation of a new phase can primarily occur in three ways: 1, homogeneous nucleation, 2, heterogeneous nucleation, and 3, dynamic nucleation. Firstly, homogeneous nucleation will be considered. For a system, the change in free energy upon formation of a spherical embryo of radius will have two components: an interfacial components and a volume component. The interface component will be positive as any surface will have a positive surface energy, whereas the volume free energy will be negative. The total change in free energy of formation for a nucleus as a function of radius, r, is given by:

$$\Delta G = \Delta G_S - \Delta G_V = 4\pi r^2 \gamma + \frac{4}{3}\pi r^3 \Delta G_v \tag{2.2}$$

Where ΔG_S is the surface free energy of an embryo, ΔG_V the volume free energy, σ the interfacial tension between melt and crystal, and ΔG_v the free energy per unit volume. The change in free energy with respect to embryo radius is illustrated in figure 2.3.

Equation 2.2 assumes that the composition and structure of all embryos are equal. Embryos will form continuously, due to statistical fluctuations, however only those surpassing a given critical change in free energy will be stable and can grow into crystals. As the volume contribution and surface contribution follow different dependencies on the radius, a critical radius of a stable embryo can be calculated. Derivation of equation 2.2 with respect to radius gives:

$$\frac{\partial \Delta G}{\partial r} = 8\pi r \gamma + 4\pi r^2 \Delta G_v \tag{2.3}$$

By considering $\frac{\delta G}{\delta r} = 0$, a critical size of nucleation can be calculated:

$$r_c = \frac{-2\gamma}{\Delta G_v} \tag{2.4}$$

Insertion of the critical radius into equation 2.2 gives the critical free energy required for formation of a stable nucleus:

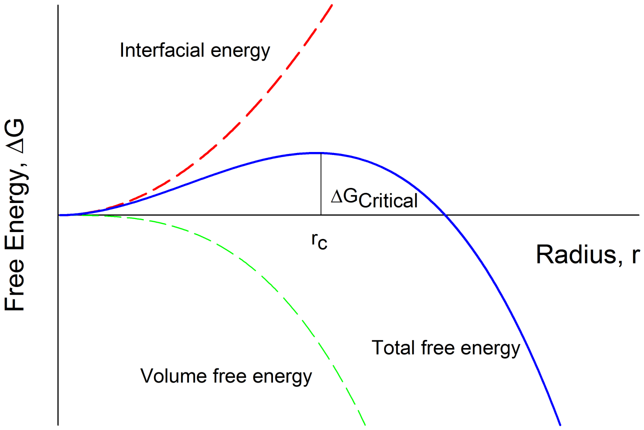

Figure 2.3: Total free energy change for formation of a nucleus with respect to the nucleus radius (blue line). The surface free energy component is marked by the red dashed line and the volume free energy component by the green dashed line.

$$\Delta G_{critical} = \frac{4}{3}\pi r_c^2 \gamma \tag{2.5}$$

The critical free energy required represents an activation energy for crystallisation. The activation energy of nucleation acts as a kinetic barrier for nucleation. The rate of nucleation will follow an Arrhenius dependency and can be described using equation 2.6 [33].

$$J = A \exp\left(\frac{-\Delta G}{kT}\right) = A \exp\langle -\frac{16\pi\gamma^3\nu^2}{3k^3T^3(\log S)^2}\rangle \tag{2.6}$$

Where A is a system constant, k is the Boltzman constant, γ the interfacial tension, ν is the molecular volume and S the supersaturation. It is apparent from equation 2.6 that nucleation rate is governed by temperature, supersaturation and interfacial tension.

Supersaturation is defined as when a solution has a higher activity of a solute than the equilibrium activity at the given temperature is. For a homogeneous solution with multiple components, the most abundant is termed the solvent and the less abundant components the solutes. Examples can be salt in water where salt is the solute and water the solvent. For the case of SiGe, both Si and Ge can be defined as the solute, as the alloy is soluble over the whole composition range. The definition can often be simplified by the using of concentrations instead of activity [33], as illustrated in equation 2.7.

$$S = \frac{a_i}{a_{eq}} \approx \frac{c_i}{c_{eq}} \tag{2.7}$$

Where c_i and a_i is the concentration and activity, respectively, of component i and c_{eq} and a_{eq} the equilibrium concentration and activity of the species. For the case of a fully miscible binary melt such as Ge in Si, the equilibrium concentration is given by the liquidus line in figure 2.10. Thus, for temperatures above T_L in figure 2.2 the solution never reaches supersaturation, whereas for lower temperatures adding enough Ge will supersaturate the solution. This is clearly seen by following an isothermal line at a temperature between T_S and T_L: at a given point the liquidus is crossed and the the solution will be supersaturated. For low temperature very high amounts of Ge are required, technically making Ge the solvent, however, this is just a formal definition and does not affect the science. The supersaturation can also be described using the chemical potential, μ, of the solid and the solution and is given by equation 2.8 [33]:

$$S = \exp(\frac{\delta\mu}{RT}) \tag{2.8}$$

Where $\delta\mu$ is the difference in chemical potential, R the gas constant and T the temperature. The supersaturation can thus be controlled in two ways: Either more solute can be added to increase the activity, or the equilibrium activity can be altered by lowering the temperature. The latter means that supersaturation can be achieved by lowering the temperature of the solution, as seen in equation 2.8.

Homogeneous nucleation in pure melts is very unlikely due to the high activation energy [30]. For alloys, achieving the required supersaturation is often more feasible and homogeneous nucleation can occur. This is mainly because it is easier to achieve a high supersaturation by adding solute rather than undercooling the melt. However, it is far more common to observe heterogeneous nucleation [30] [33]. The theory is quite complex, and will not be covered in great detail. For a more detailed derivation, the reader is directed to chapter 4 of [30]. Heterogeneous nucleation is when an embryo is formed on a seed, which reduces the critical energy of formation. Seeds can be crystals added during manufacturing, the side of a crucible, or even dust particles or other contaminants. If the solidifying material is in contact with a different material, such as a solid crucible, it will usually acts as a centre for heterogeneous nucleation, unless the cooling rate is extremely rapid. The reason that the activation energy is lowered is because the area-to-volume ratio of the nucleus will be reduced when in touch with a seed. Interfacial tension between the nucleus,the seed and the melt will form a wetting angle, and the activation energy decreases as wetting increases. A modified critical energy for heterogeneous nucleation can be defined on the basis activation energy for homogeneous nucleation and the wetting angle. Volmer expressed the relation in 1939 as equation 2.9 [34]:

$$\Delta G^{\text{Heterogeneous}}_{\text{critical}} = \frac{(2+\cos\theta)(1-\cos\theta)^2}{4} G^{\text{Homogeneous}}_{\text{critical}} \tag{2.9}$$

where θ is the wetting angle, and $\Delta G^{\text{Heterogeneous}}_{\text{critical}}$ and $\Delta G^{\text{Homogeneous}}_{\text{critical}}$ the critical free energy change for heterogeneous and homogeneous nucleation, respectively.

The third type off nucleation is dynamic nucleation. This is simply a part that has broken of an already initiated crystal, moved to another location and initiated growth there. For large melts were substantial convection occurs it is important to consider dynamic nucleation.

2.1.3 Crystal Growth

Following the formation of a stable nucleus, growth can proceed. Growth is a very complex phenomenon, and there are numerous theories and models out. A simple introduction of relevant growth phenomenon will be given here.

2.1.3.1 Undercooling and Supersaturation

As explained in section 2.1.2, supersaturation is needed for solidification to occur. There are five known different types of undercooling: kinetic- , thermal- , constitutional-, curvature- and pressure undercooling [30]. Only thermal and consitutional will be considered here. Thermal undercooling is when the liquid is cooled below the equilibrium melting temperature and nucleation is absent. The solution is then supersaturated and nucleation can occur. For alloys, such as SiGe, constitutional undercooling is usually more important, and often cited as a main reason for the difficulty of SiGe solidification [13]. It occurs due to compositional variances across the solidification interface. The areas with a higher solute concentration can then be locally supersaturated, which in turn can cause nucleation.

When a solution is solidifying there will be a solidification interface, a solid-liquid phase boundary, travelling through the liquid. In general there are two ways that solidification occurs; either with a single solidification interface travelling into the liquid or with many nuclei growing separately. A combination of the two is also possible, and the type of solidification is determined by the cooling conditions. The behaviour of the interface is essential for the resulting structure. When solidification occurs in a binary alloy such as SiGe, the composition in the solid and liquid phase will not be the same. The equilibrium segregation coefficient is the ratio of solute to solvent in the solid phase relative to that of the liquid face. For a binary system such as SiGe, it is defined by the following equation:

$$k = \frac{C_S}{C_L} \tag{2.10}$$

C_S is the concentration of solute at the solidus, and C_L the concentration at the liquidus. As discussed in section 2.1.2, for SiGe, both Si and Ge can be defined as the solute, giving inverse distribution coefficients. Figure 2.4 illustrates cooling in a phase diagram. A liquid of composition X that is cooled along the dashed red line to the point marked by a red dot will see the formation of a solid phase of a different composition to the liquid phase. The solute concentration of the liquid is X_L, determined by the liquidus at the temperature T. Solute concentration in the solid will be determined by the solidus, in this case being X_S. The relative amounts are determined by the lever rule [31].

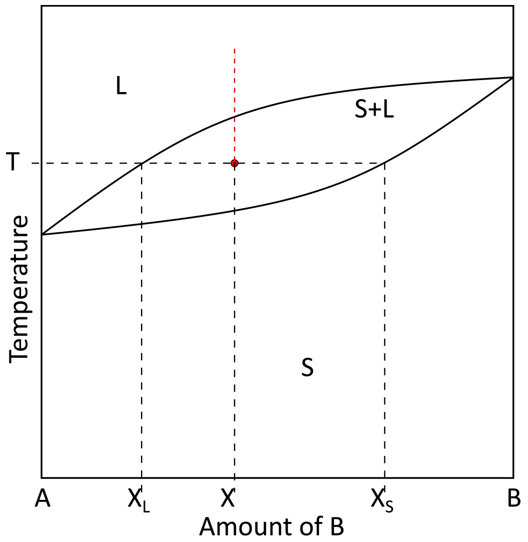

Figure 2.4: Distribution coefficient illustrated in a binary alloy of composition X at temperature T. X_L is the concetration of B in the liquid phase, whereas X_S is the concentration of B in the solid phase.

As mentioned above, crystallisation is governed by two mechanisms: mass- and heat transport. If we consider a growth interface of a binary alloy where $k < 0$, which is the case for Ge in SiGe, solute will be rejected from the crystal upon solidification. This will lead to a solute rich area. For a sufficiently slow crystallization, the solution will have time to equilibrate by diffusion as crystallization occurs and the equilibrium distribution coefficient is accurate. This is shown in figure 2.5a. For faster growth rates, diffusion will not have sufficient time to equilibrate the liquid composition, and a steady state will be reached with a higher concentration in the liquid close to the interface. This is shown in figure 2.5b. Steady state is reached when the solute rejection from the growth interface is in balance with the diffusion away from the growth interface. Thus, the solute distribution depends on growth velocity and how much time diffusion has to work. This is not the whole story though, as mass balance will cause initial and final compositional transients in the solid. This will be covered in section 2.1.3.2.

2.1.3.2 Directional Solidification

A simple system that shows the effects of solute segregation is directional solidification of a rod. Consider the directional solidification of a molten rod of SiGe. Assume a planar phase

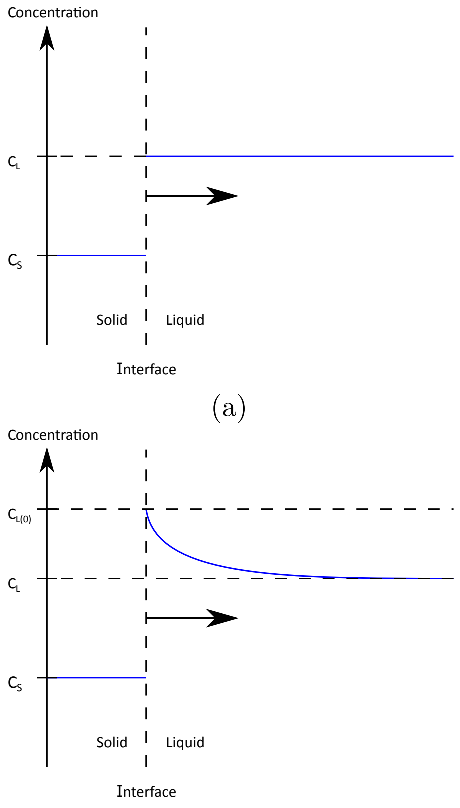

(a)

(b)

Figure 2.5: Distribution of solute in when crystallisation occurs in equilibrium (a) and at an faster rate (b). For the slow growth rate, the solute rejected from the growth interface has time to equilibrate in the liquid by diffusion. For a high growth rate, an solute rich interface layer is formed close to the growth interface.

front, constant growth rate and that diffusion in melt is dominant and with distribution coefficient k. As the solid forms, there will be a concentration difference at the interface with respect to the solute. For $k < 1$, the solid will be deprived of solute and the liquid next to the interface will be solute-rich. Further growth will see a solid of higher concentration as the liquid solidifying is already Ge-rich compared to rest of the liquid, as seen in figure 2.6. However, diffusion will act to minimise the concentration difference of solute in the liquid. A mass balance is reached, when the number of solute atoms diffusing away from the interface is equal to the number of solute atoms rejected from the advancing solid. The steady state crystallisation is not reached until the mass balance is achieved. As the equilibrium distribution coefficient is only valid for very slow solidification rates with minimal temperature gradients over the phase boundary, it is often inaccurate in real systems. In the steady state condition a more accurate distribution coefficient is the interface distribution coefficient, defined as:

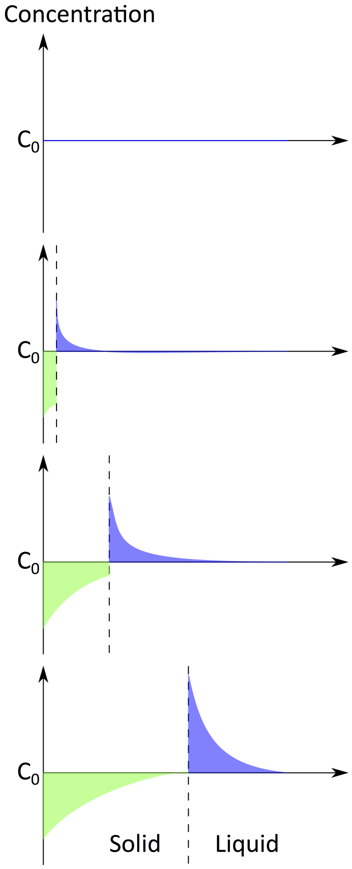

Figure 2.6: Illustration of solute concentration in a growing solid and the liquid, for $k < 0$. Green marks the solid and blue the liquid, and the dashed line the interface. The start of the solid will have a composition based on k, then, as more solute is rejected the interface layer faces an increasing solute concentration. The solidifying area will therefore have an increase in solute composition as well. Steady state is reached when the solid composition is C_0.

$$k^* = \frac{C_S}{C_{L(0)}} \tag{2.11}$$

where $C_{L(0)}$ is the concentration in the liquid next to the interface, as seen in figure 2.5b. As this can be hard to physically measure, a more practical distribution coefficient is the effective distribution coefficient, k^*, defined by Burton, Prim and Slichter [35] as:

$$k_{\text{eff}} = \frac{k_0}{k_0 + (1 + k_0)e^{-\frac{v\partial}{D}}} \tag{2.12}$$

where v is the solidification velocity, ∂ is the extent of the interface layer occurring due to solute rejection and D the diffusivity of the solute. The effective distribution coefficient modifies the equilibrium distribution coefficient, so for low velocities $k_{\text{eff}} \approx k$.

For directional solidification, the nucleation point will have a concentration illustrated in figure 2.6, based on a melt of concentration x. However, the melt at the interface will experience an increasing concentration, thus also changing the concentration of the solid, until steady-state is reached. The steady-state will continue as long as there is a steady supply of solute atoms.

At the end of the rod, a final transient will appear as there is a solute-poor region due to the initial transient. Figure 2.7 shows the resulting concentration along the rod.

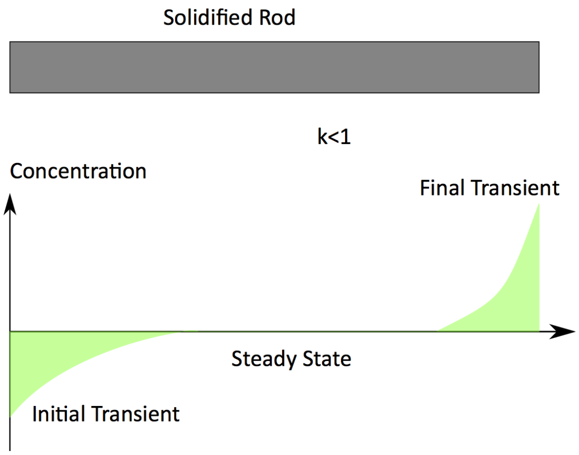

Figure 2.7: Schematic of a solid rod after directional solidification, with a graph illustrating the concentration profile along the rod. Note that the illustration is for the case $k < 0$

2.1.3.3 Interface Stability

The stability of the solid-liquid (melt) phase boundary is imperative with respect to the final structure during solidification. There are two sources of interface instability for an alloy: thermal instability and compositional instability. Heat transfer in the system determines the final structure of the system [30]. If the liquid in front of the advancing solid phase boundary has a positive temperature gradient, a smooth interface is maintained. This is because any instability will dissolve as the highest undercooling is at the phase boundary. On the other hand, if the thermal gradient is negative, the thermal undercooling will increase when moving into the melt. Any instability occurring will grow. The occurring thermal gradients is determined by how the system transfers heat: conduction through the solid crystal and mould, or convection and conduction through the liquid. For alloys, this stability requirement regarding the thermal gradients is more complicated. The solute rejection at the interface will cause a solute rich boundary layer. This leads to a lower liquidus temperature next to the interface. A new problem then arises - constitutional undercooling can cause unstable interfaces despite a positive temperature gradient. If the temperature gradient from the liquid into the solid is lower than the liquidus gradient a constitutional undercooling is caused and an interface instability arises. The effect of an unstable interface will be discussed in section 2.1.3.5, but an unstable interface will cause a transition form planar growth to cellular or dendritic causing compositional inhomogeneity for alloys.

2.1.3.4 Critical Growth Velocity

Section 2.1.3.3 has outlined how the resulting structure depends on the solid-liquid interface stability. As solute rejection is mitigated by diffusion, the growth rate of the solid will determine the interface stability and thus the structure. A critical growth velocity can be defined as where the liquid will be supercooled, and it marks the change into the solidification of a polycrystalline material. Tiller et al. derived an expression for the critical velocity in 1953 [24], and the results is presented in equation 2.13:

$$v_c = \frac{D\nabla\Theta k}{\nabla T_L x(k-1)} \tag{2.13}$$

where D is the diffusion coefficient, $\nabla\Theta$ is the temperature gradient in the liquid, ∇T_L is the slope of the liquidus, k the distribution coefficient and x the composition. It is clear that a negative thermal gradient will result in a negative critical growth velocity, confirming that the interface is always unstable then.

The Tiller criterion is often used when considering critical growth rates [36] [13], and has been shown to correspond well with experiments at several occasions [8] [13], as shown in figure 1.1. Often, the Tiller criterion is efficient to determine crystallisation schemes [37]. However, a more thorough criterion was developed by Mullins and Sekerka in 1963, developing a theory considering the stability of the interface with regards to the time dependence of a sinusoidal perturbation [28]. The theory considers the the time and frequency dependence of the sinusoidal disturbance to determine whether or not the perturbation grows, causing an unstable interface, or decays. There are three parts governing the time derivative of the perturbation, and the balance between the three determines the stability of the interface. The theory will only be qualitatively explained in this thesis. The first term is due to the capillarity and is always negative, meaning that it favours the decay of a disturbance. The second term comes from the thermal gradient in the system, but unlike the Tiller criterion it considers the gradient in both the liquid and solid. Assuming a negative gradient, this term is negative and favour decay. Finally, the third term represents the effect of the solute on the equilibrium melting temperature. The third term is always positive, and will thus favour growth of any sinusoidal instability. The magnitude of each parameter depends differently on the frequency of the sinusoidal perturbation, and thus different frequencies will favour growth and decay. If capillarity can be ignored, the criterion reduces to a criterion very similar to that proposed by Tiller *et al.*. However, in the case where the capillarity effect dominates the solute effect a state of absolute stability is reached [28]. This can occur at small scales and high growth velocities. This thesis will aim to investigate the effect of small scale and growth velocity on interface stability.

The Mullins-Sekerka criterion has later been revised to include the effect of thermal diffusion, which is relevant for high thermal gradients [29]. Thermal diffusion can have a stabilising role on the interface. All in all, Mullins-Sekerka theory can, for certain systems, give up to twice the critical growth velocity of that given by Tiller's criterion [37].

2.1.3.5 Solidification Structure

Upon solidification, there are two different regimes: stable interface and unstable interface. A stable interface will results in planar growth of alloys, usually only achieved with high temperature gradients and low solidification velocities. On the other hand; if the interface is unstable any disturbance will grow due to thermal or constitutional undercooling. At low undercooling cellular growth occurs, whereas at higher levels of undercooling a transition to dendritic growth occurs. The resulting structure depends on temperature gradient relative to solidification velocity, and solute concentration, as illustrated in figure 2.8.

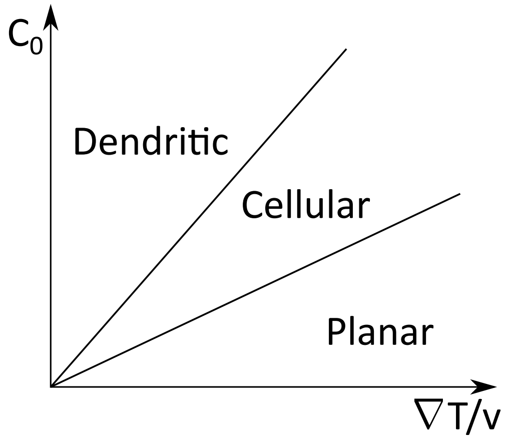

Figure 2.8: Transition between different growth structures depending on $\frac{\nabla T}{V}$ and solute concentration (C_0). The balance between thermal gradient, growth rate and solute concentration determines if growth is homogeneous or not.

The relationship illustrated in figure 2.8 is based on the work on redistribution of a solute upon solidification by Tiller et al.[24]. Cellular growth occurs when a disturbance grows into the liquid. The latent heat released from the growing spike will cause a localised temperature increase surrounding the spike. This creates a negative temperature gradient, as the liquid next to the spike has a higher temperature than the bulk liquid, leading to further instabilities and the growth of more spikes. If the undercooling is sufficiently high and the growth velocity sufficiently fast, side protrusions might develop, leading to a dendritic structure. The different growth structures and the relationship to thermal gradient is illustrated in figure2.9.

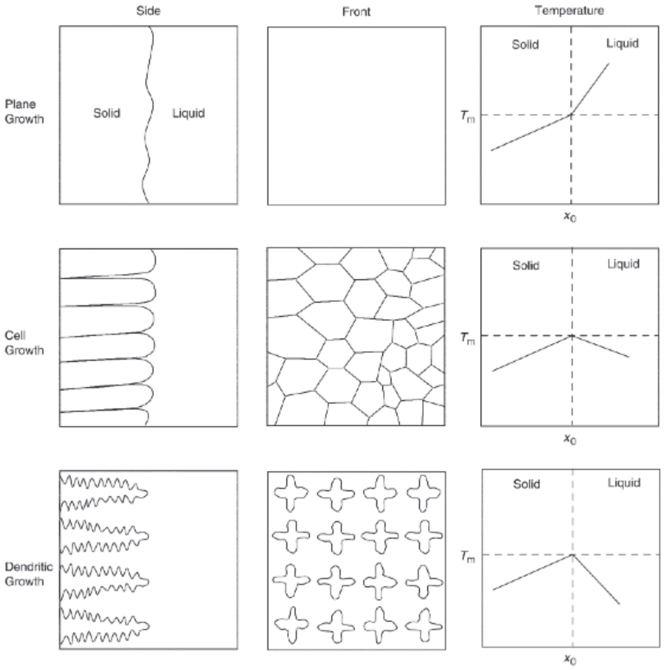

Figure 2.9: Schematic illustration showing the resulting solidification structure depending on thermal gradient across the growth interface. A positive gradient will see a stable phase front, while a negative gradient will cause an unstable phase boundary. Figure from [38].

2.1.4 Growth of $\mathbf{Si_xGe_{1\text{-}x}}$

Both Si and Ge adopt the diamond structure, with lattice parametes of $a_{Si} = 5.42$Å and $a_{Ge} = 5.64$Å [31]. As Si and Ge adopt the same crystal structure, have a small lattice parameter difference and are of similar electronegativity they form a substitutional solid solution with the diamond structure. The phase diagram of SiGe is presented in figure 2.10.

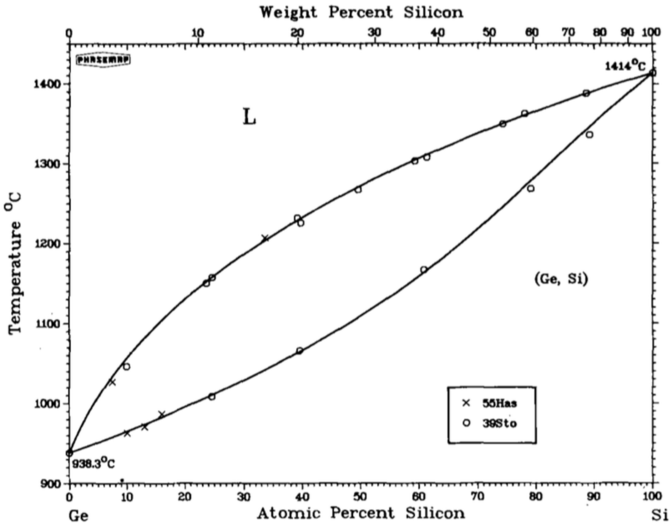

Figure 2.10: Phase diagram of SiGe, retrieved from Springer [39].

Si_xGe_{1-x} is a substitutional solid solution alloy that is fully miscible at all compositions. This miscibility was first shown in 1939 [11], and is clear in the phase diagram of SiGe, presented in figure 2.10. Over the last five decades it has received a lot of interest due to its good thermoelectric properties [40] [41], and was selected for NASA's Deep Space program to convert heat to electricity [8]. Despite reaching commercial applications, SiGe to this day remains a laboratory scale solid solution material. Due to the large separation of the liquidus and solidus lines, phase separation often occurs in SiGe, giving compositional variations. The critical growth velocity of bulk crystals is usually on the order of $1\,\mathrm{mm\,h^{-1}}$ to $8\,\mathrm{mm\,h^{-1}}$ over the whole composition range [8], thus leading to long processing times. Exploring new annealing procedures that can allow for faster processing is of great interest. The following sections will present different growth techniques used to grow SiGe today and their limitations.

Over the years, many different growth techniques have been tried in order to grow bulk SiGe. This section will briefly introduce the most common methods, as well as the method used in this thesis.

2.1.4.1 Slow Freezing

The first attempts and success of single crystal SiGe growth was by slow freezing of a melt [14]. By slowly cooling it in a quasi-equilibrium state the phase separation can be avoided. Achieving a single crystal requires nucleation of a single nucleus and following growth. As the nucleation rate is dependent on the undercooling, a slow cooling rate will cause few nucleation events and allow for the growth of large grains or single crystals. The slow cooling will also allow for the solid composition to follow the solidus and avoid a coring effect on composition. Further information can be found in e.g. chapter 9 of [32]. The original experiments done by slow cooling used very complex solidification schemes and no clear cooling rate is determined or stated [11] [14]. More recent experiements have shown homogeneous crystals grown at cooling rates as slow as $0.5\,°\mathrm{C\,h^{-1}}$ [42].

2.1.4.2 Czochralski

Growth of SiGe single crystals has historically been done by Czochralski growth (CZ), using a similar set-up as used for pure Si [19] [13] [8]. The technique employs seeded growth of single crystalline SiGe by contacting a SiGe seed crystal into a SiGe melt. The crystal is then slowly drawn out of solution with growth occurring at the interface. High quality crystals can be achieved using the technique, but avoiding segregation usually requires very slow growth velocities of approximately $1 - 8$ mm/h [43][21][22]. Besides slow growth rates, there are still problems with macrosegregation and uneven composition [8].

2.1.4.3 Bridgeman

It has been attempted to grow SiGe single crystals by the Bridgeman process [44] [45]. The technique consists of melting a polycrystalline ingot and slowly solidifying it from one side with a seed. Despite successful growth of single crystals, the technique can only handle very small melt volumes and thus slow production rates. Another problem is that the final crystal will have a compositional variation along the growth axis [46].

2.1.4.4 Other Growth Methods

CVD growth of SiGe has seen an increased interest with the advent of strained heterostructures [47][48], however, it has also been applied for bulk growth of SiGe [46].Growth rates are very slow, but the result is good. Kinoshita *et al.* have developed a growth technique they call travelling liquidus-zone method, where a homogeneous crystal is grown by zone melting [49]. The solute distribution s controlled such that the solute concentration in the melt zone is proportional to the thermal gradient [49]. Homogeneous crystals have been produces for Ge contents of 50at% [50] [51]. Despite the successful growth of homogeneous crystals, the growth rates are very low for bulk crystals. Recently, rapid melt growth has been implemented in the growth of SiGe [26]. RMG is a seeded melt growth technique that allows for growth of SiGe in restricted structures such as multi-gate structures on insulators [26]. Single crystalline SiGe was grown using a Si seed by liquid phase epitaxy at cooling rates of $150\,°\mathrm{C\,s^{-1}}$. Despite fast growth rates, the growth method is very restricted in application with respect to growth geometries [26].

2.1.5 Recrystallisation Techniques

Recrystallisation is the process of nucleating a new set of grains from an already grown crystal or amorphous region in a controlled manner. This can occur by heating without melting, or simply by re-solidifying in a controlled manner. Growth methods such as CZ rely on growing a single crystal straight out of solution, but as discussed in section 2.1.4, it is a slow process. Another possibility, as is done in this thesis, is to grow the crystals in a imperfect manner, then recrystallise the solid.

2.1.5.1 Slow Freezing With Homogeneous Cooling

One of the simplest recrystallisation techniques is simply to melt and then solidify by slow freezing. As outlined in section 2.1.4.1, the process can be hard to control, but can produce single crystals.

2.1.5.2 Zone Melting

A popular technique in for refining crystals that has enabled the electronics industry is zone melting. It allows for recrystallisation of a crystal under controlled rates, allowing for improved structure and reduced impurity levels [30]. A melted zone is created and translated through the sample. This causes directional solidification. The melt zone can be created by localised heating, or by use of a suitable solvent and heating. Either the sample or the heater is translated to move the molten zone through the sample, dissolving the solid in front and recrystallising behind. A major part of this work was directional recrystallisation by zone melting using a CO_2 laser. The method can be explained by considering a fibre with overall composition x. The melt zone created will be undersaturated with respect to Ge, and will thus preferentially dissolve Ge from the unmelted solid. Thus, a solvent rich melt zone can be transported through the rod. This is illustrated in figure 2.11. Again, an initial and a final transient occurs, with a steady-state region in between. The compositional variations of the recrystallised rod will depend on several parameters, such as zone length and scan velocity. It is important to note that the main body of the rod will have a lower solute concentration after zone refining, as seen in figure 2.11.

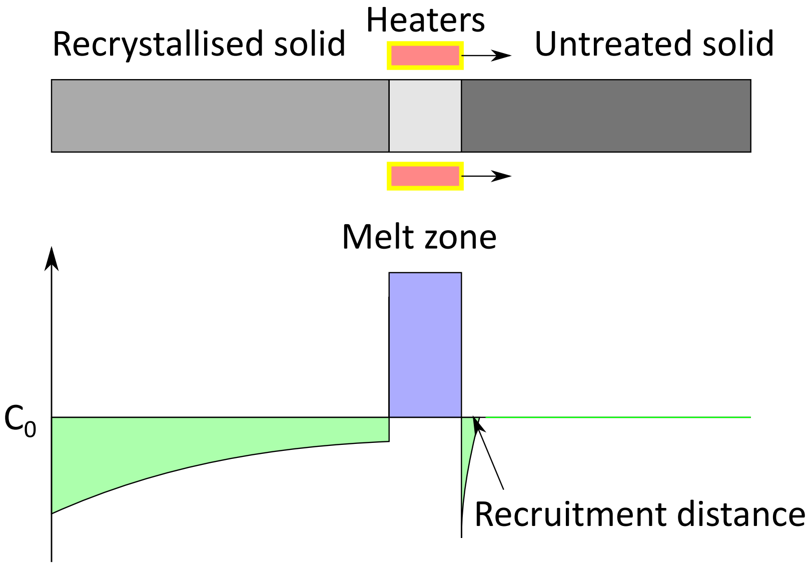

Figure 2.11: Schematic of zone melting by translating heaters. A solute rich melt zone is translated through the material. A small area in front of the melt zone will be solute poor as well, due to the solute being recruited into the melt zone.

2.2 Characterisation Techniques

Both the scanning electron microscope and x-ray tomography are based on the interactions of electrons and x-rays with matter. Thus, the interactions of relevance will be covered in detail in sections 2.2.1.1 and 2.2.2.1, respectively. Section 2.2.1.2 will then develop an understanding of how the SEM instrumentation allows the user to take advantage of secondary effects induced by electrons interacting with the sample, and optimise the information obtained by control of important parameters, such as beam current and acceleration voltage. Electron dispersive X-Ray spectroscopy as an add-on to SEM for micro-compositional analysis will also be discussed in section 2.2.1.3. Section 2.2.1.4 will then introduce the concept of electron backscattered diffraction for crystallographic analysis. Further on, section 2.2.2 will discuss how interactions between x-rays and a sample can be used in an x-ray tomograph to create 3D reconstructions.

2.2.1 Scanning Electron Microscope (SEM)

2.2.1.1 Electrons and Matter

Consider an electron entering a solid. The electron is termed a primary electron, and in the case of an electron beam, the primary beam. When an electron enters a solid, the electron will usually be scattered. The average distance between each scattering event, termed the mean free path, can be defined by equation 2.14 as

$$\lambda_{mfp} = \frac{1}{\mathrm{N}\sigma} \tag{2.14}$$

where N is the amount of particles per unit volume of the specimen, and σ is defined as the apparent cross-section the sample particles present to the incoming electron [52]. There are two main types of scattering that can occur: 1, Elastic scattering and 2, inelastic scattering.

Elastic Scattering If the incoming electron is scattered, but the electron energy is unchanged ($\Delta E = 0$) it is termed elastic scattering. The energy must remain unchanged, but the direction of the electron can change. Elastic scattering is a result of Coulombic interactions between the primary electron and both the nucleus and its associated electrons [52]. The primary electron can be scattered at any angle, and the probability of scattering through a given angle θ is given by:

$$p(\theta)\alpha\frac{1}{E_0^2 sin^4(\theta)} \tag{2.15}$$

where E_0 is the energy of the beam and the scattering angle is $\theta \in [0, 2\pi\rangle$. From equation 2.15 it is clear that elastic scattering will mainly occur at small angles, and that the scattering through any angle decreases with energy of the primary electron. The amount of elastic scattering is strongly affected by the atomic number, and increases approximately as Z^2 [53]. This is because the mean free path of elastic scattering depends on atomic number, or rather the apparent cross-section of the atoms. The probability of elastic scattering is thus strongly dependant on the atomic number of the sample. This dependency is due to the strong dependency of the apparent cross section on atomic number, following approximately Z^2 [54]. More on the subject can be found in introductory books on Quantum Physics, such as chapter X in Mandl [54].

Inelastic Scattering Inelastic scattering is a collection term for several scattering processes that causes a loss in energy for the primary electron ($\Delta E < 0$). Some of the most important inelastic scattering mechanisms are

Phonon Scattering A primary electron can excite a phonon in the sample, thus losing a small portion of its energy (usually < 1eV).

Plasmon scattering For metals, the primary electron can cause a plasmonic excitation.

Inner shell excitation The incoming electron can transfer its energy to a inner shell electron of the sample, thus knocking it out and creating another free electron (secondary electrons).

Outer shell excitation Also electrons located in the outer shells of the sample atoms can be knocked out.

It is inelastic scattering that brings the primary electron to a hault inside the sample. In 1930 Bethe described the rate og energy loss (de) due to inelastic scattering over a distance ds as:

$$\frac{dE}{ds} = -2\pi e^4 N_0 \frac{Z\rho}{M_m E_i} \ln\left(\frac{1.166E_i}{(9.76Z + 58.5Z^{-0.19} * 10^{-3}}\right) \tag{2.16}$$

where e is the electron charge, N_0 Avogadro's number, ρ the density, M_m the atomic weight and E_i the electron energy at any point.

Theoretical calculations [55], as well as experimental work [56], have shown that electrons entering a solid experiences lateral spreading and energy loss, resulting in an interaction volume as shown in figure 2.12.

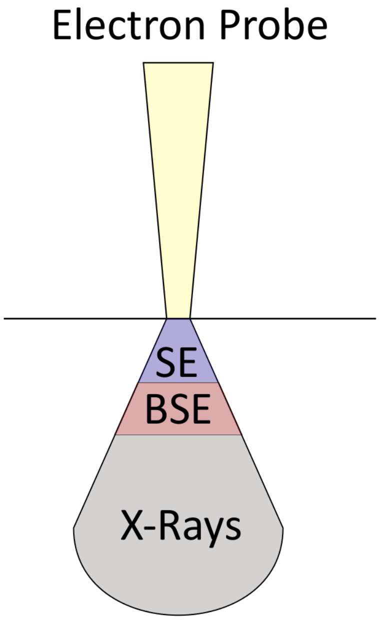

Figure 2.12: Schematic of the interaction volume of the primary electrons from the electron probe. The difference in escape depth for the different secondary effects is illustrated, and will be discussed in section 2.2.1.1.

A simplified measure of the interaction volume is the electron range, defined as the radius of an imagined hemisphere that contains a specified fraction of the electron trajectories in the interaction volume. Kanaya and Okayama [57] proposed equation 2.17 to describe the electron range in μm.

$$R_{KO} = \frac{0.0276 M_m}{Z^{0.89}\rho} E^{1.67} \tag{2.17}$$

From equation 2.17, it is clear that the interaction volume depends on the atomic weight and atomic number of the sample, the density of the sample, and the energy of the electron beam.

Secondary Effects As the primary electron enters the sample it will experience a combination of elastic and inelastic scattering, contained within the interaction volume. Several effects are induced by the scattering of the primary beam. Those detectable outside the material are termed secondary effects [53]. The most important effects in the case of SEM and EDS are backscattered electrons, secondary electrons and x-ray emission trough relaxation of excited atoms [53].

Backscattered electrons are primary electrons that have interacted with the sample and escaped. The samples can either experience large-angle elastic scattering and escape after few scattering processes, or several low-angle scattering processes. Backscattering removes energy from the primary beam. The energy distribution of electrons escaping a typical surface is illustrated in figure 2.13. Back-scattered electrons are high-energy electrons and can thus escape from quite far into the interaction volume, as shown in figure 2.12.

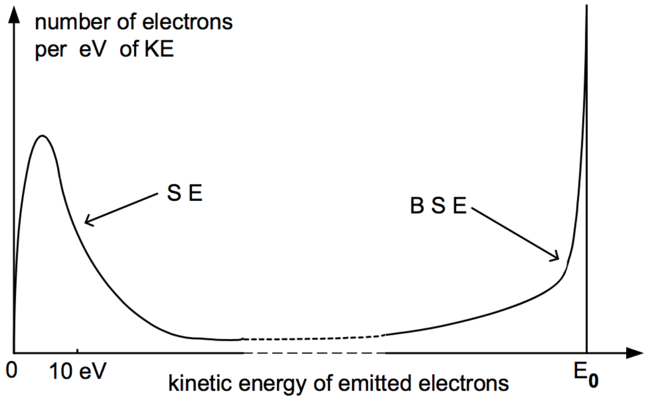

Figure 2.13: Kinetic energy distribution of electrons escaping the sample. The primary beam has energy E_0. A large amount of electrons that escape have only slightly reduced energies and represent BSE. At energies below 50 keV the amount increases again, due to secondary electrons escaping. Figure from [58].

Experimentally, it has been shown that at low energies a huge increase in detected electrons is observed [58], which can be seen in figure 2.13. A secondary electron is an electron that escapes from the sample, with an energy $E <\approx 50eV$. As SE are defined purely on kinetic energy, they can be either a primary electron that, at the ends of it's path, manages to escape from the sample or electrons that are knocked loose from their atom by the primary electron and escapes from the sample. As a primary electron usually experiences several inelastic scattering event, it can produce several SE. Figure 2.14 illustrates a typical scattering process that an electron undergoes upon entering a sample. SE occur at any point on the path of the primary electron, however only those close to the surface will have enough energy to escape the sample (as they have very low kinetic energy). The escape depth is illustrated in figures 2.12 and 2.14.

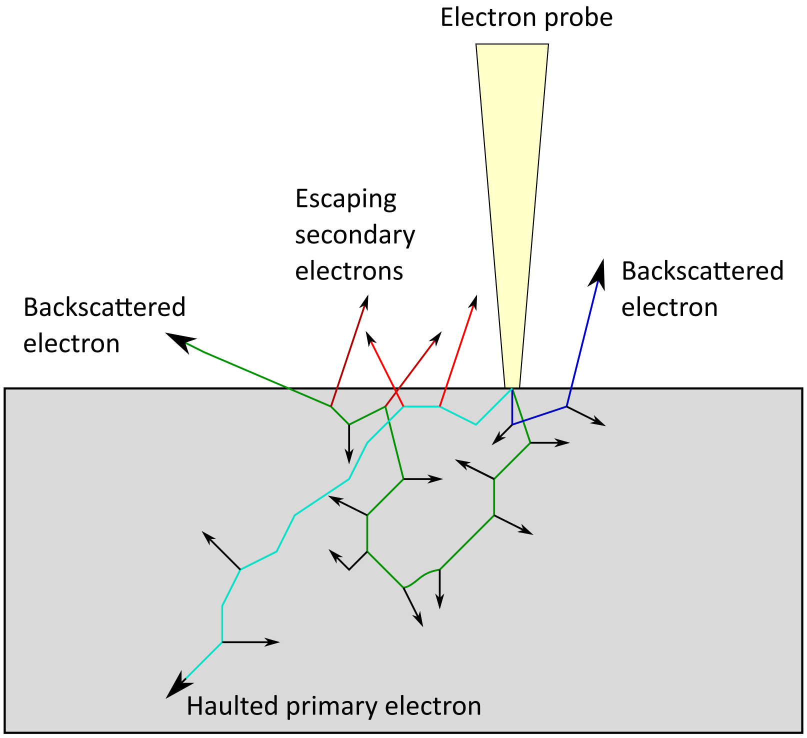

Figure 2.14: Illustration of different scattering events in a material. The green and blue arrow illustrates scattering leading to a emission of a backsacattered lectron, whereas the cyan arrow illustrates absorption of a primary electron through inelastic scattering. The blue arrows are secondary electrons that escape the surface, whereas the black are absorbed secondary electrons.

In general, backscattering and secondary electrons are quantified by the backscatter coefficient, η, and the secondary electron coefficient, δ, respectively. The coefficients are defined as follows:

$$\eta = \frac{n_{BSE}}{n_B} = \frac{i_{BSE}}{i_B} \tag{2.18}$$

$$\delta = \frac{n_{SE}}{n_B} = \frac{i_{SE}}{i_B} \tag{2.19}$$

Where n_i is the amount of electrons of type i, and i_i is the current of electrons of type i.

The backscattered electron yield and secondary electron yield is dependent on many different factors. η depends on atomic number of the investigated sample,the approximate relation is presented by the solid line in figure 2.15. For δ, the dependency is much less pronounced, as shown by the dashed line in figure 2.15. This implies that compositional contrast can be achieved by using a BSE detector rather than a SE detector. Changing the acceleration voltage does not alter the amount of BSE much, but SE show a inverse dependence - lower voltage gives a higher signal, in general [52], until very low energies. Both SE and BSE depend on sample tilt. The amount increases for both with increasing tilt. Tilt can also represent morphological changes, and thus both SE and BSE give morphological contrast. SE, however, gives almost exclusively topological contrast. It is important to note that the backscatter coefficient has a theoretical maximum of 1, whereas the secondary electron coefficient can have higher values.

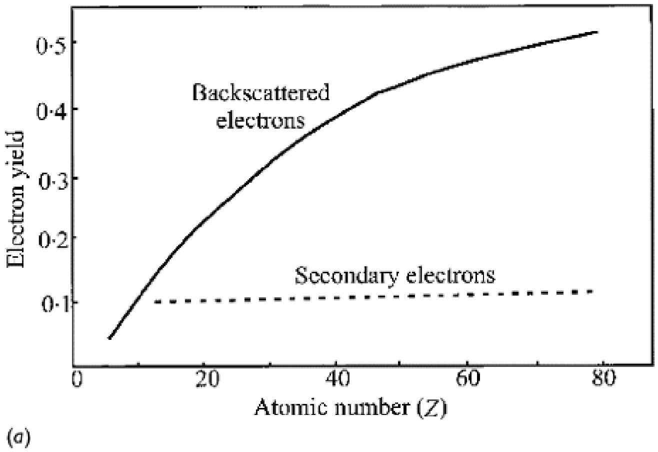

Figure 2.15: Illustration of BSE yield and SE yield as a function of atomic number. Figure from [52].

If the primary electron removes electrons from the sample atoms through scattering, the atoms is left in an excited state. Subsequent relaxation will occur through radiation of characteristic x-rays or auger electrons [59]. Auger electrons can be used in auger electron microscopy, but will not be discussed further here. The x-rays will have energies corresponding to the energy difference between the outer shell and the inner shell that the electron relaxes to. As the energy differences in the shells are characteristic for each atom, the x-rays reveal chemical information. Detection of the x-rays emitted from a sample by electron dispersive X-ray spectroscopy will reveal sharp peaks at the characteristic energies corresponding to the relaxation energies. A typical x-ray spectrum for SiGe is shown in figure 2.16, with very distinct characteristic lines. The characteristic x-rays are named by a Roman letter and a Greek letter. The Roman letter is that of the empty shell, and the Greek letter indicates the origin of the relaxing atom (increasing alphabetically from α with increasing separation). The transitions are governed by a set of selection rules, and are further complicated by the existence of sub-shells, but this is beyond the scope of this thesis. Further information can be found in e.g. chapter 9 of [59].

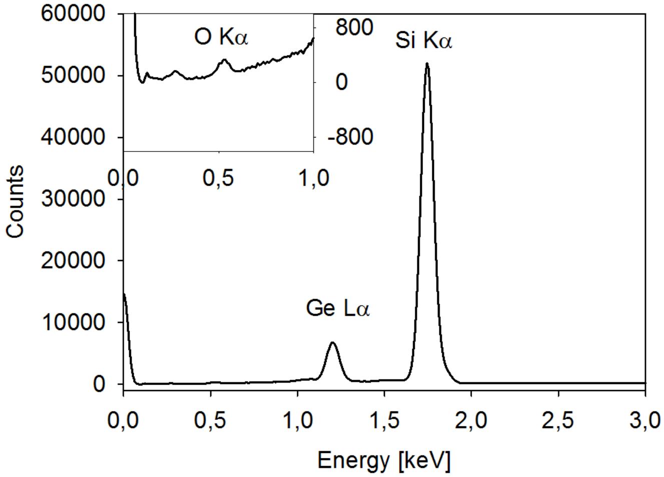

Figure 2.16: X-Ray spectrum captured by EDS for SiGe.

On top of the characteristic lines there is a background spectrum, called Bremsstrahlung. The bremsstrahlung can be emitted when electrons are decelerated in the Coloumbic field of the specimen. The randomness of the deceleration means that the spectrum is a continuum.

2.2.1.2 Scanning Electron Microscope Instrumentation

In section 2.2.1.1 secondary effects were defined as effects caused by the interaction between the electron beam and the sample, that are detectable outside the sample. Attention will now be given to how image formation is done in an SEM and what information is available.

An SEM uses detectors for BSE and/or SE to create an image of the sample. This section will first explain how an electron beam is formed and rastered. The important parameters controlling the beam will be discussed.

The electrons used are created by an electron gun. Thermionic emission from a W filament or a field emission gun are common electron sources. Electrons from the gun are then accelerated over a voltage between 1 kV and 30 kV, reaching an energy between 1 keV and 30 keV, respectively. The electron beam is then focused by a set of electromagnetic lenses. When an electron moving at a speed $\vec{v}$ is exposed to a magnetic field $\vec{B}$, it will experience a force given by:

$$\vec{F} = e(\vec{B} \wedge \vec{v}) \tag{2.20}$$

A small misalignment between the magnetic field and the direction of travel for the electron creates a helical motion along the lens. The helical motion grows tighter as the electron processes, which allows for focusing of the beam into a spot.

The incident beam needs to be as small as possible, and the part impinging on the sample is termed an electron probe. By rastering the electron probe across the surface and detecting SE, BSE or both at each point, a micrograph of the sample is produced. This is illustrated in figure 2.17. Magnification in an SEM is produced simply by reducing the area rastered. The rastering of the beam is done by a set of deflection coils.

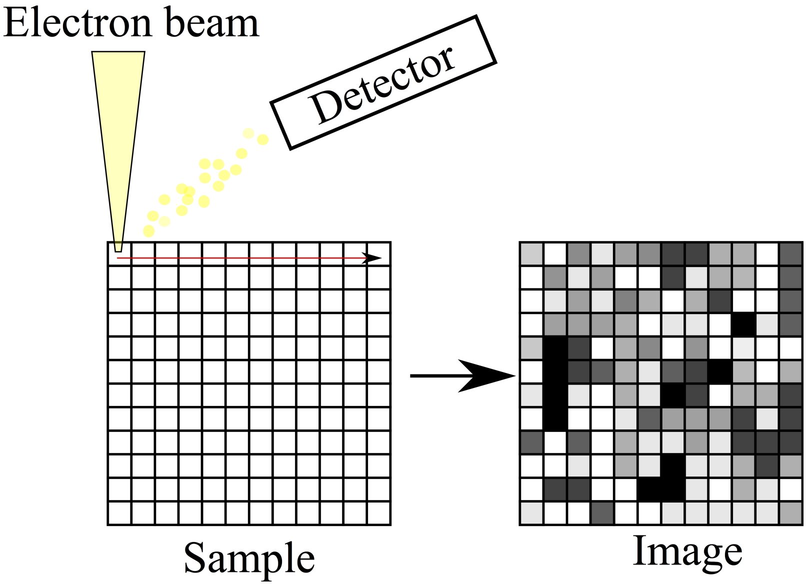

Figure 2.17: schematic overview of the image generation in an SEM. The electron probe is rastered across the sample, generating both SE and BSE. A detector can measure the intensity of SE or BSE at each point and an image is constructed based on the detected intensity. Figure altered an used with permission^1.

As electrons are readily absorbed by most atoms, most SEMs operate in vacuum. The electron column is under continuous vacuum, whereas the specimen chamber can be a direct loading and thus pumped up and down, or loaded using a specimen exchange chamber and thus under continuous vacuum.

There are two kinds of electron detectors used. Secondary electrons can be detected by using an Everhart-Thornley detector. A positively biased grid is used to attract the secondary electrons. Following the grid, the electrons are accelerated over a voltage and hits the detector. The detector is a scintillator, emitting light into a photomultiplier as it is struck by electrons. Back-scattered electrons can be detected by using e.g. a solid-state detector. The detector is placed at a smaller angle to detect the high-energy back-scattered electrons. BSE can also be detected using the Everhart-Thornley detector. In stead of a positively biased grid, it is switched to a negative bias. Now, only the high energy BSE can penetrate, whereas the SE are rejected. BSE and SE detector give very different information due to the different properties of BSE and SE discussed in section 2.2.1.1. Using a BSE detector allows for compositional studies of the sample, and can give pure compositional contrast in a flat sample. SE detectors, on the other hand, will not give much compositional contrast, but in stead almost purely topological contrast.

The performance of an SEM is dependent on the shape of the electron probe. The limiting sharpness and feature visibility depends on four parameters:

d_p The probe diameter. A smaller probe size increases the resolution.

i_p The probe current. Increasing the current means a higher electron density in the beam, which in turn will cause more secondary effects (especially relevant for EDS and BSE). However, sensitive samples can take damage from a high current beam.

α_p The convergence angle. Defined as the half-angle of the probe it determines the depth of focus of the SEM.

V_0 The acceleration voltage. The resolution varies with acceleration voltage as the interaction volume increases with increasing voltage.

An understanding of the four parameters is important both for taking micrographs, but also equally important for the analysis.

2.2.1.3 Electron Dispersive X-Ray Spectroscopy (EDS)

A very important detector available for quantitative SEM analysis is the electron dispersive x-ray spectroscope. As stated in section 2.2.1.1 electrons relaxing can produce X-rays. As x-rays interacts weakly with matter, the sampling volume for x-rays is approximately the whole of the interaction volume. As each atoms produces X-rays of a set of characteristic energies, chemical analysis can be performed by investigating the spectrum occurring from the sample. Both quantitative and qualitative data can be gained by investigating the X-ray spectrum. By measuring the wavelength of the characteristic X-rays that are emitted, qualitative information on what elements the sample contains is achieved. Further investigation on the relative intensities of the lines can give quantitative information on the relative amounts of each element. Quantification of the elemental constituents is usually performed using a ZAF correction. More on the details of automated quantitative analysis and ZAF correction can be found in chapter 9 in **??**.

2.2.1.4 Electron Backscatter Diffraction (EBSD)

EBSD is a technique that can be used in a SEM to determine crystal orientations of a sample across large areas [53]. Polycrystalline materials can consist of same composition grains in different orientations, making it hard to separate grains using conventional SEM. EBSD can then be performed to determine the orientations of the individual grains, as well as any variations within a grain. It can also be used to differentiate between polymorphs of a material [53]. As it is used in an SEM, large areas can be analysed.

EBSD analysis starts with the generation of a EBSD pattern from the sample. The pattern is a diffraction pattern consisting of the kikuchi lines of the different crystal planes. The sample is tilted to a high angle ($\approx 70^\circ$) and bombarded by a high current beam. The backscattering coefficient is high at severe tilting, as explained in section 2.2.1.1, thus increasing the pattern intensity. As the electron beam interacts with the sample, primary electrons can experience inelastic scattering, followed by elastic scattering out of the sample. Every plane in the crystal will diffract the elastically scattered electrons in two flat cones per plane, due to diffraction from the back and front of the atomic planes. The cones are specified by the Bragg angle of the atomic plane. The details behind the formation of the diffraction pattern in EBSD is a complicated topic and will not be covered further.

By using a phosphor screen detector, the EBSD pattern can be detected. As the cones are quite flat, they appear as bands on the detector, termed Kikuchi bands [60]. An example of a Kikuchi pattern from SiGe is presented in figure 2.18. Each of the lines can then be indexed according to the crystal plane that caused it. The distance between a pair of lines is related to the interatomic spacing of the plane. The Kikuchi patters are usually fitted to theoretical models by computers in order to determine crystal structure at each point.

2.2.2 X-ray Tomography (XRT)

X-ray Tomography is probably most known for it's application in medical imaging under the alias CAT-scan, or computer-assisted tomography. It is a powerful technique that uses X-ray absorption and sample rotation to form 3D reconstructions of samples. The model will contain information on composition and density. This section will start with a presentation of relevant theory on the interactions between X-rays and matter. Then the working principles of XRT will be discussed.

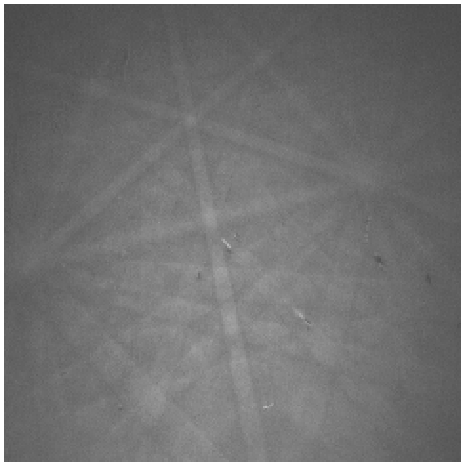

Figure 2.18: Kikuchi pattern from an untreated SiGe fibre. By matching the lines with predicted a theoretical model for SiGe the crystallographic orientation can be determined.

2.2.2.1 X-rays and Matter

For X-ray Tomography, understanding the interactions of X-rays with matter is essential. It is also of interest with respect to EDS, as it determines the sampling depth of EDS. As a beam of X-rays impinge on a sample it is attenuated throughout the sample. There are three mechanism causing attenuation:

- Photoelectric absorption
- Compton scattering
- Pair production

The different mechanisms dominate at different energy regimes of the incoming photon [61]. Photoelectric absorption is when the photon is absorbed by an atom, transferring its energy to an inner electron, thus ejecting the electron with kinetic energy given by:

$$E_k = E_{\text{Photon}} - E_{\text{Binding}} \tag{2.21}$$

where E_{Photon} is the energy of the absorbed photon, and E_{Binding} the energy of the binding energy of the electron. At low energies, photoelectric absorption dominates. At higher energies, Compton scattering becomes the dominant attenuation mechanism. Compton scattering is the inelastic scattering of the photon off an outer electron in an atom. The photon transfers some of its energy and is deflected. The final mechanism is pair production, an event where the energy of an X-ray produces a particle and it's antiparticle. This is only relevant at energies far beyond that used in XRT and will thus not be considered further.

In the energy range used for X-ray tomography, photoelectric absorption will be the dominant attenuation mechanism [61]. Photoelectric absorption is described by the linear attenuation coefficient μ. The attenuation of the beam intensity I through an infinitesimally thin sheet is given by:

$$-dI = I(z)\mu dz \tag{2.22}$$

Solving the differential equation for $I(0) = I_0$ gives the following equation for beam intensity through the sample:

$$I(z) = I_0 e^{-\mu z} \tag{2.23}$$

In order to use X-ray absorption for characterisation, it is helpful to express the linear attenuation coefficient in terms of material properties. In order to do this, we consider the number of absorption events, W, in an infinitesimally thin sheet, given by:

$$W = I(z)\rho_{at} dz \sigma_a \tag{2.24}$$

Where ρ_{at} is the atomic density and σ_a the absorption cross-section. The number of absorption events is proportional to the attenuation, giving:

$$\mu = \rho_{at}\sigma_a = \frac{\rho_m N_A}{M}\sigma_a \tag{2.25}$$

So the linear attenuation coefficient is proportional to the material density and the absorption cross-section. The absorption cross section follows the approximate behaviours given in equation 2.26

$$\sigma_a \propto k^{3-4} \tag{2.26a}$$

$$\sigma_a \propto Z^4 \tag{2.26b}$$

The Z^4 dependency is imperative for imaging as it gives composition contrast. Considering equation 2.25 and equations 2.26 together it is absorption contrast arises from both density as well as atomic number, with atomic number being the most influential parameter by far.

2.2.2.2 XRT Working Principles

An X-ray tomography instrument starts with an electron gun. Electrons are accelerated through an acceleration voltage. The electrons then impinge on a X-ray source, which can be slice of a single material. Different materials are used, depending on what characteristic X-ray spectrum that is wanted (See section 2.2.1.3). Two different sources are usually applied: 1, Reflection sources where the electrons enter on one side and the X-rays that escape form the same side are used, or 2, transmission sources where the electrons bombard a thin slice and the X-ray exiting from the other side are used. A conical X-ray beam is created. The electron beam acceleration voltage will determine the energy of the X-rays, whereas the electron beam current will determine the amount of X-rays. The two parameters must be tuned to achieve a good balance between signal and contrast.

For measurements, the sample is placed in a suitable sample holder in front of the X-ray source. Behind the sample is an X-ray detector. The magnification is directly proportional to the distance between the sample and the X-ray source. The sample is exposed to a uniform cone of X-rays the detector detects the transmitted signal. The detected signal will have interacted with the sample, and an image can be formed based on the attenuation at each pixel. As described in section 2.2.2.1, attenuation is highly dependent on atomic number, but also affected by density. This means that the contrast in signal detected will contain information on composition and density of the sample. By measuring the transmission through the sample at discrete steps during a 2π rotation, a $3D$ model of the sample can be reconstructed. The set-up and process is illustrated in figure 2.19.

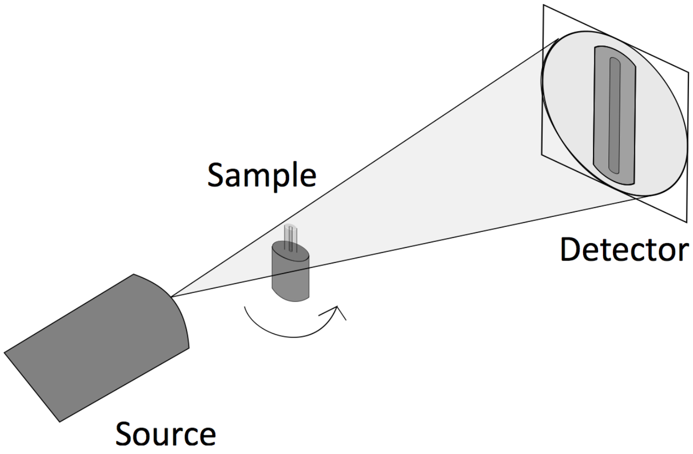

Figure 2.19: A typical XRT set-up with a rotating sample stage. A conical beam of X-rays is emitted from the source and interacts with the sample. The detector measured the attenuated signal. By rotating the sample and capturing images at given intervals, a computer can make a 3D model based on absorption.

2.2.3 µ-Raman

2.2.3.1 The Origin of Molecular Vibrations

Today, there are numerous different characterisation techniques to investigate sample composition. A quick and easy technique is the use of vibrational spectroscopy. The energy of a molecule can, to a first approximation, be divided into four separate components: translational energy, rotational energy, vibrational energy and electronic energy [62]. Chemical compounds are capable of absorbing different ranges of radiation in different ways, through energy transitions in the different energy components [62]. For vibrational spectroscopy it is, as the name implies, absorption due to vibrational transitions that are of interest. The vibrational transitions of a sample are in general unique for that material and acts like a fingerprint. Molecules consist of atoms bound through chemical bonds, and these chemical bonds vibrate. The bonds can stretch, contract or bend in complex vibrations, but the motion can be broken down to normal modes of vibration [62]. A normal mode is when all atoms vibrate with the same frequency and pass through their equilibrium positions simultaneously [62]. The number of normal modes in a molecule relate to the degrees of freedom. A chemical species consisting of N atoms will have $3N$ degrees of freedom. For a molecule in a gaseous state, 3 of the degrees of freedom are prescribed to translation of the molecules centre of gravity. Another 3, or 2 if the molecule is linear, are assigned to rotation around the centre of gravity. The remaining degrees of freedom are termed internal degrees of freedom and correspond to the normal modes of vibration for the chemical species [62]. For a molecule such as CO_2 there will be 4 normal modes, as it is a linear molecule, namely: symmetrical stretching, asymmetrical stretching, and two bending modes in different planes. For solids, the normal modes are represented by phonons in the crystal. Not all transitions in a material are allowed, and it is separated between IR active and Raman active transitions, but a mode can be both as well. The difference is that for a transition to be IR active there can not be a change in dipole moment, whereas for raman active there can not be a change in polarisability.

2.2.3.2 The Raman Effect

There are two main types of vibrational spectroscopy: infra-red and Raman spectroscopy. Both techniques are used to investigate the vibrational states of the sample, thus giving information on composition, and sometimes stress or other parameters. The set-ups are very different, but the main difference is that they excite a different set of vibrational modes. In IR spectroscopy the IR active modes are excited, whereas in Raman the Raman active modes are excited.

Raman spectroscopy is performed by exposing the sample to a strong, monochromatic laser and measuring the scattered signal. Photons from the laser will be scattered in the material. Scattering can occur in different forms, which can be separated into elastic and inelastic scattering. Most of the photons from the laser will be scattered elastically through Rayleigh scattering, but a small amount will experience scattering by the Raman effect. The Raman effect is an inelastic scattering effect where the incoming photon of energy $h\nu_i$ transfers some energy to the scattering molecule, and the scattered photon has the energy changed by $h\nu_s$. The energy changes by an amount:

$$-\Delta E_{photon} = \Delta E_{molecule} = h\nu_i - h\nu_s \tag{2.27}$$

Raman scattering occurs through absorption of the photon, then emission of a new photon. Incoming photons can excite these molecules to high energy level, and they will immediately relax back to the ground state. This is shown in figure 2.20, and represents Rayleigh scattering. However, a small amount of the molecules excited from ground state will, upon relaxation, end up in the state $\nu = 1$. This is illustrated by the red arrow in figure 2.20 The emitted photon will have a lower frequency than the adsorbed. This leads to a shift in wavenumber, resulting in a Stokes line in the spectrum. The green arrows in figure 2.20 illustrate a third possibility; that an excited molecule e.g. state $\nu = 1$ adsorbs the incoming photon. If this molecule then relaxes to the ground state there will be an opposite effect: The frequency of the emitted photon is larger than the incoming. The result is an adsorbtion line at a higher wavenumber than the Rayleigh scattering band, termed the anti-Stokes line. As the amount of excited molecules is fairly low at ambient temperatures, compared to the amount in the ground state, the anti-Stokes lines will be much weaker than the Stokes lines.

As transitions occur between allowed vibrational states only photons matching the frequency $\Delta E_{molecule} = h\nu_{molecule}$ will be absorbed. As the incoming light usually has a much higher frequency than the range of vibrational transitions it will excite the molecule into an unstable, high energy level, shown by a dotted line in figure 2.20. The molecule will immediately relax back into a lower vibrational level. There are two selection rules governing transitions in Raman spectroscopy:

1. Only transitions between adjacent energy levels are allowed:

   $$\Delta\nu = \pm 1 \tag{2.28}$$

2. The transition must lead to a change in dipole moment

   $$\frac{\delta\alpha}{\delta Q} \neq 0 \tag{2.29}$$

   where α is the polarisability and Q is the displacement.

Where ν is the vibrational quantum number and α the polarisability of the state. At ambient temperatures most molecules will be in the level $\nu = 0$.

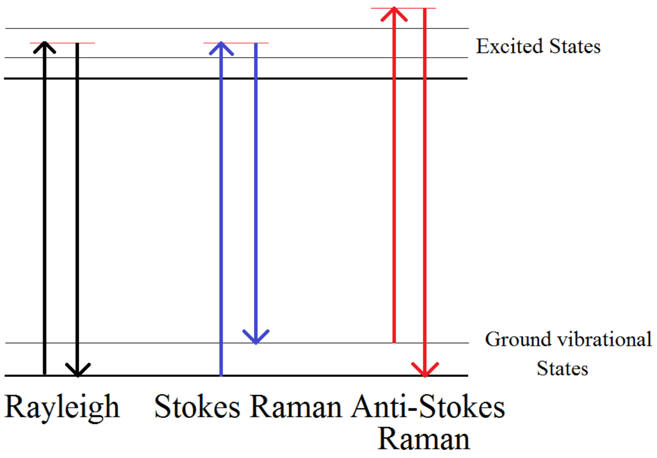
Excited States
Ground vibrational States
Rayleigh
Stokes Raman
Anti-Stokes Raman

Figure 2.20: Absorption of a laser photon and the three relaxation types relevant for Raman spectroscopy.

2.2.3.3 Raman Spectroscopy

The instrumentation for a Raman spectroscope is not particularly complex, and the versatility of the technique is tremendous. A sample stage is usually connected to an optical system for alignment and control. for µ-Raman spectroscopy, a laser is then connected to the optical system to control the location of the exposure. In general, minimal sample preparation is needed. For µ-Raman spectroscopes the optical system allows for the laser to be rastered across the sample, giving the option of Raman mapping.

Chapter 3

Experimental Methods

In this project, SiGe fibres were drawn using two different techniques, in order to produce fibres with different compositions. Additionally, fibres of both compositions were redrawn to give different diameters. The main body of the project has been applying different heat treatments with the goal of recrystallising homogeneous fibres, and characterising the fibres using a set of complementary techniques: SEM, EDS, EBSD, XRT and µ-Raman. This chapter will present the experimental methods used for the drawing of the fibres, the heat treatments and all characterisation techniques used.

3.1 Fibre Drawing

Fibres were drawn both at Clemson University in a fibre tower and at NTNU by hand. The drawn fibres were also redrawn into SiO_2 capillaries to give thinner core fibres. Two different thermal treatments were used on the fibres. This section will start with a sample overview and nomeclature. Section 3.1.2 will the discuss the experimental techniques for drawing at Clemson, and section 3.1.3 will discuss hand-drawing at NTNU.

3.1.1 Samples Overview and Nomenclature

The samples are named using one letter denoting where they were drawn (”C” for Clemson, ”N” for NTNU), a second letter to distinguish between as-drawn, ”A”, and redrawn, ”R”. A third letter is given based on treatment: ”O” for tube furnace, ”L” for laser. Finally, the samples are given numbers to separate between similar experiments. For the laser annealed samples, the number represents the scan velocity in $\mu m\,s^{-1}$, separating multiple samples of the same velocity by an additional number. When discussing specific samples they will be referred to by full name, e.g. CAL1000-1 or NRL100-1. When discussing trends, whole batches can be addressed with e.g. CR meaning all redrawn fibres from Clemson.

3.1.2 Clemson Fibres

Fibres were drawn using a fibre tower at Clemson University by the molten core fibre drawing method [27] [63] [64]. The procedure is similar to the drawing procedure for optical fibres, but instead of a SiO_2 cylinder, a hollow tube is used. A procedure used for drawing Si microwires [27] was slightly altered to allow for SiGe microwires to be drawn. The cylinder was filled with SiGe. CaOH was used as an interface modifier to improve the quality of the fibres [63]. By heating the material to approximately 2000 °C the SiO_2 becomes suitably ductile and drawing can commence. As the melting point of SiGe is lower than that of pure Si, the core will be well molten when the SiO_2 is ready. When drawing of the SiO_2 commences the SiGe will follow inside the hollow SiO_2 tube. The fibre is molten until the final diameter is reached and then solidifies, meaning that despite compositional variances within a cross-section, the global composition is constant. The result is a SiGe fibre with a SiO_2 cladding.

The resulting fibres have the composition given in table 3.1. The composition was measured by EDS, within the yellow circle marked in figure 3.1a. The spectrum used for quantification is given in figure 3.1b. The compositions does, however, vary within a fibre. More on this in section 4.2.

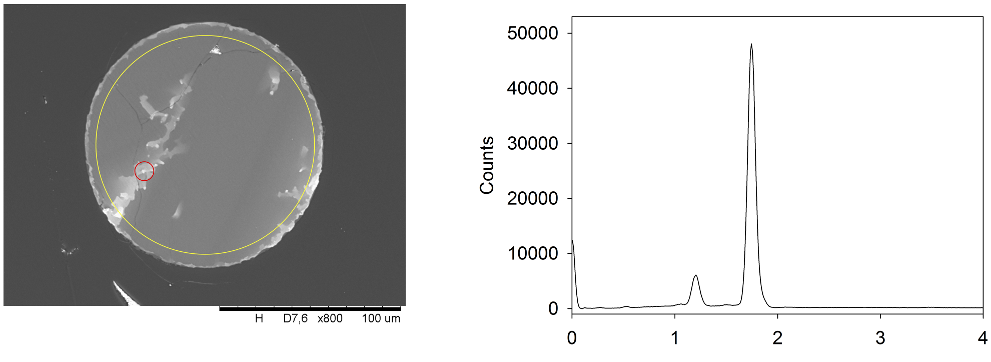

(a)

(b)

Figure 3.1: BSE SEM image of the untreated CA cross-section used for EDS analysis (a). The analysis was done within the yellow circle, and the resulting spectrum is presented in (b). EDS quantification was also done for the Ge-rich area marked by the red circle in figure (a).

EDS mapping was performed on a cross-section of an untreated sample, and the maps are presented together with a BSE SEM micrograph in figure 3.2. Figure 3.4a shows an inhomogeneous fibre core, and consulting figures 3.4b and 3.4c confirms that the untreated fibres have inhomogeneous composition, with Ge rich areas randomly distributed. Figure

Table 3.1: Composition of Clemson fibres.

Element	at%	Error in %
Si	91.7	3.4
Ge	5.3	0.7
O	3.0	0.2

3.4d shows the distribution of Ca. As CaOH is used as a coating material for the fibre tower drawing, the Ca is located at the interface of the core and the SiO_2.

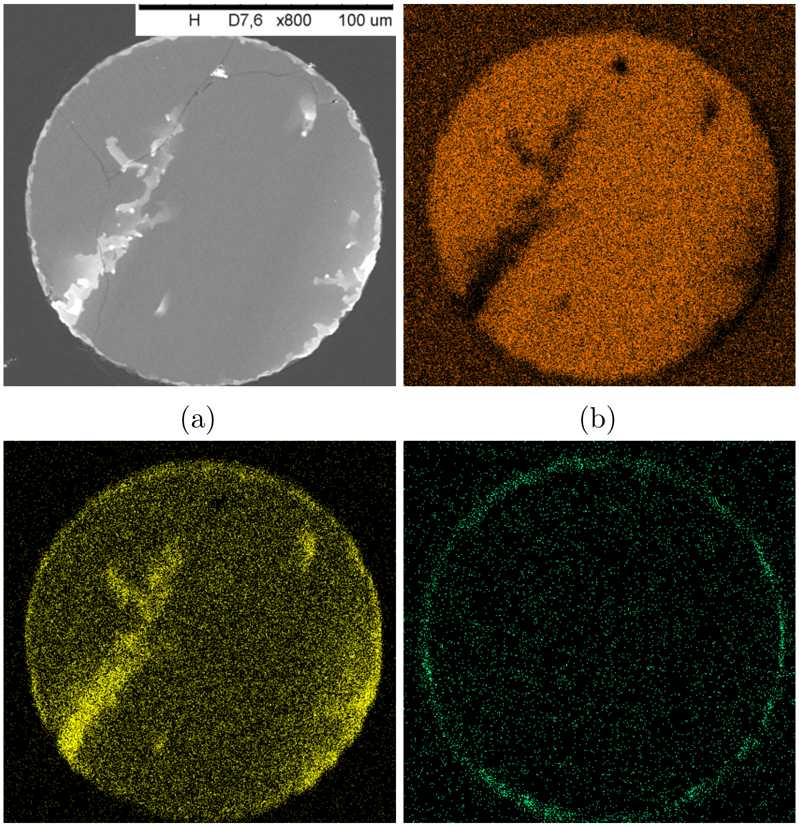

(a) (b)

(c) (d)

Figure 3.2: BSE SEM micrograph of a representative untreated section of a CA fibre (a) and corresponding elemental maps of Si (b), Ge (c) and Ca (d). There is a clear inhomogeneiety in the Ge and Si distribution. Ca is localised at the core/cladding interface.

EDS quantification of a Ge-rich area was performed, as marked by the red circle in figure 3.1a, giving a Ge content of approximately 20at%. This indicates that the variations in composition seen in figure 3.4a are severe.

Thinner samples of the same composition were prepared by redrawing the fibres at the NTNU Glassblowing Workshop. This was done by taking a small piece of original fibre and placing it in a quartz capillary. The capillary was then heated using an H_2-torch until the SiGe was suitably molten. Drawing was then performed by hand. More on the details of hand drawn fibres is given in the following section. The resulting CR fibres had a core of approximately 8 µm, as seen in figure 3.3.

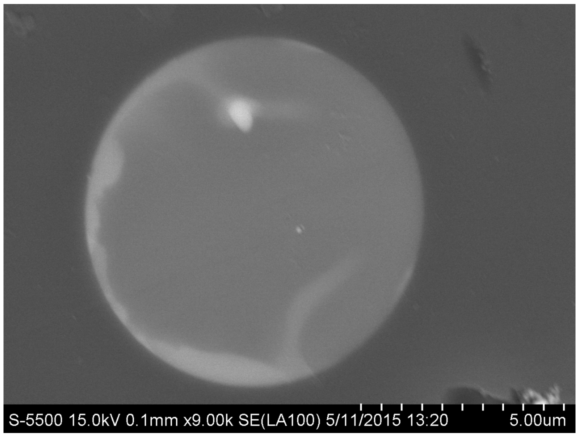

Figure 3.3: Cross-sectional LA-BSE micrograph of a clemson fibre redrawn into a quartz capillary. As for the CA samples, the Ge distribution is inhomogeneous.

3.1.3 NTNU Fibres

Several fibres were drawn at the NTNU Glassblowing Workshop as a way to test other compositions without doing long draws in the fibre tower.

Optical grade Si windows and optical grade Ge windows from CRYSTRAN was used as source material for the fibres. The Si and Ge were cleaned with a 5 min sonication bath in acetone, followed by a 5 min sonication bath in iso-propanol. The Si and Ge were then dried using a N_2-gun. Two batches of approximately $Si_{0.5}Ge_{0.5}$ were then prepared, using the amounts given in table 3.2. The material was placed in a BN-cruicble and inserted to a vacuum chamber and pumped down to 3×10^{-5} Pa. The BN crucible was chosen due to its chemical inertness [8], as molten Si is highly reactive. The two batches were melted by resistive heating of the crucible. This was done with a W filament holding the BN crucibles. The alloyed material was then crushed to make it easier to handle.

Table 3.2: Parameters used for the production of the source alloy used for drawing of the NA fibres.

	Batch A	Batch B
Weight Si [g]	0.039	0.025
Weight Ge [g]	0.096	0.063
Calculated at% Ge	48.9	49.7
Pressure [Pa]	$3 \cdot 10^{-5}$	$3 \cdot 10^{-5}$
Current [A]	75	70

Fibre drawing of SiGe requires a cladding material. In this thesis SiO_2 tubes were used. The inside of the tubes were coated to improve the quality of the fibres. A mixed coating using CaOH, $CaCl_2$ and spin-on glass was used.

A suitable amount of the crushed alloy was loaded into the quartz tubes. A steady flow of Ar was introduced to avoid oxidation during melting. A H_2-torch was used to melt the alloy in the tube, and a glass rod was connected to the end of the tube. When the solid was suitably molten the fibre was drawn. The composition of the drawn fibres were evaluated by EDS, and is presented in table 3.3. An BSE SEM micrograph and elemental EDS maps of a representative fibre is shown in figure 3.4.

Table 3.3: Composition of an NTNU drawn fibre.

Element	at%	Error in %
Si	56.4	1.3
Ge	41.7	3.4
O	1.9	0.2

There is a clear compositional non-uniformity in the fibres. Based on the structure of the Ge-rich sections, it seems to be dendritic growth in the fibres. This is understandable, as such high Ge-content would easily give severe constitutional undercooling and the high growth rates occurring in fibre drawing by hand.

Smaller core fibres were prepared by redrawing small pieces of successfully drawn fibres. Small pieces were cut out and loaded into thin quartz capillaries. Again, the alloyed fibre was melted using a torch and drawn when suitably molten. An example of a redrawn fibre is presented in figure 3.5.

It is important to note that the redrawn fibres, the inner glass fibre containing the core, is not in full contact with the quartz capillary used for the redrawing process. This can alter the thermal properties of the system during recrystallisation. The irregular shape of the core, might be a consequence of the drawing being done by hand or the change in thermal conductivity due to the existence of a gap.

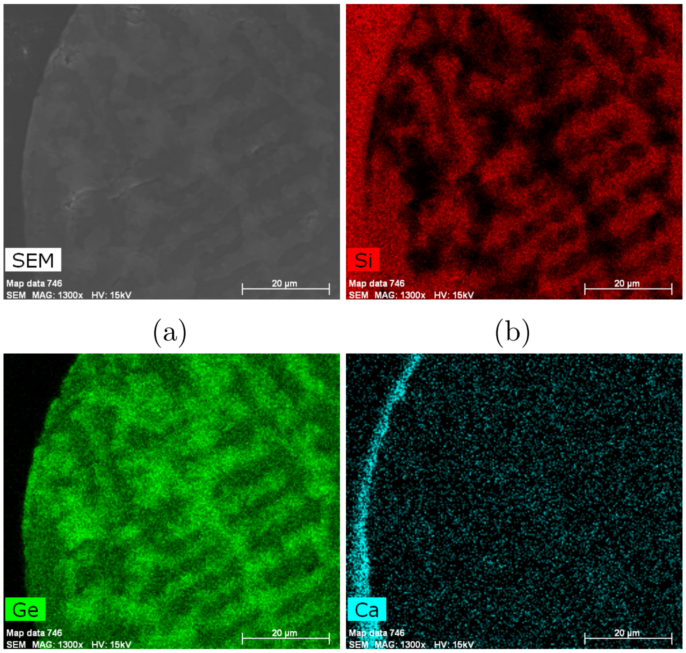
SEM
Map data 746
SEM MAG: 1300x HV: 15kV
20 µm
Si
Map data 746
SEM MAG: 1300x HV: 15kV
20 µm
Ge
Map data 746
SEM MAG: 1300x HV: 15kV
20 µm
Ca
Map data 746
SEM MAG: 1300x HV: 15kV
20 µm

(a) (b)

(c) (d)

Figure 3.4: BSE SEM micrograph of a reresentative untreated section of a NA fibre (a) and corresponding elemental EDS maps for Si (b), Ge (c) and Ca (d). The composition of the fibre is given in table 3.3. The growth structure appears to be dendritic with large compositional variations.

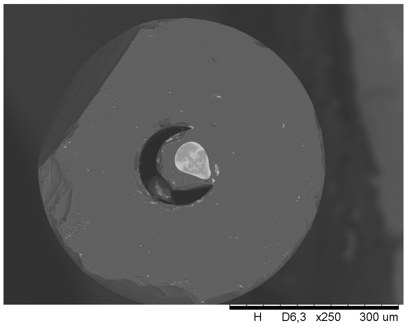
H D6,3 x250 300 um

Figure 3.5: Cross-sectional micrograph of an NR fibre. The inner glass circle is form the original fibre and the outer is the SiO_2 capillary used for the redrawing process.

3.2 Heat Treatments

The inhomogeneity of the as-drawn and redrawn fibres is clearly demonstrated in sections 3.1.2 and 3.1.3. Recrystallisation was done using two different heat treatments: 1, solidification in a tube furnace by homogeneous cooling and by 2, travelling melt zone method using a CO_2 laser. The following sections will describe the two set-ups, as well sa the procedures used.

3.2.1 Tube Furnace

A GSL-1500X High Temperature Gas tube furnace was used for recrystallisation experiments by slow solidification of the melt, by homogeneous cooling of the system. The samples were mounted in batches of four, using the set-up illustrated in figure 3.7. Each sample is given a letter based on their position, as shown in figure 3.7. Ta wire was used to stabilise the samples to a Al_2O_3 ceramic boat. Four different samples were tested in each case in order to investigate any possible effects due to gravitation or inhomogeneous cooling due to location relative to boat, as well as off-centre placement in the oven. The sample holder was placed in the middle of the furnace. Two porous, ceramic bricks were placed to block one end. An Ar flow of $1\,\mathrm{L\,min^{-1}}$ was used to minimise oxidation.

Two different programs were used. Table 3.4 summarises the programs used, and figures 3.13a and 3.13b illustrate the programs. All runs were initiated by 60 min dehydration at 120 °C, as well as a 120 min stay at 350 °C to prepare the heating elements for the high temperatures. These steps were suggested by the producers [1]. The two programs have different cooling rates, as well as a shorter stay at the maximum temperature for program A. The shorter stay in program A is to avoid prolonged exposure to high temperatures, as SiO_2 may get damaged. A total of 16 samples were tested, batches CAO1 and CAO2 for program A, and CAO3 and CAO4 for program B.

---

[1] GSL-1500X User Manual

Table 3.4: Summary of the two different heating procedure used in the tube-furnace. The time is how long spent from steps $i-1$ and i.

	Program A		Program B	
Step	Set temperature [°C]	Time [min]	Set temperature [°C]	Time [min]
1	120	15	120	15
2	120	60	120	60
3	350	60	350	60
4	350	120	350	120
5	1000	90	1000	90
6	1430	90	1430	90
7	1430	10	1430	30
8	1200	153	530	180
9	530	120	-	-

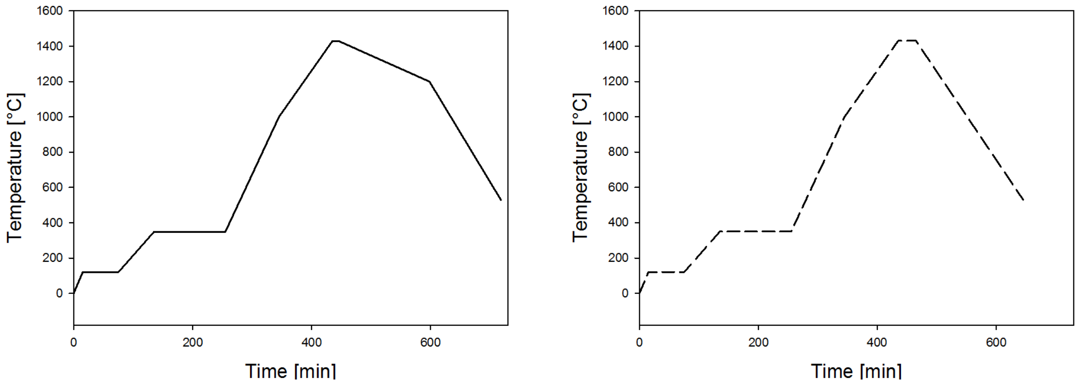

(a) (b)

Figure 3.6: Temperature profiles for the slow cooling program A (a) and the fast cooling program B (b) in the tube furnace.

3.2.2 CO_2-laser

Recrystallisation by zone melting was done using a Universals Laser Systems URL-25 CO_2 laser. The laser has a wavelength of 10.6 µm and a maximum power of 28 W. The fibre consists of a semiconductor core and a glass cladding. At 10.6 µm the semiconductor core is mostly transparent, whereas the cladding is opaque. This means that the cladding will be heated directly, whereas the core will be heated only indirectly from the cladding. The fibres were mounted on a stage using magnetic holders, as illustrated in figures 3.8. The

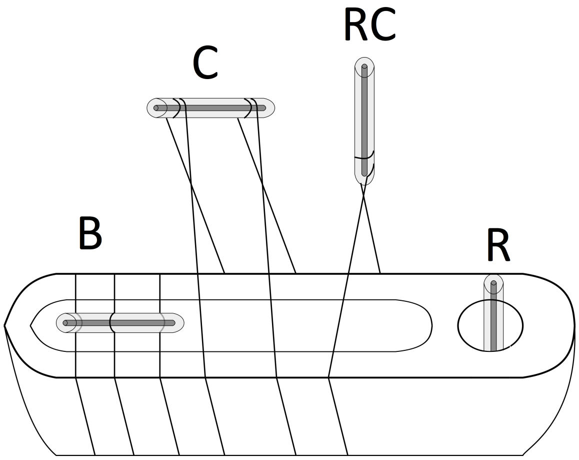

Figure 3.7: Schematic of the different sample placements on the ceramic boat for the tube furnace experiments. The different placements were chosen to investigate correlations between compositional distribution with respect to horizontal or vertical placement, as well as whether placement inside the oven had any effect.

laser was focused with a lens of focal length 5 cm. Two step controllers were connected; one to translate the laser along the axis of the fibre, and one to adjust the focal plane of the laser. The last stage allowed for adjustments in power through a change in focus, rather then changing the output of the laser, avoiding instabilities in the laser that arises when changing power. The laser was off focus by approximately 12 mm. The power of the laser was controlled, in combination with adjusting the focal length in order to obtain a melt zone of approximately 0.5 mm for each sample. A shutter was connected to the laser to control exposure time. A *B&W* camera was used, and controlled by use of Thorlabs software. Two different removable narrow band filters were attached to the camera detector; 514 nm and 635 nm, allowing for determination of thermal gradients in the fibre, as done in section 4.1.3. The set-up is illustrated in figure 3.8. With the camera it was clearly visible when a melt zone was formed, as shown in figure 3.9. The slant of the interface is due to the laser hitting one side of the fibre, resulting in an uneven heating profile. The camera was used to make sure the melt zone was stable before translation started.

Several different translation velocities were tested in order to determine the critical growth velocity in the fibres. It should be noted that the slowest rate of $10\,\mu\text{m}\,\text{s}^{-1}$ corresponds to $36\,\text{mm}\,\text{h}^{-1}$, which is approximately 10 times the rates for bulk growth. Four sets of fibres were tested: CAL, CRL, NAL and NRL. Table 3.5 summarises the experiments

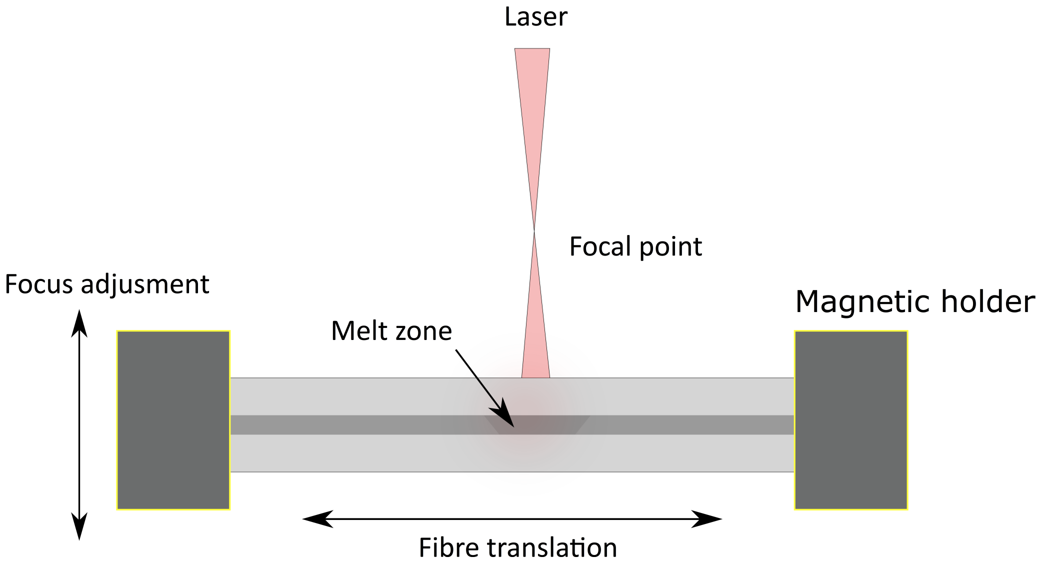
Laser
Focal point
Focus adjusment
Magnetic holder
Melt zone
Fibre translation

Figure 3.8: Schematic of the annealing set-up for travelling zone recrystallisation by use of a CO_2 laser. The fibre is held by magnetic holder and the sample stage with two step-controllers to translate the fibre and focus the laser.

performed on each set of fibres.

Table 3.5: Summary of the different scan velocities tested for the different samples. Each velocity tested will be marked by the sample name, and velocities not tested are marked by "-".

Samples	10	50	100	1000	3000
CAL	10-1	-	100-1	1000-1	-
CAL	10-2	50-1	100-2	-	3000-1
CRL	10	-	100	1000	-
NAL	10	-	100	-	-
NRL	10	50	100	1000	-

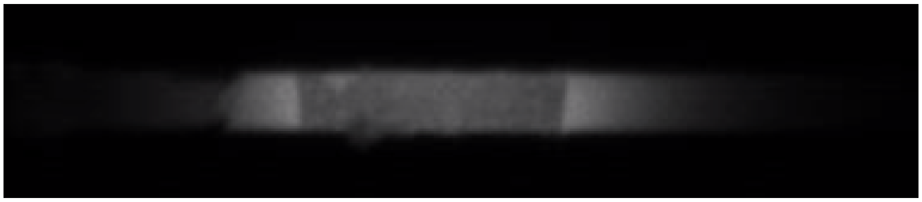

Figure 3.9: Image captured using the camera in the CO_2 set-up. The melt zone is clearly visible due to the difference in emissivity of the liquid and solid phase. The camera was placed perpendicular to the laser axis.

3.3 Characterisation Techniques

Several different characterisation techniques have been applied in order to assess the success of the thermal treatments. This section will first describe any required sample preparation prior to any characterisation. All experimental details for the characterisation techniques used will then be presented. Section 3.4 will discuss the MATLAB script (appendix A) used for analysis of the SEM s to analyse the Ge distribution, as well as present examples to show its function.

3.3.1 Sample Preparation

For investigations of cross-sections of the fibres the samples were cut and polished. Coarse sandpaper was used to level the face of the fibre, then a fine grit was used to polish it. The results was evaluated continuously in an optical microscope and polishing continued until the results were satisfying. As the aim of doing SEM with a BSE detector is to get compositional information, any topographic contrast should therefore be minimised. By doing a thorough polish to ensure a flat surface, the only contrast will will be due to compositional variances. The samples were cleaned prior to characterisation with 5 min sonication in acetone, followed by 5 min sonication in iso-propanol was used. The samples were then dried with an N_2-gun.

3.3.2 SEM+EDS

Prior to SEM investigation, a 4 nm coating of Pt/Pd was applied using a Cressington 208 HR B sputter coater. This was performed to prevent the samples from charging.

BSE micrographs of the larger core samples were obtained using a Hitachi TM3000 SEM. The samples were loaded on a cross-section stage and mounted at a working distance of approximately 4 mm for micrographs. For EDS, the working distance was increased to 7 mm in order to maximise the EDS signal. For cross-section images an acceleration voltage of 15 kV was used, as this increases the penetration depth, giving a more representative composition average. As the features are fairly large (no need for super high resolution), the "Analy" mode was used, which increases the aperture [2] and thus the current, increasing the signal from the sample. Micrographs were captured using the Hitachi TM3000 software. For EDS, the Quantax 70 software was used.

The small core fibres were investigated using a Hitachi S-5500 S(T)EM. A standard holder was used, but the samples were mounted so to expose the cross-section. The sample was loaded through the sample exchange chamber. For imaging, an acceleration voltage of 15 kV and a current of 15 µA was used. A low-angle BSE detector was used, with 100% BSE detection. The probe mode was set to "Analysis" for all micrographs to increase signal, without disturbing the resolution as the cores are relatively large. For EDS measurements, the current was increased to 20 µA to increase signal strength, and DBC scan mode was used to minimise noise. The EDS detector was injected for the measurements, and the collection was controlled using ESpirit 1.9.4.

It is important to take the electron range into consideration when performing EDS measurements, as it determines the resolution of the measurements. The electron range of at 15 kV can be calculated using equation 2.17. By using the molar mass, atomic number and density of Si, an electron range of $R_{\mathrm{KO}}^{\mathrm{Si}} \approx 2.97 \mu m$. Calculating the same for pure Ge gives $R_{\mathrm{KO}}^{\mathrm{Ge}} \approx 1.59 \mu m$. The range for the SiGe alloys considered in this thesis will lie somewhere in between the two maxima. For the cross-sectional analysis, quantification was done in restricted circular areas. For homogeneous samples, having borders too close to the core/cladding interface will result in higher O count, as the interaction volume will stretch into the interface modifier and SiO_2-cladding. The change is approximately 1at% from inclusion of the interface, which is shown in appendix C. Additionally, for inhomogeneous samples, such as the fibre in figure 3.2, the measured composition will depend on the quantification area. These two factors will add to the error of the calculations.

3.3.3 Electron Backscattered Diffraction

EBSD was performed using a ZEISS Ultra with an attached EBSD detector. The samples were mounted on a sample stage and tilted at a 70° angle relative to the beam direction. An acceleration voltage of 20 kV was used with an aperture opening giving 60 µA. A frame rate of 30 fps with an exposure time of 33 283 µs was used for acquisition. The Kikuchi pattern was then analysed using NTNU written software. The imaged areas were limited due to charging, but manual investigation the entire fibre face was done for all characterised samples.

---

[2] TM3000 User Manual

3.3.4 X-Ray Tomography

X-Ray Tomography was performed using a Nikon XT H 225 ST, controlled with the Nikon Inspect-x software. Nikon CT-Pro 3D was used for reconstruction and Volume Graphics VG Studio Max for furthr treatment. The reference sample was placed in a hollow Al_2O_3 tube, attached to a standard holder. The sample of interest was then placed on top of the reference and placed onto the sample stage. The sample holder was then moved to a distance of X from the source. A reflection source was used, with a tungsten element, to produce X-rays. Prior to starting the measurement, a calibration was done using three intensities. The calibration measures the detected signal at full, half and zero beam intensity. The measurements were all performed using an acceleration voltage of 110 kV, and a power of 120 µA. 3000 projections was used.

3.3.5 µ-Raman

3.3.5.1 Experimental Procedure

µ-Raman spectroscopy was performed using a Renishaw InVia Reflex Spectrometer System, with a 532 nm laser as the excitation source. The laser power was 45 mW. The samples were mounted on a sample holder, exposing the cross-sections to the optical axis. The built-in optical microscope was used to align the sample and adjust the focus. 50x was used for all measurements, unless otherwise stated. For single spectrum acquisition the laser power was set to 50%, using a exposure time of 3 s and a single measurement. Raman mapping was done with the same settings as for a single spectrum acquisition, but with the exposure time reduced to 2 s to reduce the acquisition time. A scan resolution of 1 µm was used in both the x and y direction. For accurate line scans, the resolution was reduced to 0.5 µm.

3.3.5.2 Strain-analysis by µ-Raman

µ-Raman is most commonly used for compositional analysis, but it can also be used to analyse strain in the material [62]. As strain in a material changes the bond distance, it will also change the scattered signal from the sample. Raman spectroscopy is commonly used for strain analysis of Si integrated circuits [65]. For the last couple of decades, µ-Raman spectroscopy has been used for analysis of strain and composition in SiGe thinfilm heterostructures [66][67] [68]. More recently, investigations into built-in strain in multicrystalline SiGe with large compositional variations have been performed [69].

Peaks in a Raman spectrum can experience two effects: a shift in peak position or a change in intensity. For SiGe, the relative integrated intensity between the peaks give the composition of the sample [70]. The relevant peaks for SiGe are the Ge−Ge peak at around 300 nm, the Si−Ge peak at around 400 nm and the Si−Si peak at around 520 nm. A typical SiGe raman spectrum is presented in figure 3.10, with the relevant peaks marked.

Assuming a random alloy with nearest-neighbour interaction, the intensity of the peaks should follow equation 3.1 to a first order approximation [68].

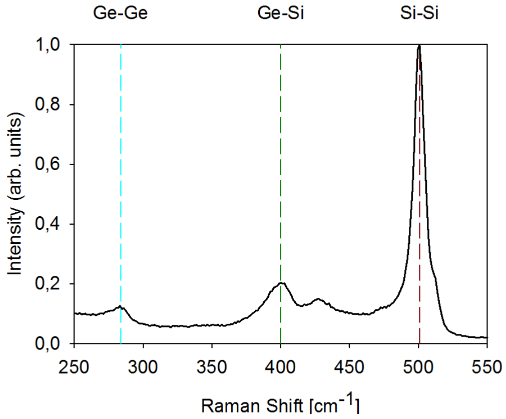

Figure 3.10: Raman spectrum of a SiGe sample. The Si–Si peak is well defined, whereas the Ge–Si and Ge–Ge peaks less intense and have a much higher FWHM.

$$I_{\text{Si}-\text{Si}} \propto x^2 \tag{3.1a}$$
$$I_{\text{Ge}-\text{Ge}} \propto (1-x)^2 \tag{3.1b}$$
$$I_{\text{Si}-\text{Ge}} \propto 2x(1-x) \tag{3.1c}$$

The ratio of the integrated intensities can then give the composition. Equations 3.2 and 3.3 gives the expected relative intensities of the peaks [70].

$$\frac{I(\text{Si}-\text{Si})}{I(\text{Si}-\text{Ge})} = \frac{A(1-x)}{2x} \tag{3.2}$$

$$\frac{I(\text{Ge-Ge})}{I(\text{Si-Ge})} = \frac{Bx}{2(1-x)} \tag{3.3}$$

Where A and B are wavelength dependent constants.

The shift of peak positions depends on both composition and strain. Equations 3.4 give the dependency on peak position for the Si–Si, Si–Ge and Ge–Ge peaks on composition and strain [70].

$$\omega_{\text{Si}-\text{Si}} = 520.0 - 70.5x - 830\epsilon \tag{3.4a}$$
$$\omega_{\text{Si}-\text{Ge}} = 400.5 + 16x - 575\epsilon \tag{3.4b}$$
$$\omega_{\text{Ge}-\text{Ge}} = 284.7 + 16x - 384\epsilon \tag{3.4c}$$

Where ϵ is the strain, defined as:

$$\epsilon = \frac{\delta l}{l_0} \tag{3.5}$$

where l_0 is the initial bond length and δl the change in bond length. Equation 3.4c has been adjusted to the results of Parker *et al.* [71].

From equations 3.4a and 3.4b an expression for both composition and strain can be derived. Equation 3.6 gives the composition based on the shift in the Si−Si peak and the Ge−Ge peak. The strain is given by equation 3.7.

$$x = \frac{(\omega_{\mathrm{Si-Ge}} - 400.5) - 0.6928 \cdot (\omega_{\mathrm{Si-Si}} - 520)}{64.84} \tag{3.6}$$

$$\epsilon_{\mathrm{SiGe}} = \frac{520 - \omega_{\mathrm{Si-Si}} - 70.5x}{830} \tag{3.7}$$

Determining the peak position requires a lot of care, as peak fitting of with background subtracion is a major source of error, especially for the less intense peaks [70].

3.3.5.3 Standards

Four standard samples measured to calibrate the system:

- CRYSTRAN Si window
- CRYSTRAN Ge window
- Si fibre
- Ge fibre

All measurements were performed using the 532 nm laser at 50% with a collection time of 2 s. The results from the Ge and Si samples are presented in figure 3.11 and 3.12, respectively. The peaks presented in figures 3.11 and 3.12 were peak fitted and the fitted peak positions and FWHMs are presented in table 3.6. In 1967, Parker *et al.* determined the peak of pure Si to be 520.2 cm^{-1} ± 0.5 cm^{-1} and the peak of pure Ge to be 300.7 cm^{-1} ± 0.5 cm^{-1}. An

Table 3.6: Peak position and FWHM for the main peaks of all the calibration samples.

	Peak position	FWHM
Si Window	520.5	4.1
Si Fibre	521.5	3.8
Ge Window	301.6	5.5
Ge Fibre	300.0	4.6

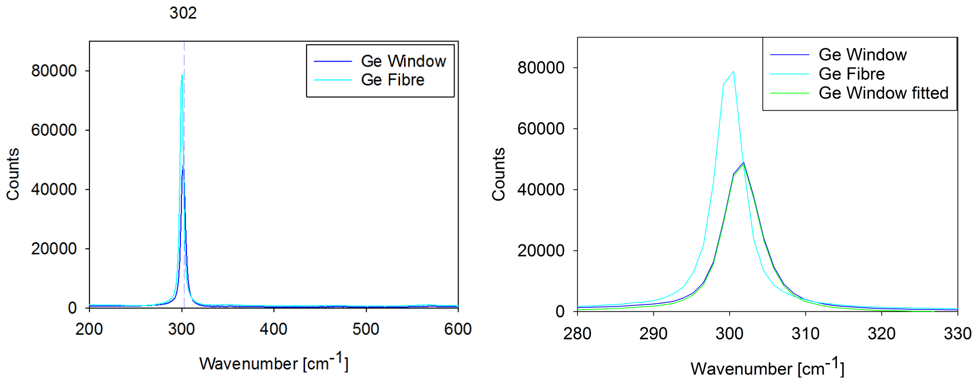

(a) (b)

Figure 3.11: Raman spectra for the pure Ge window and pure Ge fibre. A fitted peak for the Ge window is added to illustrate the fit (green line), though both spectra were peak fitted.

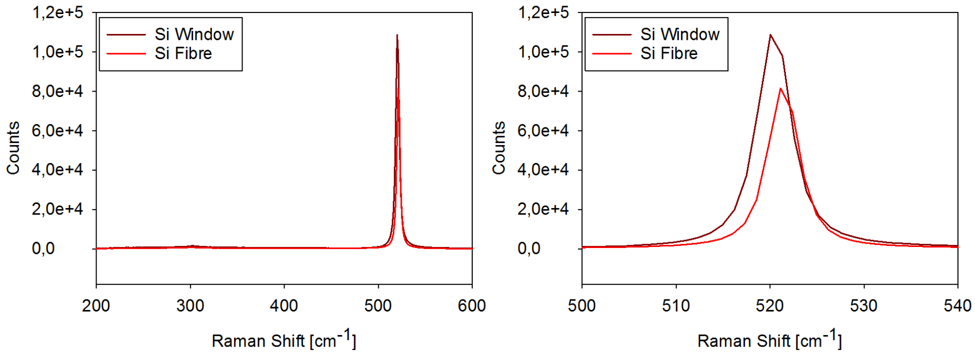

(a) (b)

Figure 3.12: Raman spectra for the pure Si window and pure Si fibre.

opposite shift is observed in Si and Ge for window versus fibre. The Si window is within the uncertainty given by Perker *et al.*. By using equation 3.4a and $x = 0$ for Si, the strain in the Si fibre is calculated:

$$\epsilon_{\text{Si}}^{\text{Fibre}} = -0.00181 \pm 0.0001 = -0.18\%$$

As the value for strain is negative, it represents a small compressive strain. Calculating the same for the Ge window and Ge fibre using $x = 0$ gives:

$$\epsilon_{\text{Ge}}^{\text{Fibre}} = 0.00181 \pm 0.0002 \approx 0.18\%$$

$$\epsilon_{\text{Ge}}^{\text{Window}} = -0.00287 \pm 0.00003 \approx -0.29\%$$

The uncertainties were calculated by performing the measurements at three locations for each sample. Especially for the wafer, the error is far smaller than the resolution of the instrument. This suggests that there is a slight tensile strain on the Ge fibre, whereas a compressive strain for the Ge window. As the Ge window is supposedly strain-free, this suggests that the Ge peak is slightly off-set for the instrument. As both Ge and Si expand upon solidification [72], a compressive strain would be expected. As the Si peak is in agreement with literature [71], it will be used for all further calculations.

3.3.5.4 Strain Calibration in SiGe

As discussed in section 3.3.5.2, the Raman spectra of SiGe contain information on both strain and composition. For the low Ge content samples, separating the effects from strain and composition is difficult. This is due to the fact that determination of the composition alone, using the integrated intensities, is very hard and inaccurate due to the very weak intensity and broad shape of the Ge−Ge and Si−Ge bands at low Ge contents [70]. This also makes it very hard to determine their shift. The result is that only the Si−Si peak is well-defined and can be used for analysis, meaning that it is not possible to separate the effect of strain and composition. However, strain can be analysed by determining the composition by the use of a complimentary technique. EDS was used to determine the composition of the sample in the area marked in figure 3.13a. The composition of Ge was determined to be 5.45at%. The peak position can be determined by considering the

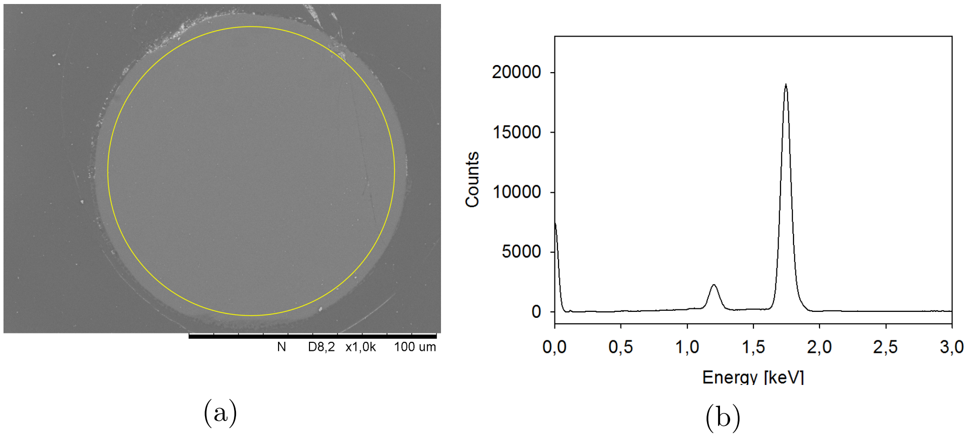

(a) (b)

Figure 3.13: Image of the quantified region of sample CAL100-1 used for strain calibration (a) and the corresponding EDS spectrum (b).

spectrum in figure 3.14 and performing a peak-fit, giving a Si−Si position of 514.1 cm^{-1}. Inserting the composition determined by EDS into equation 3.4a gives:

$$\epsilon = 0.00247 \pm 0.0003 \approx 0.25\%$$

This means that the fibre has a small amount of tensile strain. The maximum strain for epitaxially grown SiGe is $\epsilon = 0.0417$ [68].

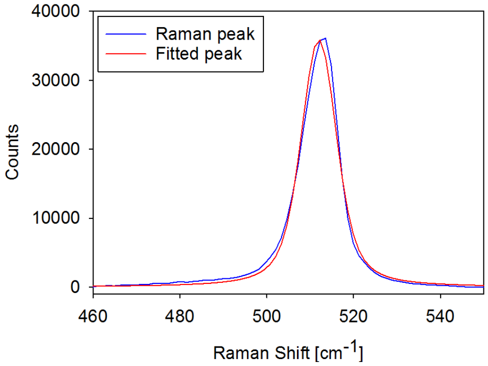

Figure 3.14: Raman spectrum for the CAL100-1 sample (blue) and a fitted curve (red).

3.3.5.5 Spot Size Measure

The spot size was experimentally determined as it is important when considering the resolution of the instrument. A line scan was done over the edge of a pure Si wafer. The 532 nm laser was used at 50% at 50x magnification, using a collection time of 1 s and a step size of 1 µm. The intensity of the Si peak at 520 cm^{-1} is plotted as a function of scan step in figure 3.15. The spot size is determined by considering the area between 10% and 90% of maximum intensity, resulting in an approximate peak diameter of 4 µm. This is of similar size to the diameter of the spot size for SEM as calculated by the electron range in equation 2.17.

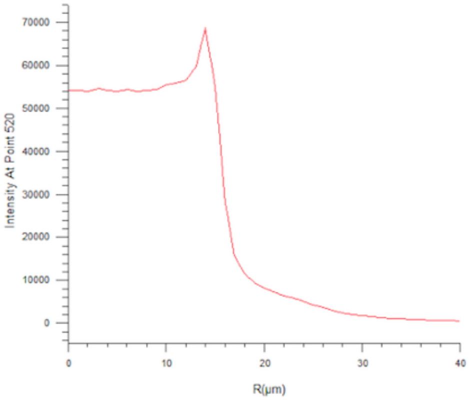

Figure 3.15: Phase diagram of SiGe

3.4 Data Analysis

A MATLAB script was written to aid with analysis of cross-sectional micrographs of the samples. This was done to have an objective measure of whether samples are homogeneous or not, giving an easy way to compare the large amount of data retrieved in the thesis. Section 3.4.1 will explain the script. For µ-Raman, several spectra were peak-fitted. Section 3.4.2 will discuss peak fitting.

3.4.1 Compositional Analysis

The MATLAB analysis is done to have a way of quickly determine what sample that are possibly homogeneous in a large dataset. BSE EDS micrographs of core cross-sections were analysed using the MATLAB script *Analysis.m*, provided in appendix A. Prior to analysis, the BSE micrographs were cropped and blurred using ImageJ, in order to reduce pixelated noise for the edge detection.

Analysis.m loads the image and converts it into a matrix with elements corresponding to the pixel grey values. Each row of the image matrix is then derivated. From the derivated matrix the edge of the core can be found by determining the maxima of the derivatives, as the contrast between core and cladding is much greater than internal variances. The maxima are determine per row, but splitting the columns into two parts as there are two maxima (each side of the core). The centre of the detected edge is assigned by averaging all detected edge positions per row and column, thus giving the mean x and y position of the edge and defining it as the centre. A matrix of the same size as the image is then created containing the distance to all points. Figure 3.16a present an input image image of an untreated fibre and the figure 3.16b present the detected edge and centre. By using the determined edge indices the radius can be calculated by averaging the distance from the centre to all edge points.

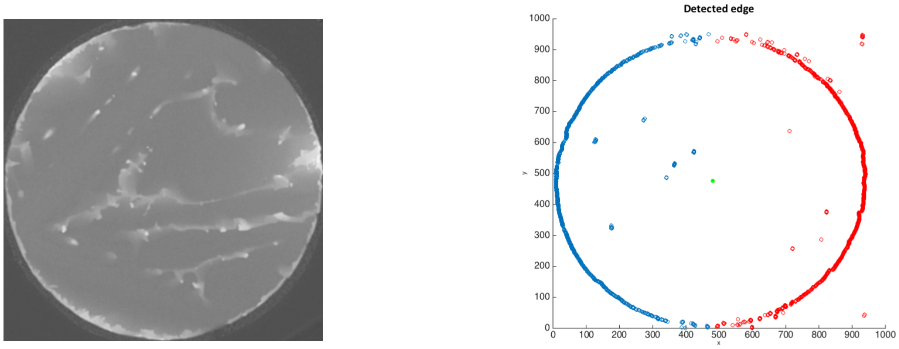

(a)

(b)

Figure 3.16: Cropped and blurred image of untreated fibre input into *Anaylysis.m* (a) and the detected edge and centre (b). The red and blue circles mark the edge at the different sides whereas the green marks the centre. A few misplaced indices are expected for the inhomogeneous samples.

In order to give a description of compositional variance in the samples the average grey scale value of the core is calculated to use as a reference. The average value is determined by creating a matrix from the distances matrix containing the grey scale value within the specified radius and zeros outside. The average is then computed by summing over the hwole matrix and dividing by the amount of non-zero integers in the matrix. The radial change in composition is then determined by integrating the grey scale value of a hollow circle of radius r and thickness $2dr$ normalised with respect to the same integrated area using the average greyscale value. This is calculated by using the distances matrix to define a logic matrix where all elements outside the defined radius $r \pm dr$ are zeros. The grey scale value is then the sum of all non-zero elements, and the result is divided by the average grey scalevalue. By repeating the procedure for all r from the centre to the edge the distribution is determined. The resulting values are plotted against radius, as illustrated in figure 3.18a. The angular distribution is also of interest and is presented by a similiar plot (figure 3.18b) as the radial distribution. The conic shape defined by an angle $\theta \pm \phi/2$, where $\theta \in [0, 2\pi)$ inside the core is integrated and compared to the same area with the average greyscale value. The results is then plotted against angle.

Based on the calculated integral areas, the sum of least squares was calculated using equation 3.8 to allow for easy determination of successful treatments.

$$S = \sum_{r=0}^{Radius} (r_i - 1)^2 \tag{3.8}$$

3.4.1.1 Examples

Three cases will be presented in the following section to illustrate how the analysis works. The cases investigated are an inhomogeneous, untreated fibre; an inhomogeneous, treated sample; and a homogeneous treated sample. The three samples analysed are presented in figure 3.17. Figures 3.18a and 3.18b show the result from analysing a cross-sectional micrograph of the samples with Analysis.m. In addition, table 3.7 presents the sum of least squares calculated for all three samples. The difference in sum of least squares for the homogeneous relative to the inhomogeneous is vast, allowing for easy differentiation. However, it is not trivial to separate between figures 3.17a and 3.17b based on the calculated sum of least squares, but they do represent to very different cases that are important to distinguish between. By considering the radial and angular distributions for the two samples, it is possible to distinguish. Considering the blue line in figure 3.18a, it suggests that the Ge is concentrated to the edge of the fibre core. Figure 3.18b clearly shows that the Ge is located on one side of the core aswell. Combining the two graphs indicates a fibre with Ge concentrated at the edge of one side, as is clearly the case in figure 3.17b.

Table 3.7: Calculated sum of least squares for the angular and radial distributions of the samples in figure 3.17.

	Sum of Least Squares	
	Radial	Angular
Untreated	0.066131	0.1555
Inhomogeneous	0.011922	0.021215
Homogeneous	8.2931e-05	0.00058566

The sum of least squares together with the radial and angular distribution plots give a quite good understanding of the sample. There are, however, some major drawbacks with the script. For some of the samples analysed, the angular distribution shows a distinct sinusoidal dependency. As the script only analyses the greyscale value, it can not distinguish between compositional variations or shadowing effects. Some samples have been slightly tilted in the SEM, thus giving a slightly higher signal from one side than the other. This will show up as a sinusoidal wave, but is easily recognisable, and the radial distribution will tell if the sample is homogeneous or not. All in all, the script is meant as a screening mechanism to determine which samples that are likely to have a homogeneous composition, and is implemented as a way of analysing the large amount of micrographs obtained in this work.

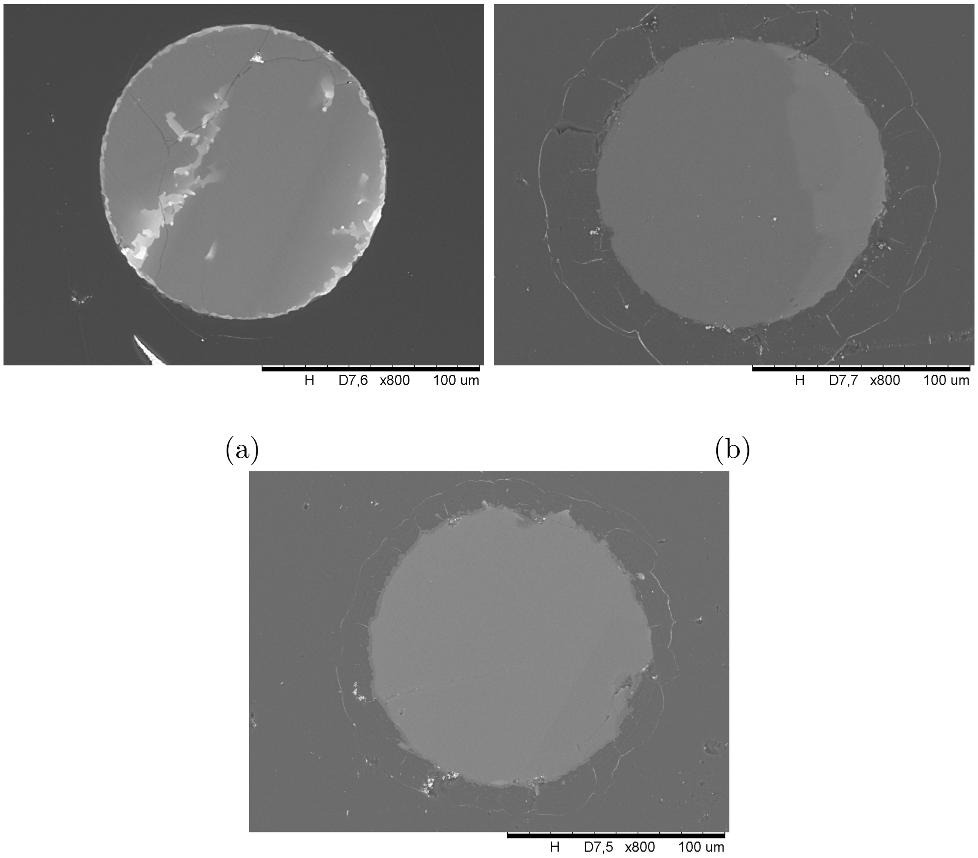
H D7,6 x800 100 um
H D7,7 x800 100 um
H D7,5 x800 100 um

(a) (b)

(c)

Figure 3.17: BSE SEM micrographs of an untreated sample (a), an inhomogeneous treated sample (b) and a homogeneous treated sample (c).

3.4.2 Peak Fitting

Peak fitting of Raman spectra was performed using FITYK v.0.9.8. A Voigt peak profile was used and the Levenberg-Marquardt fit method. Prior to peak fitting, a careful baseline subtraction was performed, using [68] as a template.

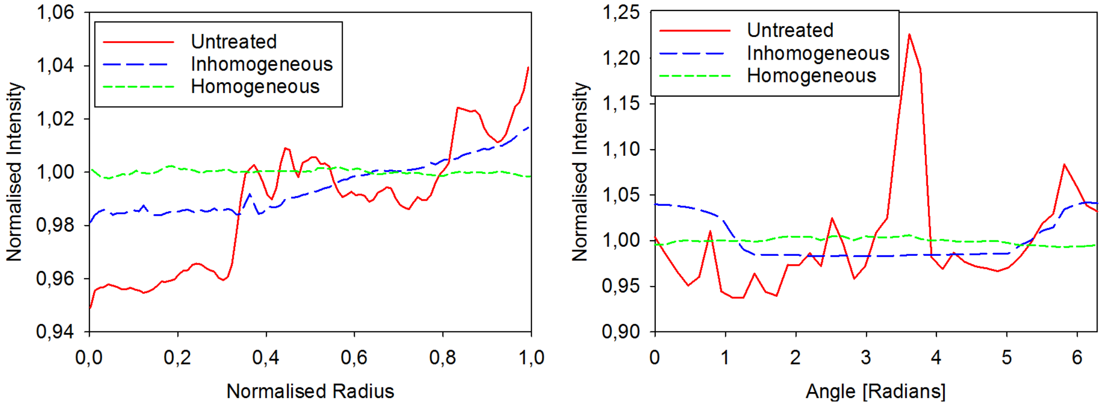

(a) (b)

Figure 3.18: Radial (a) and angular (b) distribution for the three examples presented in figure 3.17.

Chapter 4

Results and Discussion

The results will be resented in two main parts. Section 4.1 and section 4.2 will present SEM and EDS results for all heat treated samples. Section 4.1.1 will present the resulting compositional distribution from the tube furnace annealed samples. The results will be compared to literature to establish a baseline. The critical growth velocity for homogeneous samples using recrystallisation by zone melting will be determined experimentally from the SEM results in section 4.1.2. A theoretical estimate will be calculated by Tiller's criterion in section 4.1.3. Section 4.1.4 will investigate deviations in experimentally determined critical growth velocities in the different samples, as well as discrepancies between theoretically and experimentally determined values. Section 4.2 will present EDS data and analyse if the treatments change the composition, especially with respect to oxygen levels.

The second part of the results will present EBSD and µ-Raman results for three selected samples: CAO2B, CAL100-1 and an untreated sample. Section 4.3 will present data on the crystallinity of the selected samples to investigate the effect of the recrystallisation techniques on the microstructure of the sample. Then, section 4.4 will present µ-Raman spectroscopic data and discuss how the treatments affect strain in the fibres.

4.1 Compositional Distribution

The following section will present the results obtained with the different annealing procedures. All samples have been characterised by SEM and EDS by investigating cross-sections of the fibres. Most samples have been analysed using *Analysis.m*, however, for samples where the analysis proved not achievable, micrographs will be presented and discussed in stead.

In chapter 3 it was stated that the fibres appear to be inhomogeneous based on the cross-sectional micrographs. The statement was further investigated by XRT. Figure 4.1 presents an XRT slice of an untreated CA fibre, clearly showing an inhomogeneous composition with respect to Ge.

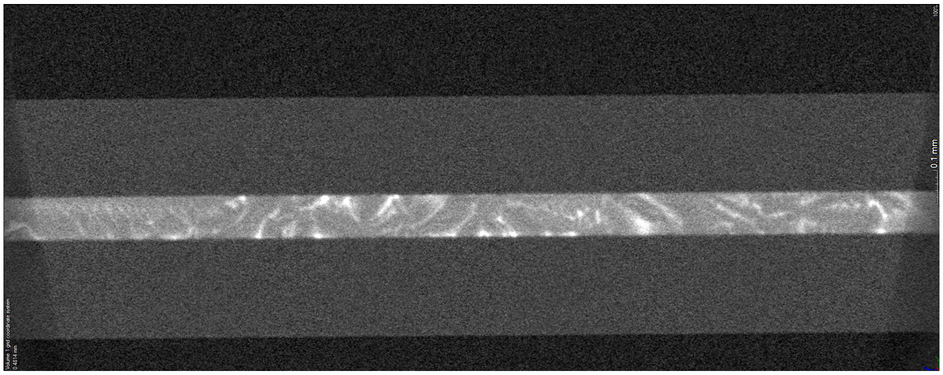

Figure 4.1: XRT slice of an untreated CA fibre. The SiO_2 cladding is clearly visible sorrounding the inhomogeneous SiGe core. The light areas are Ge-rich and variations of up to 20at% are shown in section 3.1.2 and as high as 36at% are shown in section4.4.1.

An NA fibre with approximately $20at\%$ Ge content is presented in figure 4.2 [1]. A crystal structure resembling dendritic growth is clearly visible from the figure. The difference in solidification structure is both due to the difference in composition, as well as the different cooling rates in the two drawing mechanisms.

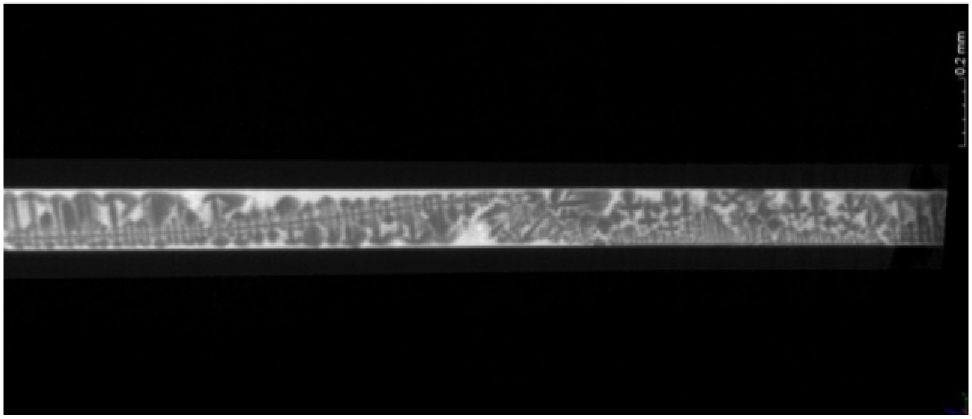

Figure 4.2: XRT slice of an untreated SiGe fibre with 20at% Ge. The inhomogeneous core has a crystal structure resembling dendritic growth.

---

[1] Sample from previous work

4.1.1 Tube-Furnace

Two different programs were tested, as described in section 3.2.1. For tube-furnace treated samples cross-sectional SEM micrographs from the centre of each sample was analysed using *Analysis.m* and the results will be presented in the following sections. Slow cooling using similar cooling rates as those investigated in this work has resulted in polycrystalline SiGe [69], however, this work will look at whether the dimensions of the fibres can have a positive effect or not. A comparison between the fast and slow cooling rate will be made. Additionally, several different positions in the oven were tested and the effects of placement will be discussed. The centre of the fibres was investigated to ensure steady state conditions. Some corresponding figures are included, and a collection of all figures can be found in Appendix B.

4.1.1.1 Program A - Slow Cooling

Two annealing runs were performed using program A, with a cooling rate of 1.5 °C min^{-1}. The CAO1 and CAO2 batches were treated with program A, with the samples placed as shown in figure 3.7. The radial and angular distributions for CAO1 and CAO2 are presented in figures 4.3 and 4.4, respectively. Samples CAO2R and CAO2RC show only minute changes in composition respect to radius and small changes with respect to angle. All CAO1 samples have an increasing Ge-content towards the edge of the core, distributed at random angles.

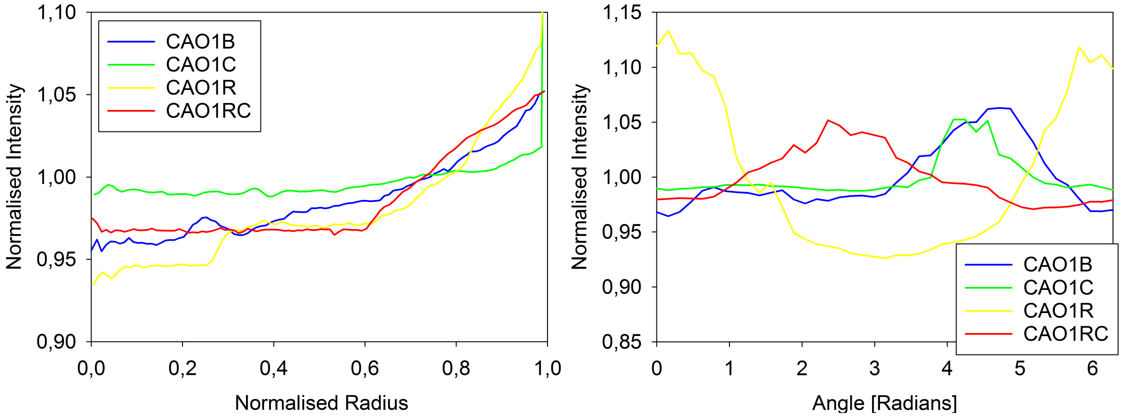

(a) (b)

Figure 4.3: Radial (a) and angular (b) distribution of Ge in batch CAO1. All samples have an incresing Ge content towards the edge of the core restrained to random angles.

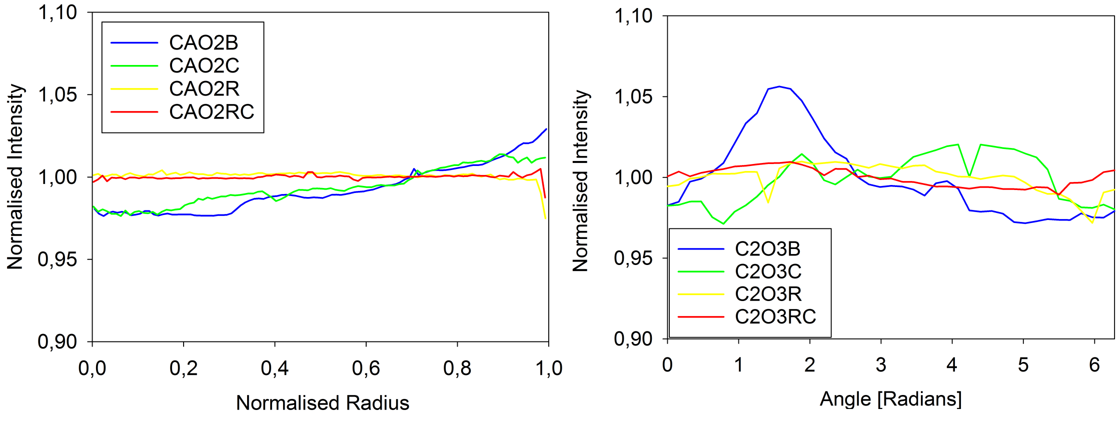

(a) (b)

Figure 4.4: Radial (a) and angular (b) distribution of Ge in batch CAO2. Samples CAO2R and CAO2RC have flat radial and angular distributions.

4.1.1.2 Program B - Fast Cooling

An additional two runs were performed using program B, having a faster cooling rate of 5 °C min^{-1}. Again, the samples were placed as illustrated in figures 3.7 for both runs. The results from cross-section SEM analysis is presented in figures 4.5 and 4.6 for samples CAO3 and CAO4, respectively. Samples CAO3C and CAO4B have a relatively flat distribution of Ge, as seen in figures 4.5 and 4.6. For the remaining samples, the Ge appears to be concentrated at the edges of the core. The angular distribution of the CAO3RC sample has a sinusoidal shape, occurring because of the script weakness described in section 3.4. From the radial distribution of the sample, it is clear that CAO3RC is homogeneous with respect to radius. Consulting figure B.2d confirms that the sample is homogeneous.

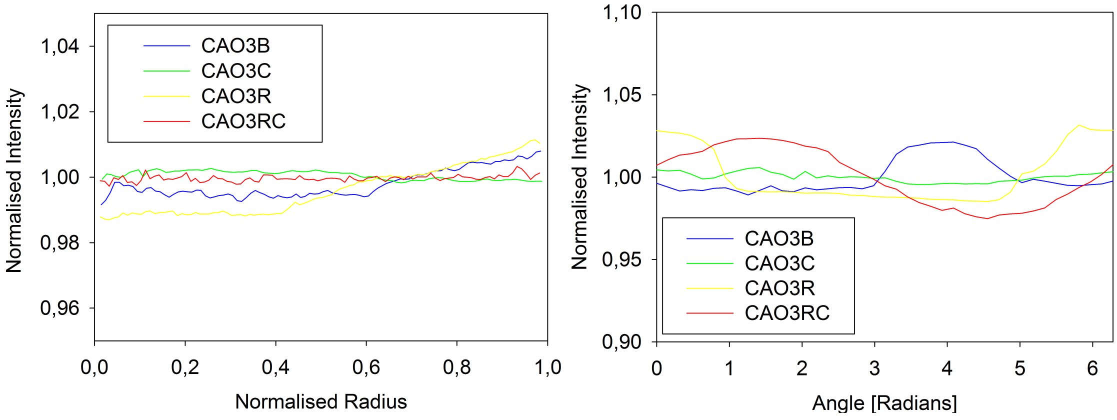

(a) (b)

Figure 4.5: Radial (a) and angular (b) distribution of Ge in batch CAO3. CAO3C and CAO3RC show a flat radial distribution. CAO3C has a sinusoidal angular distribution, though this is due to a weakness in the analysis method.

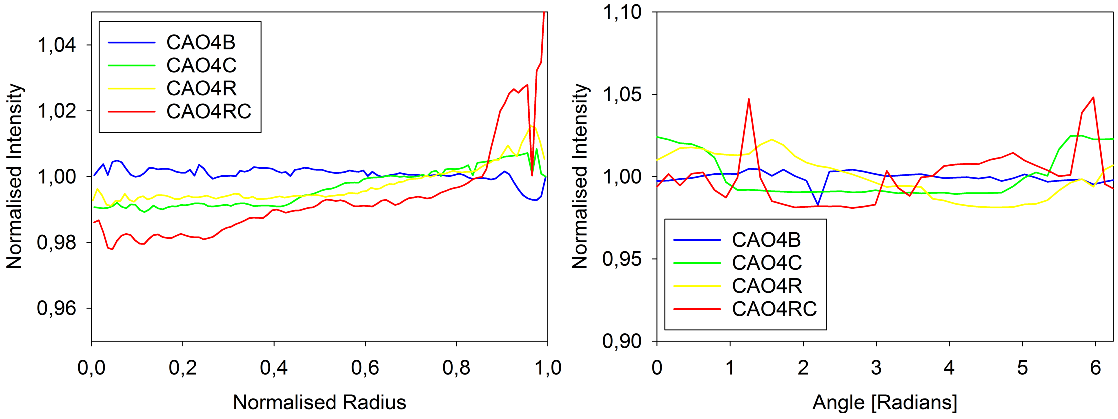

(a) (b)

Figure 4.6: Radial (a) and angular (b) distribution of Ge in batch CAO4.

4.1.1.3 Discusison

The calculated sum of least squares for the radial and angular distribution for all tube-furnace annealed samples are plotted in figures 4.7a and 4.7b, respectively. The dashed line in the figures marks an approximate separation between homogeneous and inhomogeneous composition. This was determined by investigation of the figures in appendix B.

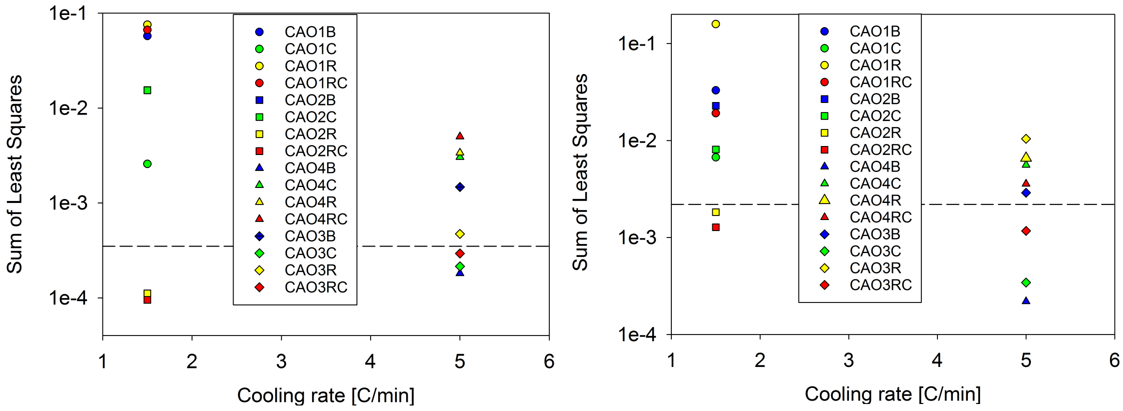

(a) (b)

Figure 4.7: Radial (a) and angular (b) SLS versus cooling rate for all tube-furnace annealed sample. The dashed line marks an approximate separation between homogeneous and inhomogeneous composition.

Based on the results presented in figures 4.7a and 4.7b, there are no apparent trends with respect to resulting compositional distribution versus sample placement in the oven - homogeneous and inhomogeneous results occur for all placements. The SLS for the samples annealed at a slower rate are higher than for those solidified at a higher rate, though the reason for the behaviour is unclear. Some examples of inhomogeneous samples are given in figure 4.8. From the samples presented in figure 4.8, it is clear that for all inhomogeneous samples, there is an increase of Ge as the radius increases. Consulting figures B.1, B.2, B.3 and B.6 confirms this. However, it is very important to note that the low Ge content area is always in contact with the perimeter of the core. As the initially nucleated grain will be solute-poor, as explained in section 2.1, such a structure could occur by heterogeneous nucleation on the cladding. As the grain grows, the residual melt will see an increase in Ge content, thus leading to Ge-rich areas forming. For several of the samples the Ge is restricted to specific angles. The resulting structure is similar to the polycrystalline SiGe produced by Usami et al. by slow freezing at a rate of 3 °C [69]. It is not clear whether the samples are single crystalline, or polycrystalline as in [69]. The crystallinity will be investigated in section 4.3.2.

The homogeneous fibres were further investigated to determine the extent of the homogeneous region. Figure 4.9 presents two cross-sections of the homogeneous CAO4B sample, separated by approximately 0.4 mm. It appears that the homogeneous section is of substantial size, but further investigations by XRT are needed.

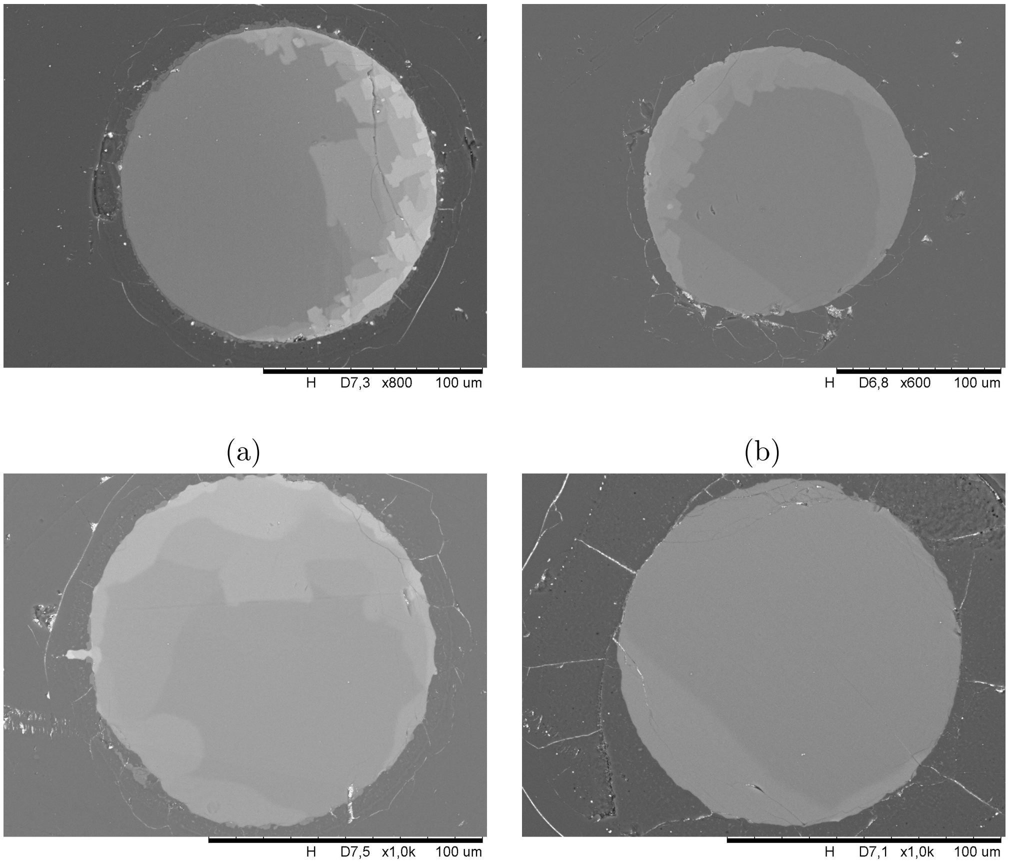

(a) (b)

(c) (d)

Figure 4.8: BSE SEM micrographs of samples CAO1R (a), CAO1RC (b), CAO2B (c) and CAO3B (d). All samples have discrete compositional changes with Ge content increasing towards the edge. For all samples, the low Ge content area is in contact with the core-cladding interface.

For optical waveguide applications it is important to have a well-defined interface to allow for internal reflection [73]. Considering the samples presented in figures 3.17b, 3.17c, 4.8c and 4.8d, it appears that the glass is damaged by the procedure. Several samples show disfigured interfaces relative to untreated fibres, as seen in figures B.1, B.2, B.3 and B.6. Additionally, as the process of slow cooling of the fibres appears to give both homogeneous and inhomogeneous, and with large structural variations for the inhomogeneous samples, the annealing procedure is disregarded for production of optical grade fibres. It might, however, be very interesting in the field of microwire solar cells [74] due to the compositional variations

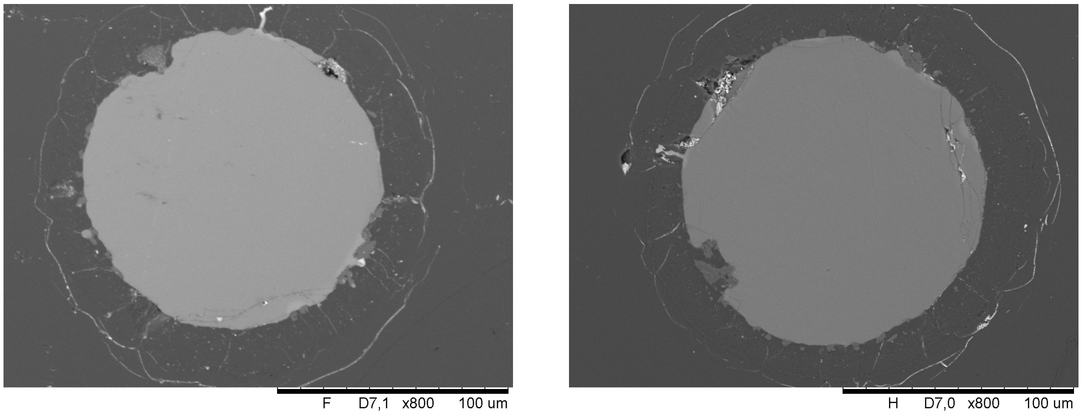

(a) (b)

Figure 4.9: BSE SEM micrographs from the sample CAO4B, separated by approximately 400 µm. The sample appears to be homogeneous for a substantial length.

[69]. Polycrystalline SiGe of varying composition will experience internal scattering and higher absorption. THe compositional nonuniformity will allow for near-infrared absoprtion in polycrystalline SiGe, where polycrystalline Si is transparent [69].

4.1.2 CO_2-Laser

Travelling melt zone recrystallisation by use of a CO_2 laser was performed to produce homogeneous fibres. The aim was to determine the critical growth velocity for homogeneous growth experimentally for each of the sample batches CA, NA, CR and NR. The theoretical value for the CA samples is calculated by Tiller's criterion in section 4.1.3. Section 4.1.4 will discuss the different critical growth velocities for the different systems, as well as compare the results with the theoretically expected value. All CA and NR fibres treated with the CO_2-laser were investigated by cross-sectional SEM, using the Matlab script *Analysis.m*. The CR samples were to small to get satisfying end-face polish, and the CA too brittle, and will therefore be discussed using micrographs. The results will be presented separately for each batch. XRT was used to investigate homogeneity throughout the samples.

4.1.2.1 CAL

The most thorough investigation of recrystallisation by zone melting was performed on the CAL samples. A total of 8 samples were treated, as shown in table 3.5, repeating several velocities. Figure 4.12 presents the SLS for the radial and angular distribution of all the CAL samples. Figures 4.10 and 4.11 show the radial and angular distribution of Ge.

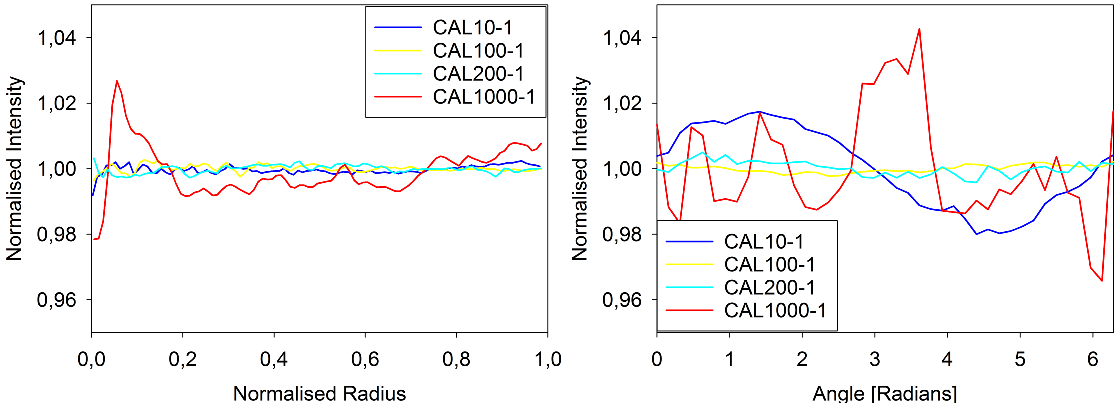

(a) (b)

Figure 4.10: Radial (a) and angular (b) distribution of Ge for samples CAL10-1, CAL100-1 and CAL1000-1. The distributions are flat up until 1000 µm s^{-1}, except for the angular distribution of CAL10-1, which has a sinusoidal shape due to a shortcoming of the analysis method.

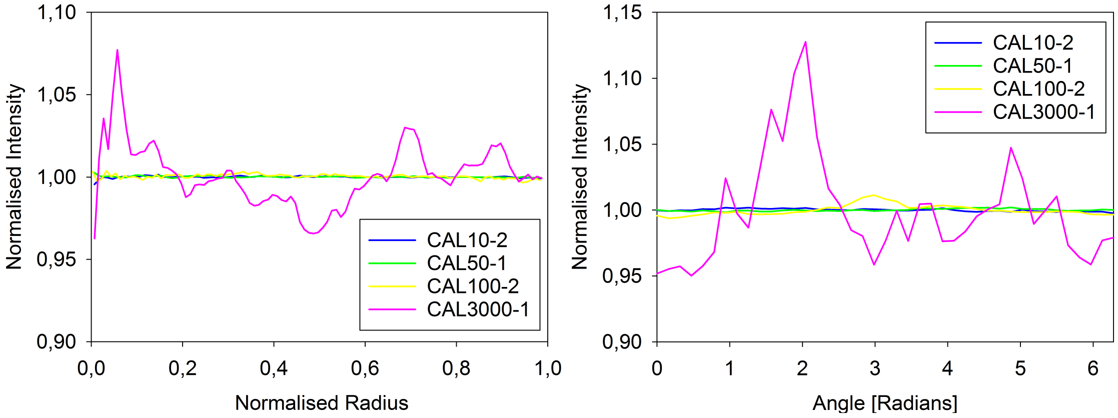

(a) (b)

Figure 4.11: Radial (a) and angular (b) distribution of Ge for samples CAL10-2, CAL50-1, CAL100-2 and CAL3000. All samples are homogeneous, except for CAL3000-1.

There is a definite change between 200 µm s^{-1} and 1000 µm s^{-1}. The samples CAL200-1 and CAL1000-1 are presented in figure 4.13, and it is clear that the sample CAL200-1 has

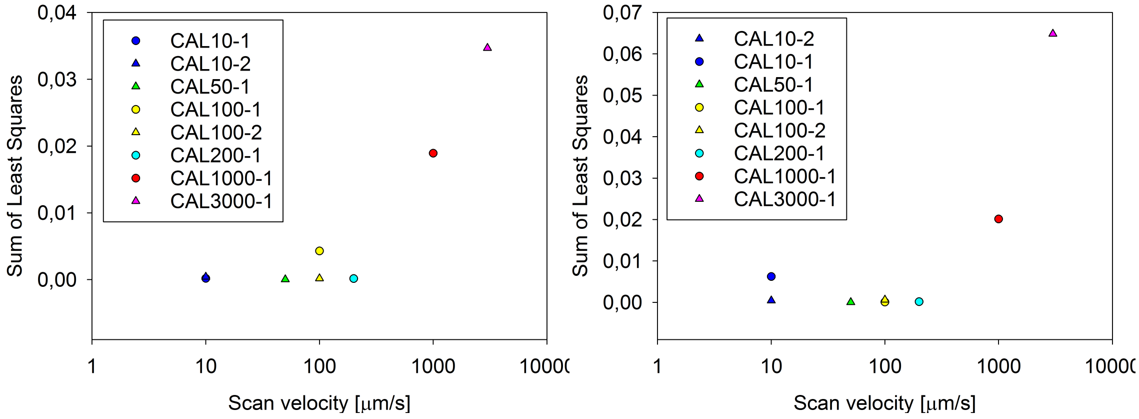

(a) (b)

Figure 4.12: Radial (a) and angular (b) SLS for the CAL samples. There is a distinct increase in SLS going from 200 µm s^{-1} to 1000 µm s^{-1}.

a homogeneous composition, whereas CAL1000-1 does not. This indicates that the critical growth velocity for homogeneous, planar growth is between 200 µm s^{-1} and 1000 µm s^{-1}. The sample CAL10-1 has a notably higher SLS for the angular composition compared to the other samples of similar velocities, and this is because of a flaw in the MATLAB program discussed in section 3.4.

The experiments using scan velocities of 10 µm s^{-1}, 100 µm s^{-1} and 1000 µm s^{-1} were repeated at two different occasions. 10 µm s^{-1} and 100 µm s^{-1} yielded homogeneous samples both times, whereas 1000 µm s^{-1} resulted in an inhomogeneous distribution both times.

XRT was used to investigate if the apparent homogeneous composition of the samples was representative for the whole fibre. Figure 4.14 shows a representative XRT slice of the CAL100-1 sample on top of an untreated standard. Based on figure 4.14 it is concluded that the samples are of homogeneous composition throughout the treated region.

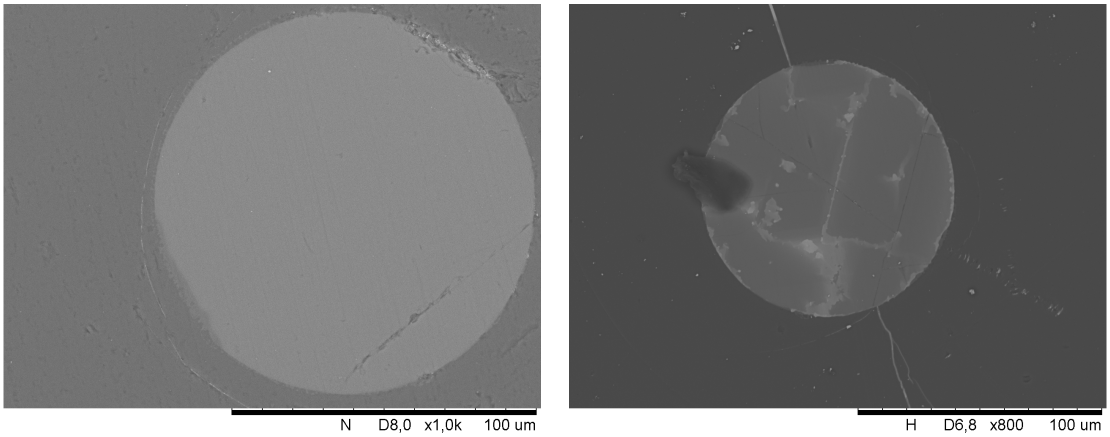

(a) (b)

Figure 4.13: BSE SEM micrograph of the samples CAL200-1 and CAL1000-1. CAL200-1 has a homogeneous composition, but has some darker damaged areas, whereas CAL1000-1 is clearly inhomogeneous.

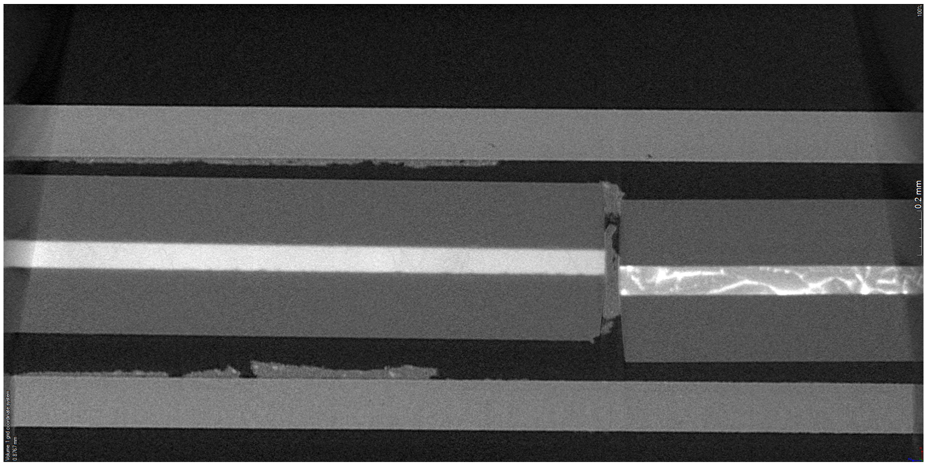

Figure 4.14: XRT slice of the sample CRL2, placed on top of the untreated standard. The untreated standard has an inhomogeneous composition, whereas the treated sample has a homogeneous composition throughout the treated region.

4.1.2.2 CRL

Three CR fibres were treated using the velocities stated in table 3.5. As the redrawn samples have a core diameter of approximately 8 µm, polishing it well enough for MATLAB analysis was very difficult. Figure 4.15 present LA-BSE images of cross-sections for an untreated (a) and all treated samples. It appears that the samples are homogeneous for all scan velocities. Thestructures observed across the glass and core are due to craks and thus surface effects rather than compositional changes. This is confirmed by the continous change across the fibre/cladding interface and investigation by SE SEM.

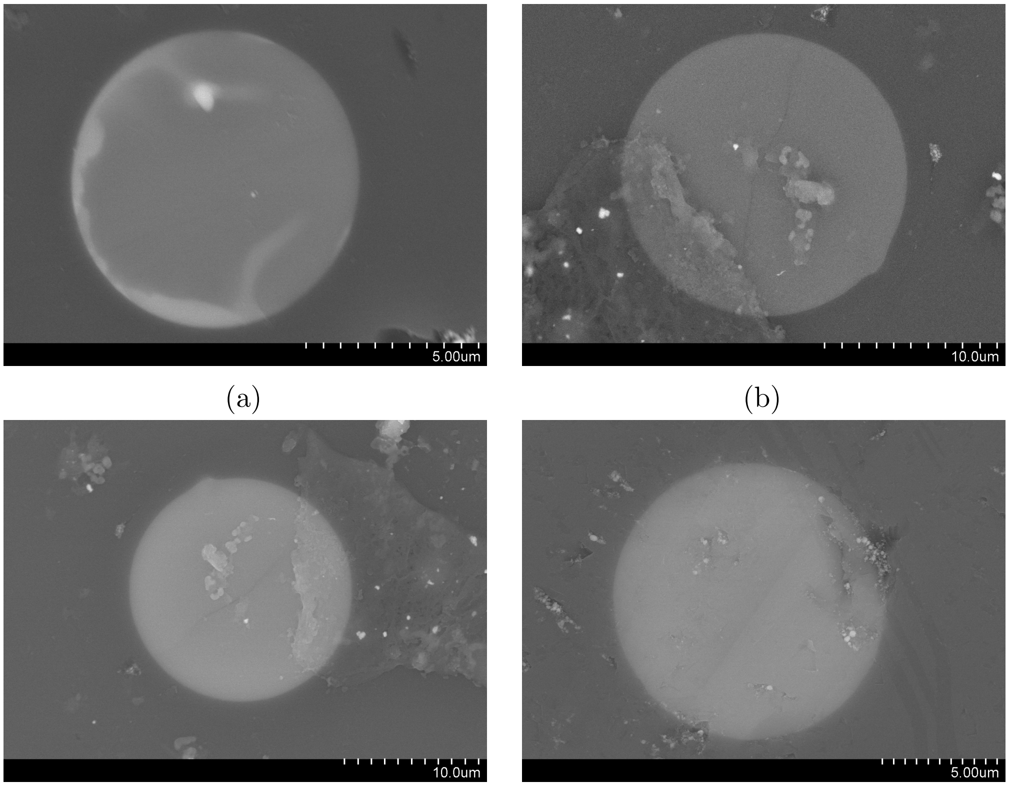

(a) (b)

(c) (d)

Figure 4.15: LA-BSE SEM micrographs of an untreated CR sample (a), CRL10 (b), CRL100 (c) and CRL1000 (d). The contrast in the cores is due to topological contrast.

4.1.2.3 NAL

The NA samples, which had a higher Ge-content, were very hard to polish due to being extremely brittle. As the samples were hand-drawn they have very little glass supporting the brittle core, causing them to break during polishing. Analysis by MATLAB requires flat samples for the edge detection to work, and will be distorted by fractures. Analysis of the NAL samples was therefore done by inspection of micrographs. Figure 4.16b shows the treated samples. Comparing to the untreated NA sample presented in figure 3.2, it appears that only the sample scanned at $10\,\mu\mathrm{m\,s^{-1}}$ is homogeneous in composition. It is worth noting that the sample scanned at $100\,\mu\mathrm{m\,s^{-1}}$ is inhomogeneous, indicating a critical growth rate between $10\,\mu\mathrm{m\,s^{-1}}$ and $100\,\mu\mathrm{m\,s^{-1}}$.

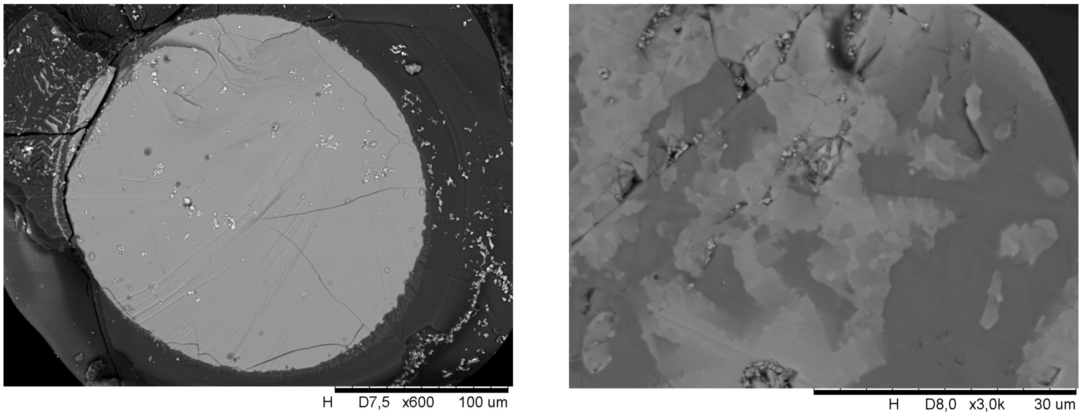

(a) (b)

Figure 4.16: Cross-sectional BSE image of NAL10 (a) and NAL100(B). The side is fractures, but the composition is homogeneous across the face for NAL10-1, whereas inhomogeneous for NAL100-2. Note the difference in magnification in the two images.

Figure 4.17 presents an image from the *B&W*-camera captured during recrystallization of the NAL10 sample. There appear to be changing perturbations on the growth interface suggesting that the interface is on the verge of instability.

4.1.2.4 NRL

Several NRL samples were treated. As they were redrawn into SiO_2 capillaries, they contain much more glass (See figure 3.3) and were thus easier to work with compared to NAL. The resulting fibres were analysed using Analysis.m. Figures 4.18a and 4.18b present the radial and angular distributions, and figure 4.19 presents the calculated SLS for the samples. Again, there is a huge increase in SLS going from $100\,\mu\mathrm{m\,s^{-1}}$ and $1000\,\mu\mathrm{m\,s^{-1}}$. Figures

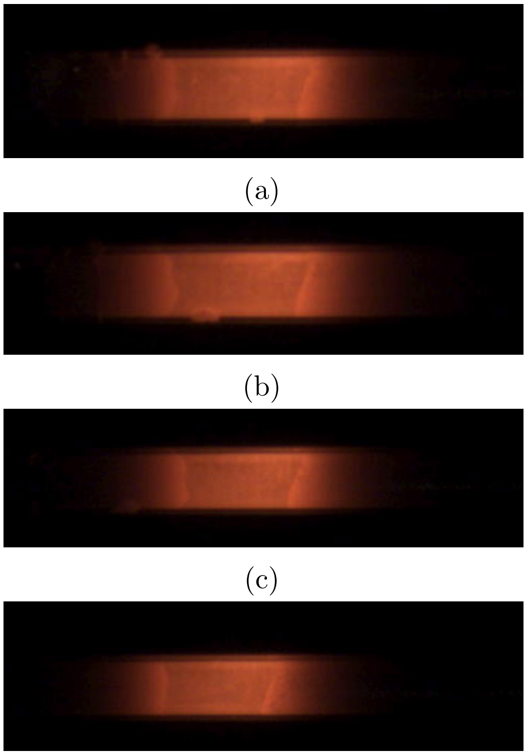

(a)

(b)

(c)

(d)

Figure 4.17: Images captured during laser annealing of the sample NAL10, with approximately 3 s between each. The interface, especially to the left, appears to be on the verge of instability.

4.20a and 4.20b show that NRL100, scanned at 100 µm s^{-1}, has a homogeneous composition, whereas NR1000, scanned at 1000 µm s^{-1}, is inhomogeneous. This suggests a critical growth rate in the given interval.

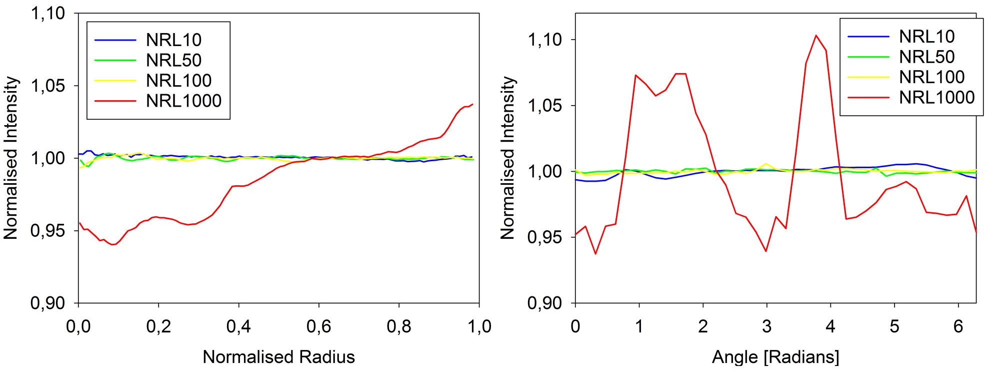

(a) (b)

Figure 4.18: Radial (a) and angular (b) distribution of the NRL samples. The distribution of NRL10, NRL50 and NRL100 are all relatively flat, suggesting a homogeneous composition.

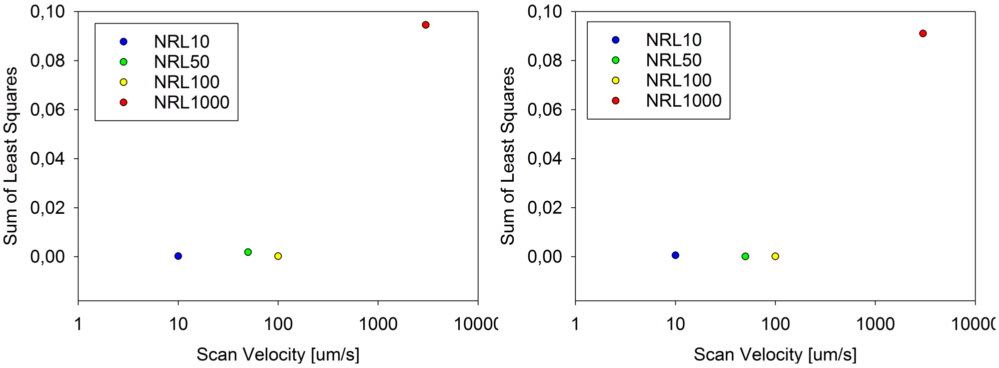

(a) (b)

Figure 4.19: SLS for the radial (a) and angular (b) distribution of Ge in batch NRL. A clear increase in SLS is observed between 100 µm s^{-1} and 1000 µm s^{-1}.

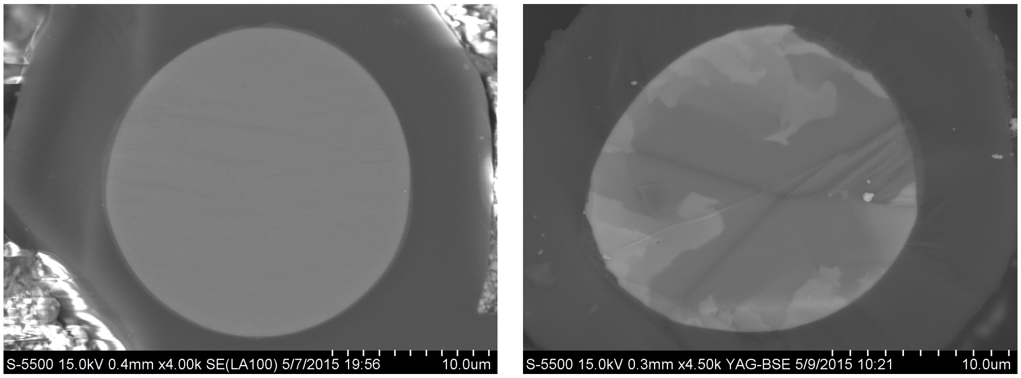
S-5500 15.0kV 0.4mm x4.00k SE(LA100) 5/7/2015 19:56 10.0um
S-5500 15.0kV 0.3mm x4.50k YAG-BSE 5/9/2015 10:21 10.0um

(a) (b)

Figure 4.20: LA-BSE SEM micrographs of the samples NRL100 (a) and NRL1000 (b). As expected from the distribution plots and the SLS, NRL100 has a homogeneous composition, whereas NRL1000 does not.

4.1.3 Calculated Critical Velocity

In section 2.1.3.4, Tiller's criterion was presented as a theoretical criterion to estimate the critical growth velocity of a binary alloy such as SiGe. In this section, the critical growth velocity of the CA samples will be calculated using equation 2.13. The calculated critical velocity will allow for comparison between the experimentally determined critical growth velocities to the theoretical value. As part of the calculation, the thermal gradient in the liquid will be estimated and can thus be compared to other techniques.

4.1.3.1 Clemson Cane

The critical growth velocity of the fibres was calculated for the CA fibres using equation 2.13. The following measurements and calculations are performed for the sample CAL100-2. In order to apply Tiller's equation, five parameters are needed: The diffusion coefficient, D; the segregation coefficient, k; the composition, x; the thermal gradient in the liquid, ∇T_L; and the slope of the liquidus, $\nabla\Theta$. An estimate of the temperature gradient in the melt can be calculated using the films captured with the different filters. Image 4.21 shows the fibre, with the melt zone, captured using the 514 nm filter. Determining the thermal gradient first requires determination of the composition in the melt zone. The diameter of the core is 105 µm, as determined by a cross-sectional SEM micrograph, shown in figure 4.22a. EDS analysis was performed on the core, giving a Ge content of $6.01at\%$. The EDS analysis was performed inside the yellow circle in figure 4.22a, and the spectrum is presented in figure 4.22b. Upon creation of a melt zone, blobs of Ge were recruited to the zone from the solid fibre. The distance from where the Ge seemed to be recruited will be termed the recruitment distance. This is both a consequence of the zone melting technique, but the effect is further strengthened by the inhomogeneous composition of untreated fibre. The high-Ge content areas will have a lowered melting point and can thus melt in the untreated fibre and migrate into the melt zone. By assuming that the recruitment distance is approximately 1 diameter length and the melt zone length is 4.1 diameters, and that all Ge is recruited, the melt zone composition becomes $8.8at\%$. The recruitment distance was determined from films captured while scanning.

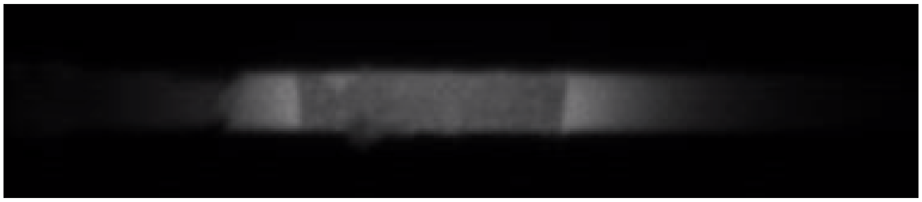

Figure 4.21: Image showing melt zone in the CAL100-2 sample, induced by zone melting with a CO_2 laser. The melt zone length is approximately 4.1 times the fibre diameter.

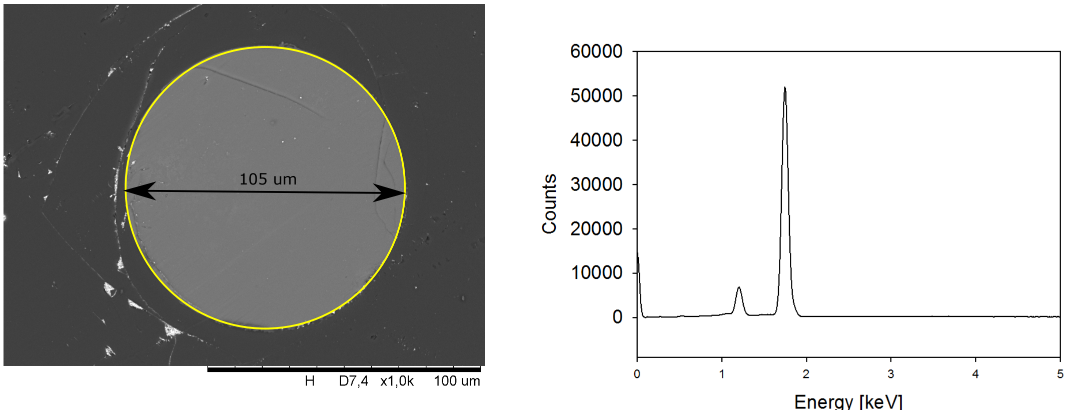

(a) (b)

Figure 4.22: Cross-section of CAL100-2 with EDS quantification area marked by yellow circle (a) and the corresponding EDS spectrum (b).

A profile plot of the greyscale values along the translation direction was done, marked by red in figure 4.23a, and the resulting plot is presented in figure 4.23b. The 514 nm filter was used and is assumed to be ideal. Assuming a constant emissivity of 0.68 for solid SiGe, which is not too crude an assumption for low Ge-content fibres at elevated temperatures [75], the temperature profile can be determined. The two peaks on each side of the melt zone corresponds to the interface, and the difference in signal is due to the difference in emissivity of the solid and molten SiGe. The temperature of melting at a composition of $8.8at\%$ is calculated using equation 4.2 for the liquidus line, giving a temperature of1402 °C. The MATLAB script BlackBody.m was used to determine the blackbody radiation from SiGe at 514 nm at 1402 °C under the stated assumptions. At the melting point, the radiation intensity at 514 nm is 3.358×10^9 W/m^2. Dividing the maximum greyscale intensity in the melt over the minimum at the interface gives $\frac{86.92}{66.97} = 1.30$. The radiation at the maximum temperature is determined by multiplying the radiation at the interface with the ratio between the greyscale intensity. By using BlackBody.m again, the value corresponds to a temperature of 1710°C. The temperature gradient from the interface to the highest temperature is then:

$$\nabla\Theta = 1.43 * 10^4 \mathrm{K/cm}$$

The thermal gradient in the liquid was also investigated using the film filtered by a 635 nm filter. Figure 4.24 shows an image with the 635 nm filter and the profile plot of the greyscale. The intensity ratio between the left interface interface and the middle of the melt zone is calculated from to be 1.24. Using the same procedure as above, the thermal gradient is calculated:

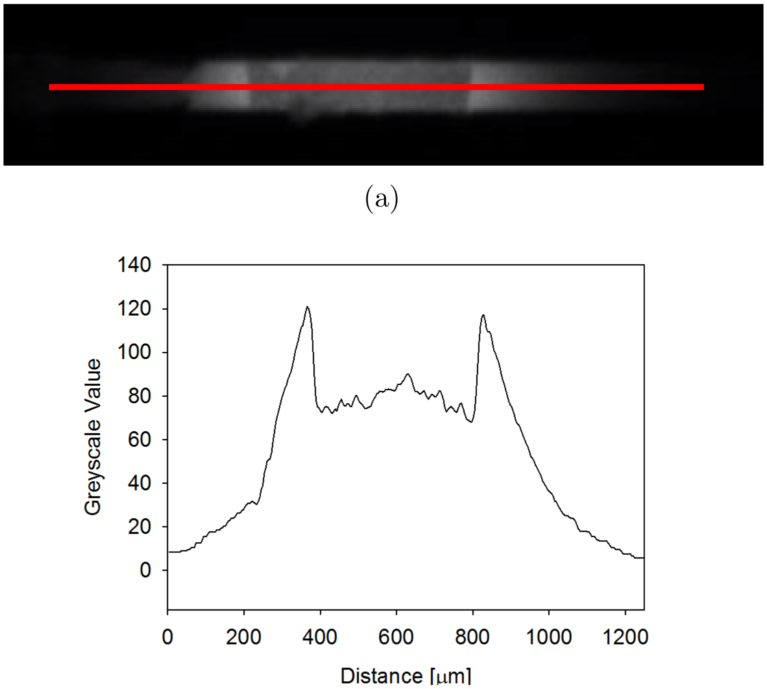

(a)

(b)

Figure 4.23: 514 nm-Filtered image of the melt zone in the fibre (a) and greyscale intensity plot (b) along the red line in image (a). The abrupt changes at the solid/liquid interface is due to the difference in emissivity of the solid and liquid phase.

$$\nabla\Theta = 1.52 * 10^4 \mathrm{K/cm}$$

The error is quite large, as the method is crude. Some sources of error is that the filters are assumed to be perfect, but in reality a distribution passes through. Additionally, the camera detector has a sensitivity function with respect to wavelength which is ignored. The resulting gradient is deemed in agreement with the previously determine gradient. The signal does have more noise using the 635 nm filter, so the gradient calculated from the 514 nm filter will be used for further calculations.

The results calculated with the 635 nm filter is compared to the unfiltered signal in figure 4.25. Though the profile is similar, it is clear that determination of the thermal gradient from the unfiltered film would overestimate the gradient in the melt.

The diffusion coefficient of SiGe can be approximated using an interpolation given in equation 4.1: [8].

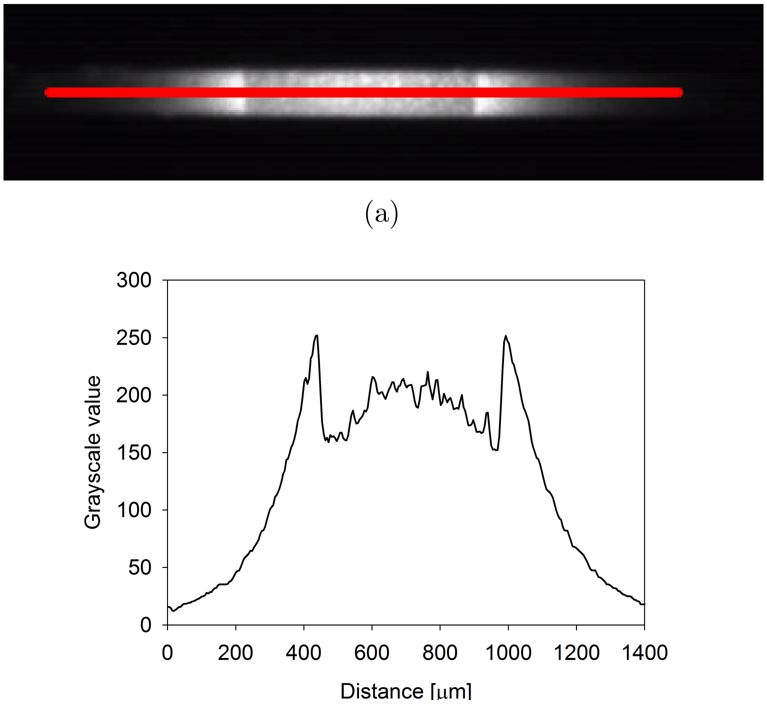

(a)

(b)

Figure 4.24: 635 nm-Filtered image of the melt zone in the fibre (a) and greyscale intensity plot (b) along the red line in image (a).

$$D = (30 - 24(1 - x)) * 10^{-5}\text{cm}^2\text{s}^{-1} \tag{4.1}$$

Where x is the atomic percentage of Ge. A composition of 8.8at% Ge will give a diffusion coefficient of:

$$(30 - 24 * (0.088)) * 10^{-5} cm^2 s^{-1} = 27.89 * 10^{-5} cm^2 s^{-1}$$

Determining the slope of the liquidus, as well as the distribution coefficient requires knowledge of the liquidus and the solidus of the phase diagram of SiGe. A curve fit of the experimental results presented by Stöhr and Klemm in 1939 [11] gives the two equations 4.2 and 4.3.

$$T_L = (1412 - 80x - 395x^2)^\circ C \tag{4.2}$$

$$T_S = (1412 - 738x + 263x^2)^\circ C \tag{4.3}$$

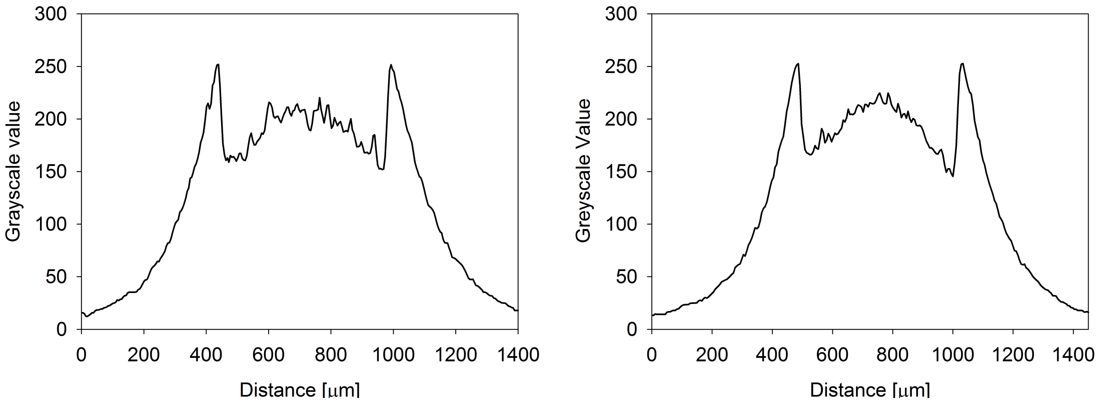

(a) (b)

Figure 4.25: Comparison of the greyscale profile of the melt zone using a 635 nm filter (a) and the unfiltered melt zone (b). The intensity variation in the melt zone is slightly higher than that for the 635 nm filtered image.

where x is the atomic fraction of Ge. The gradient of the liquidus is then given as the derivative of equation 4.2, giving:

$$\nabla T_L = -790x - 80 \tag{4.4}$$

Inserting the known composition into equation 4.4, the slope is calculated to be −149.5. Calculating the distribution coefficient is not trivial, as it will vary throughout both the liquid and the solid, further complicated by the recruitment zone. From the definition of the distribution coefficient in equation 2.10, and by using the equations for the liquidus and solidus in equations 4.2 and 4.3, the composition of the liquid and solid at the interface can be calculated. For a temperature of $1402°C$, the distribution coefficient is:

$$k = 0.16$$

The values for C_S and C_L where derived by solving equation 4.2 and 4.3. The critical velocity was then calculated using the values derived:

$$v_c = 348.23\mu\text{ms}^{-1}$$

The theoretical maximum growth velocity for an atomic component of 91.2at% Si fibres calculated by Tiller's criterion is 348.23 µm s^{-1}, meaning that any scan velocity exceeding it ought to give inhomogeneous samples.

4.1.3.2 NAL

No filtered images are available to the NA samples, however the *B&W* images can allow for an estimate of the thermal gradient. Figure 4.26a presents an image of the fibre and melt zone, and figure 4.26b gives the greyscale intensity profile.

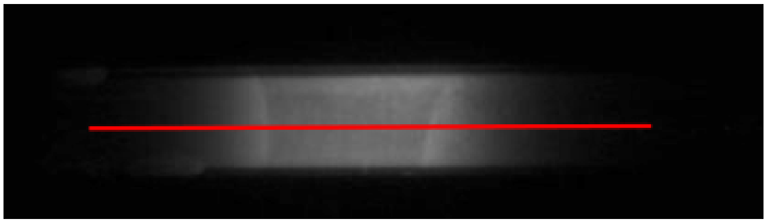

(a)

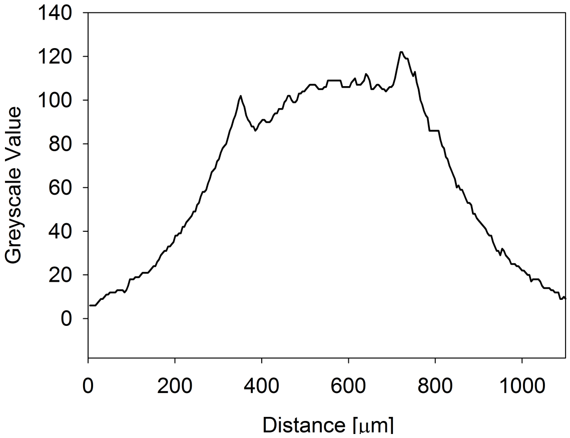

(b)

Figure 4.26: Unfiltered image of the melt zone in fibre NAL10 (a) and the greyscale intensity plot (b) along the red line in image (a).

The profile is slanted, making it very hard to determine the thermal gradient. In appendix C there is a baseline corrected profile, revealing a much lower intensity variation than those seen in figure 4.25b. This indicates a much lower thermal gradient in the liquid, which would lead to a reduction in the critical growth rate. As the thermal gradient is most likely overestimated, an upper limit on the critical growth velocity for the NA sample is calculated in appendix C, and the calculated value is:

$$v_c = 29.4\mu\mathrm{ms}^{-1}$$

4.1.3.3 Error in Calculations

Though the Tiller criterion is commonly used today [13], more advanced theories have been derived. Mullins and Sekerka developed a theory on interface stability in 1964 [28] that give growth velocities up to 50% higher than the velocities predicted theory of Tiller *et al.* [8]. This is due to the inclusion of the interfacial energy (capillarity) and thermal gradient in the solid for the Mullins-Sekerka theory [76], as explained in section 2.1.3.4.

There are several sources of error for the calculations of the critical growth velocity. The emissivity of the sample is assumed to be constant for all wavelength, which is an approximation. It is worth noting that the emissivity of pure Si has been used for the calculation, due to the low Ge content, though as the emissivity has been assumed constant this has no practical effects. Additionally, the emissivity is assumed to be constant with respect to temperature both in the solid and the liquid. The calculation of the concentration in the melt zone is a rough estimate, based on observations from the captured films. A difference in the recruitment distance or amount in the area will lead to a change in composition in the liquid, in turn changing the melting point. Further, this will alter the distribution coefficient of the material. Additionally, the composition in the melt zone will not be uniform, due to the thermal gradient altering the solubility. The compositional variations in the liquid will cause further error in the emissivity assumptions.

4.1.4 Discussion

Based on the results presented in section 4.1.2, it is clear that recrystallization using the CO_2 laser results in homogeneous samples, up until certain scan velocities. From section 2.1.3, it is expected that the critical growth velocity decreases as the liquidus slope and distribution coefficient increases. As seen in the phase diagram for SiGe (figure 2.10), both are much higher at intermediate compositions (NA) rather than low Ge compositon (CA). Additionally, from the theory of Mullins and Sekerka, a reduction in dimensions might increase the interface stability due to capillarity and thus increase the critical growth rate. From the previous arguments it is theoretically expected that the critical growth rate is higher in the C samples compared to the N samples, as well as higher rates for the redrawn ones due to a smaller core size. In section 4.1.2 it was shown that all samples investigated worked up until at least $100\,\mu m\,s^{-1}$ scan velocities, except NAL. For CA , the experimentally determined critical growth velocity is somewhere between $200\,\mu m\,s^{-1}$ and $1000\,\mu m\,s^{-1}$ based on the SEM analysis. For the CRL samples, all scan velocities resulted in homogeneous samples.

The observed growth velocities are much higher than what is usually reported for homogeneous growth of SiGe. A simple conversion will show that the tested rates vary between $36\,mm\,h^{-1}$ and $10\,800\,mm\,h^{-1}$, or $10.8\,m\,h^{-1}$. . From the calculated critical velocity in section 4.1.3 the main distinction from most literature is the extreme thermal gradient in the liquid using the CO_2 laser technique. In CZ growth the thermal gradient is often limited to approximately 40 °C cm^{-1}, whereas for this technique the thermal gradient is ≈1.43 × 10^{4} °C cm^{-1}. This can allow for large constitutional supercooling without the interface destabilising. The experimental data for the CAL samples suggest that the critical growth velocity is between 200 µm s^{-1} and 1000 µm s^{-1}. The experimentally determined growth rate is in agreement with the theoretical calculations.

For the CRL fibres, a homogeneous result is achieved for all scan velocities. The samples are to small for the estimation of a thermal gradient from the camera. However, it is probable that the gradient is not too far from that of the as-drawn fibres based on the width of the bright zone in the fibres during recrystallisation. Mullin-Sekerka theory might hold the answer, especially with the inclusion of thermal diffusion. At high thermal gradients, as is definitely the case, thermal diffusion can stabilise the interface [37], thus allowing for higher growth rates. Capillarity in the fibres will also aid in stabilising the growth interface. As the fibres have very small dimensions and the scan rates are very high, it might be that a state of absolute interface stability is reached due to the increased capillarity [28]. This might explain why the CR are homogeneous at 1000 µm s^{-1} and the CA are not. According to Mullins and Sekerka, the wavelength of disturbance that corresponds to a maximum instability is approximately 50 µm [28]. As the redrawn fibre has a diameter of 8 µm, an absolute stability is feasible. Whether there is absolute stability or not for the redrawn fibres is not clear, however, a much higher interface stability is seen for the CR fibres, evident from the homogeneous fibres treated at 1000 µm s^{-1}. Without exact determination of the thermal gradient in the CR fibre it is not possible to state for certain whether the increased stability is due to the smaller dimensions or just a change in thermal gradient. However, as the relative amount of glass is not vastly different between the CA and CR fibres it seems likely that the thermal gradients are quite similar, suggesting that the small dimensions to stabilise.

The higher Ge content of the NTNU drawn fibres will decrease the critical growth velocity, as constitutional supercooling occurs more readily [24]. As there is no data available to accurately estimate the thermal gradient for the NAL samples, the calculation is prone to severe error, as explained in section 4.1.3.2. The experimental data in section 4.1.2.3 suggest a critical growth velocity between 10 µm s^{-1} and 100 µm s^{-1}. Figure 4.17 shows an interface on the verge of instability, with pertubations growing and decaying. This suggests that the critical growth rate is close to 10 µm s^{-1}. Comparing this to the very crude estimate of the critical growth velocity calculated from an unfiltered $B\&W$ image in appendix **??**, it appears that the theoretical critical growth velocity calculated by Tiller's criterion is in agreement with experimentally determined value. The reduction in growth velocity is partly due to the increased Ge content, but also due to the lower thermal gradient. The CA samples have very little glass, which can limit the gradient as only the glass is heated directly.

A big discrepancy between the critical growth rate of the NAL and NRL fibres is observed, as the NRL fibres appears to have a critical growth rate between 100 µm s^{-1} and 1000 µm s^{-1}. As the composition is the same, the resulting increased stability in the smaller fibres might be due to capillarity, as seen for the CRL fibres. However, the NRL fibres have much more glass, as they are redrawn into SiO_2 capillaries, which could allow for higher thermal gradients. An increase in the thermal gradient would lead to an increase in the critical growth rate. Is it not possible to determine which effect is the dominant without further experiments.

As expected from theory, both the NAL and NRL samples have lower critical growth velocities than the CAL and CRL counterparts, illustrating the difficulty of growth where the miscibility gap is at it's largest. However, homogeneous growth was achieved for both at velocities far beyond what is usually cited in literature. There is also an increase in growth velocity for both compositions with a reduction of core diameter. This suggests that the reduced dimensions of the fibres stabilise the growth interface.

The inhomogeneous, laser treated samples are suspected to not represent the truth. All measurements were allowed time to establish a melt zone before translation started, however, it is unclear whether the meltzone is sustained at the higher rates or if recrystallisation is not occurring. This uncertainty means that, although samples are inhomogeneous after translation at velocities above $200\,\mu m\,s^{-1}$ for CA, it does not mean that the critical growth velocity was surpassed. It might simply be that the melt zone was not sustained during the scan. At such high scan velocities, tracking the melt zone with the camera was not feasible. The main problem with sustaining the melt zone at high scan velocities is that it requires a lot of power from the CO_2 laser, which in turn damages the glass. It becomes a balance of laser power versus scan velocity, so to melt the core without melting or destroying the glass cladding.

In general, recrystallisation by the CO_2 laser does not damage the interface between the SiGe core and the cladding as much as the tube furnace (compare e.g. figure B.6 to figure B.5). For waveguide applications, the laser annealed samples appear to be much more promising than the tube furnace annealed, due to a homogeneous composition and a better preserved interface. Preliminary results of waveguide losses for the laser annealed fibres indicate losses between $10\,dB\,cm^{-1}$ and $20\,dB\,cm^{-1}$, whereas no light was transmitted for the untreated sample [2]. The inhomogeneous samples achieved in the tube furnace might be applicable for solar cells, as polycrystalline SiGe will have a tuned band gap. This can increase the spectral response of a multicrystalline SiGe solar cell at longer wavelengths [69].

In this section, two things have been shown. Firstly, it has been shown that the extreme thermal gradient induced by the CO_2 laser will theoretically allow for critical growth velocities for homogeneous growth far beyond what is achievable in most growth techniques. This has also been confirmed experimentally. Secondly, the redrawn samples investigated have been shown to exceed the theoretical estimates. It is suspected that the increased growth interface stability is due to the dimensions of the fibres as well as the extreme thermal gradients. The stability increase due to dimensions is supported by the inverse dependency of growth rate to core diameter, seen for both CA versus CR and NA versus NR.

---

[2] Personal communication with professor Ursula J. Gibson, Department of Physics, NTNU.

4.2 EDS analysis

A thorough investigation by EDS was performed with the goal of answering two important questions: 1, Does the Ge content change upon recrystallisation and 2, does recrystallisation introduce oxygen into the sample? Understanding the effect on composition for the heat treatments is essential, as any introduced oxygen can be detrimental for optical properties. EDS was used on several untreated samples, and samples treated by both heat treatments. Table 4.1 presents EDS results from several relevant samples. Calculating the average compositions for all gives a statistical measure of any change in the material due to the heat treatment. Average composition and standard deviation is calculated for the CA+CR and NA+NR samples and is presented in tables 4.2 and 4.3, respectively.

The change in average composition for the treated versus untreated samples is less than the standard deviation for all constituents, suggesting that the composition is not altered significantly by the treatments. Table 4.1 shows significant compositional variations in the untreated samples, thus making it hard to conclude whether e.g. the different scan velocities influence the composition in different ways.

The uncertainty in the measurements is further enlarged by the fact that each single EDS measurement will have an uncertainty. Two important sources of error for EDS measurements is detector noise, as well as error associated with the ZAF-correction, with respect to e.g. the curve fitting. The error on a single measurement due to the analysis is,based on the Espirit 1.9.4 software, approximately 0.8at% for Ge and 0.25at% for O. Additionally, the error from quantification area discussed in section C further increases the error of single measurements. All in all, any conclusion on introduction of oxygen or change in composition on a sample by sample basis is very open to error.

On a statistical basis, it can be concluded that the heat treatments do not alter the composition of the fibres any detectable amount.

Table 4.1: EDS results for several untreated and treated samples. Each measurement is done at a random cross-section, thus variations in composition for the inhomogeneous samples are expected to be significant.

Sample	Si [at%]	Ge [at%]	O[at%]
Untreated 1	90.57	5.71	3.72
Untreated 2	90.02	6.60	3.38
Untreated 3	89.70	5.90	4.40
Untreated 4	91.12	5.85	3.03
Untreated 5	92.78	4.41	2.80
Untreated 6	92.46	5.41	2.13
Untreated 7	93.21	4.81	1.90
XRT Standard	92.21	5.27	2.52
CAL10-2	91.54	6.02	2.31
CAL50-1	91.29	5.15	2.56
CAL100-2	92.03	5.66	2.31
CAL1000-2	92.50	4.45	3.05
CRL100-1	92.01	5.65	2.34
NR Untreated	56.43	41.65	1.92
NRL10-1	56.79	39.38	3.38
NRL100-1	55.16	40.47	4.4
NRL1000-1	60.17	36.53	3.29
CAO2B	92.87	3.96	3.17
CAO2R	93.85	3.49	2.66
CAO4B	89.27	7.77	2.96
CAO4C	92.43	4.99	2.58
CAO4R	91.2	5.17	3.63
CAO4RC	90.04	5.54	4.42

Table 4.2: Average composition and standard deviation for the treated CA samples compared to untreated CA.

	Untreated			Treated		
	Si [at%]	Ge [at%]	O [at%]	Si [at%]	Ge [at%]	O [at%]
Average composition	91.40	5.50	3.10	91.70	5.22	3.08
Standard Deviation	1.34	0.68	0.84	1.35	1.19	0.65

Table 4.3: Average composition and standard deviation for the treated NA samples compared to untreated NA.

	Untreated			Treated		
	Si [at%]	Ge [at%]	O [at%]	Si [at%]	Ge [at%]	O [at%]
Average composition	57.39	39.37	3.26	58.23	39.1	3.1
Standard Deviation	0.97	1.27	1.53	2.62	2.67	1.02

4.3 Crystallinity

So far it has been shown that the thermal treatments alter the Ge-distribution in the samples without changing the overall composition of the fibres. Three samples were selected for in-depth studies by EBSD and µ-Raman to investigate how the treatments affect the crystallinity and strain of the samples: An untreated CA sample, the CAO2B sample due to its large regions of different composition, and CAL100-2 due to homogeneity. EBSD was performed to investigate if the samples were crystalline, and whether or not the inhomogeneous samples were polycrystalline or have varying composition within a single crystal. The size of the analysed regions are restricted by charging of the cladding, as EBSD does not allow for any metallic coating. Despite charging, a manual investigation of the EBSD pattern over the whole face was performed in for each sample. The results will be presented separately for each sample discussed in section 4.3.4.

4.3.1 Untreated Sample

Figure 4.27a presents an BSE SEM image of a region of large compositional variations in the untreated sample. A microstructural map is presented in figure 4.27b, showing that the whole region is single crystalline. Manual inspection over the whole face revealed that the entire face is single crystalline. The presented results show that despite severe compositional inhomogeneity, the crystal structure is the same for the whole face. There might, however, be a slight gradual reorientation of the structure, as seen in figure 4.27b. The reorientation does not seem to correspond in any way with the compositional variations though.

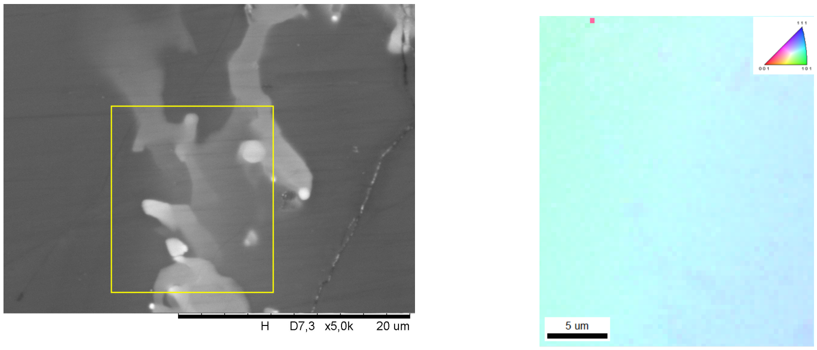

(a) (b)

Figure 4.27: BSE SEM micrograph of the untreated CA smaple, with the area investigated by EBSD marked by the yellow rectangle (a) and a microstructural map captured by EBSD (b). The area is single crystalline, but there is a small, gradual change of orientation.

4.3.2 CAO2B

The CAO2B tube furnace annealed sample was investigated due to the abrupt discrete compositional changes, contained within specific areas, as seen in e.g. figures 4.8a, 4.8b, 4.8c and 4.8d. EBSD was performed on the region within the yellow rectangle presented in figure 4.28a, clearly covering areas of different composition. The resulting microstructural map is presented in figure 4.28b, revealing a single crystalline material. Manual inspection over the whole face confirmed that the whole face was single crystalline. The deviations from the single crystalline structure seen in figure 4.28b was due to scratches on the investigated surface.

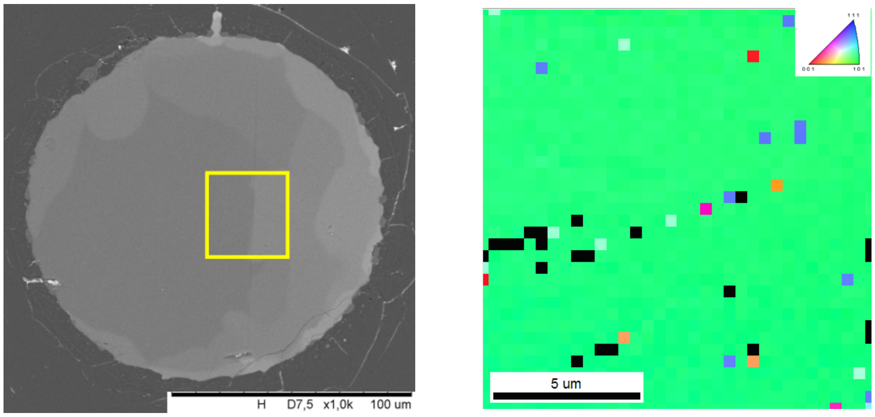

(a) (b)

Figure 4.28: BSE SEM micrograph the CAO2B sample, with the area investigated by EBSD marke in yellow (a) and a microstructural map captured by EBSD (b). The area is single crystalline, but there are some deviations due to damage in the surface.

4.3.3 CAL100-2

EBSD analysis was performed on the sample CAL100-2 inside the region marked by the yellow rectangle in figure 4.29a. The composition of the sample was homogeneous, and EBSD confirmed that the sample is also single crystalline, as seen in figure 4.29b. The area outside the rectangle was confirmed to be a single crystal by manual inspection.

4.3.4 Recrystallisation Effect on Crystallinity

Section 4.3.1 showed that the untreated CA samples are single crystalline, despite the severe compositional variations presented in section 4.1. Slow cooling changed the the compositional distribution, resulting in discrete areas of varying composition, resembling

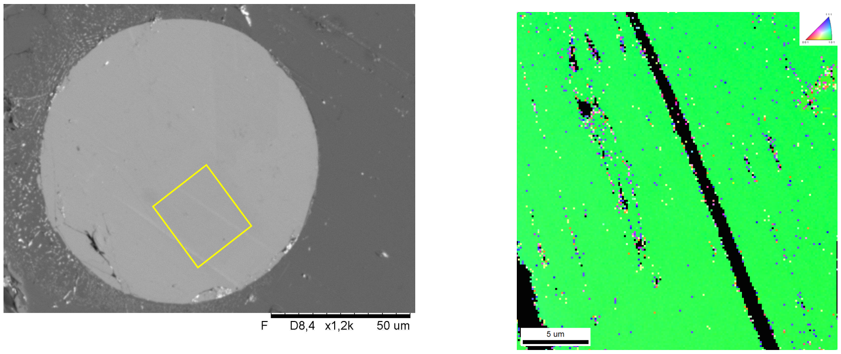

(a)

(b)

Figure 4.29: BSE SEM micrograph the CAL100-2 sample, with the area investigated by EBSD marke in yellow (a) and a microstructural map captured by EBSD (b). The area is single crystalline, and the two large areas without signal corresponds to the distinct scratches seen in (a).

different grains. However, the resulting microstructure is single crystalline. The SiGe fibres are capable incorporating large compositional variances without forming a polycrystalline material. Comparing the results for the tube furnace annealed fibres with the multicrystalline SiGe produced by Usami *et al.* [69] using similar cooling rates suggests that the geometry of the fibres impact the resulting microstructure. Section 4.4.2 will investigate strain related to the sudden compositional changes. The CAL100-2 sample also has a single crystalline face. Preliminary XRD measurements on CAL100-2 suggests that the whole treated section of the fibre is single crystalline [3]. This indicates that not only are the CO_2 treated samples of homogeneous composition throughout the sample, but also a single crystal. It is worth noting that the orientation of the untreated sample is between (111) and (101), whereas both treated sample have a (101) orientation. The reason is not clear and further investigations are needed.

4.4 Strain

The strain in the fibres was analysed using µ-Raman spectroscopy. Results will again be presented for the three samples investigated in section 4.3. The areas investigated are approximately the same as for the EBSD analysis. Understanding strain in SiGe is important as strain will alter e.g. the bandgap. For Raman analysis, x is Ge content.

---

[3] Personal communication with professor Dag W. Beriby, Department of Physics, NTNU.

4.4.1 Untreated Sample

µ-Raman spectroscopy on the untreated sample resulted in complex results. A scan was performed along the line shown in figure 4.30. Figure 4.31 shows the spectra captured at a separation of 0.5 µm. The line scan starts out with a high-Ge content area. Considering the Raman spectra from the blue line scan there are two Si−Si peaks present at the start, suggesting two different species of SiGe present. This might occur by having two areas of different composition, different strain or a combination of the two. As the area is highly inhomogeneous it might be sampling from two regions of very different composition. With a spot size of approximately 4 µm, a small area outside the Ge-rich spot will be measured. Figure 4.32 presents spectrum 4, from inside the yellow triangle, peak fitted. The two Si-Si peaks are located at 512.8 cm^{-1} and 485.6 cm^{-1}. Some important peak parameters are presented in table 4.4. As the Si−Ge peak is well-defined relative to the case of low

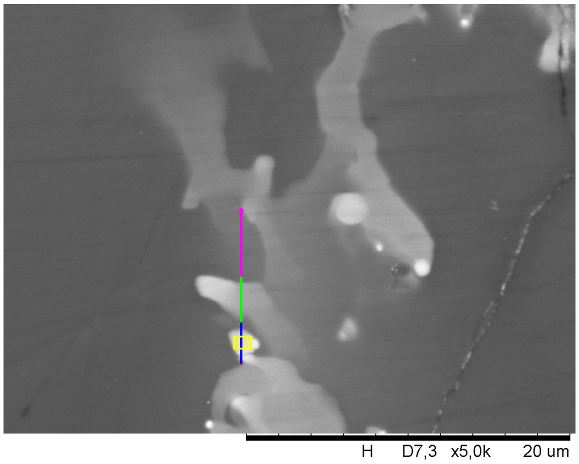

Figure 4.30: BSE SEM micrograph of line scanned by µ-Raman for an untreated sample. The scanned line is marked by different colours, each section corresponding to the spectra marked by the same colour in figure 4.31.

Table 4.4: Peak parameters of the fitted peaks in figure 4.32

Position cm^{-1}	Area	Height	FWHM
512.8	30160.0	3836.7	7.4
485.8	128382.0	7134.4	12.5
399.0	121086.0	4331.4	20.3
282.1	93774.4	4289.6	18.4

Ge-content, the composition can be calculated using equation 3.6, giving a composition of:

$$x = 0.3321 \approx 33.2\text{at\%}$$

for the most shifted peak, and

$$x = 0.4146 \approx 4.1\text{at\%}$$

for the least shifted peak. EDS was performed to determine the Ge-content in the area marked by a yellow rectangle in figure 4.30. The area has a Ge-content of 34.5at%. The average composition of the fibre was measured by EDS to be 5.03at%. The two techniques are in agreement within the error due to peak placement of the Si−Ge peak as well as the EDS error. Using the measured composition of the Ge-rich area, the strain can be calculated for the highly shifted Si-Si peak using equation 3.4a:

$$\epsilon = 0.013 \pm 0.0005 \approx 1.3\%$$

The region has substantially more strain than the a homogeneous fibre presented in section 3.3.5.4. Comparing this to the maximum strain achievable by epitaxial growth is

$$\epsilon_{\text{max}} = 4.17\%$$

[68], the results suggest a significantly strained structure. There is no splitting on the second Ge-rich region (green line), yet there is a shift of the peak position. The Si−Si peak is located at 508.1 cm^{-1}, corresponding to Ge content of 16.8at% assuming no strain. Again, EDS was performed along the area, revealing a Ge content of 16.2at%. This suggests that the area is not strained.

Finally, in the magenta line scan, the peak position is the sample as the least shifted peak in the start of the scan. This suggests that the peak from the start is from the Ge-poor region.

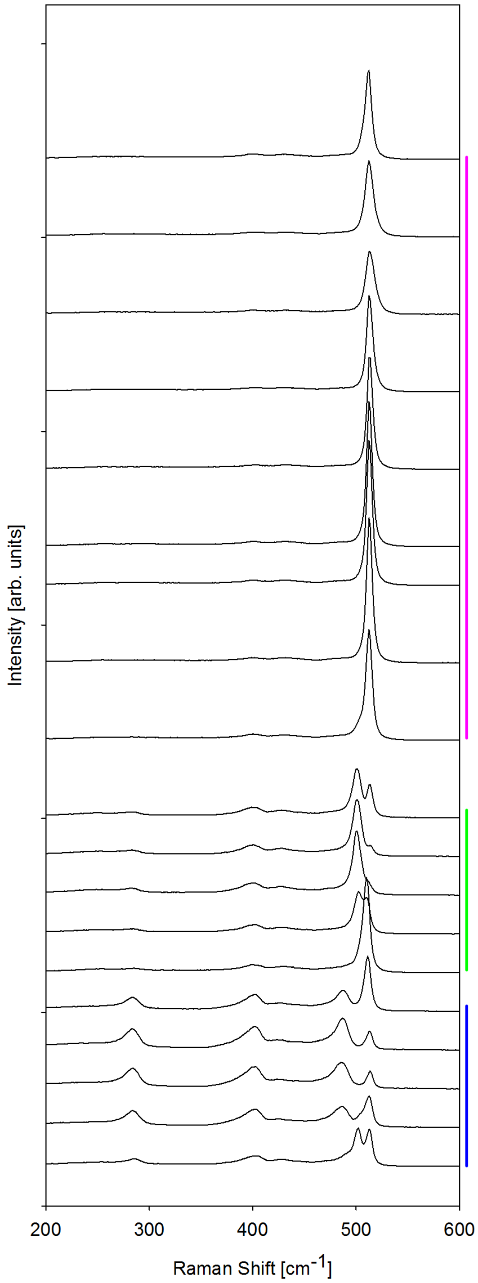

Figure 4.31: Raman spectra for the line scan marked in figure 4.30. The spectra are colour-coded to show where they belong in the scan, and the magenta spot marks the end of the scan, corresponding to the top spectrum.

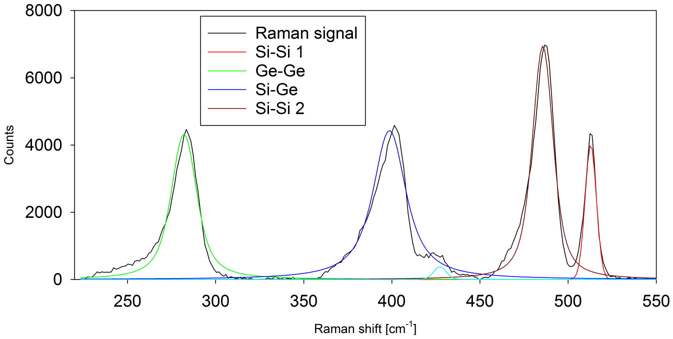

Figure 4.32: Peak fitted spectrum from the initial Ge-rich section in the line scan of the untreated CA sample.

4.4.2 CAO2B

The CAO2B sample is single crystalline with well defined areas of varying composition. This allows for investigations of strain related to the interface of different regions in the sample. As the Ge-content for the CA fibres is very low, the Si−Ge and Ge−Ge peaks suffer from severe broadening. Due to the broadening and weak signal, the Ge−Ge and Si−Ge peaks can in general not be used accurately to determine composition and strain for samples of $x < 0.3$ for SiGe [68]. Therefore, only the Si−Si peak will be considered. Figure 4.34 present the shift, integrated area and full-width half-maximum along the line scan marked by the red arrow in figure 4.33. The integrated area and FWHM deviate from local average values by a significant amount. This can likely be attributed to external factors, such surface roughness, and thus qualitative analysis based on area and FWHM is not accurate as analysis based on the shift [69]. The change in FWHM occuring at compositional transitions is probably due to the spot size covering a range of composition, leading to a broadening.

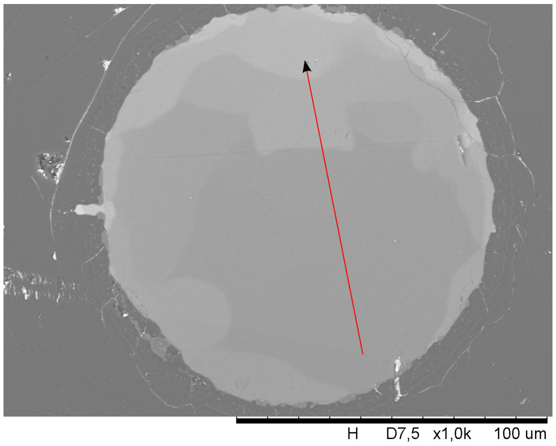

Figure 4.33: Micrograph of the CAO2B sample, with the line scanned with µ-Raman marked by the red arrow. The scan covers three regions of different composition.

In order to investigate if there is any strain in the material, especially in proximity to a grain boundary, the virtual Ge-composition can be calculated along the scan. The virtual Ge-composition can be defined as the composition calculated by rearranging equation 3.4a, and assuming a completely strain-relaxed material [69]:

$$x = \frac{520 - \omega_{Si-Si}}{70.5} \tag{4.5}$$

The virtual composition is calculated using equation 4.5 and plotted in figure 4.34d. EDS

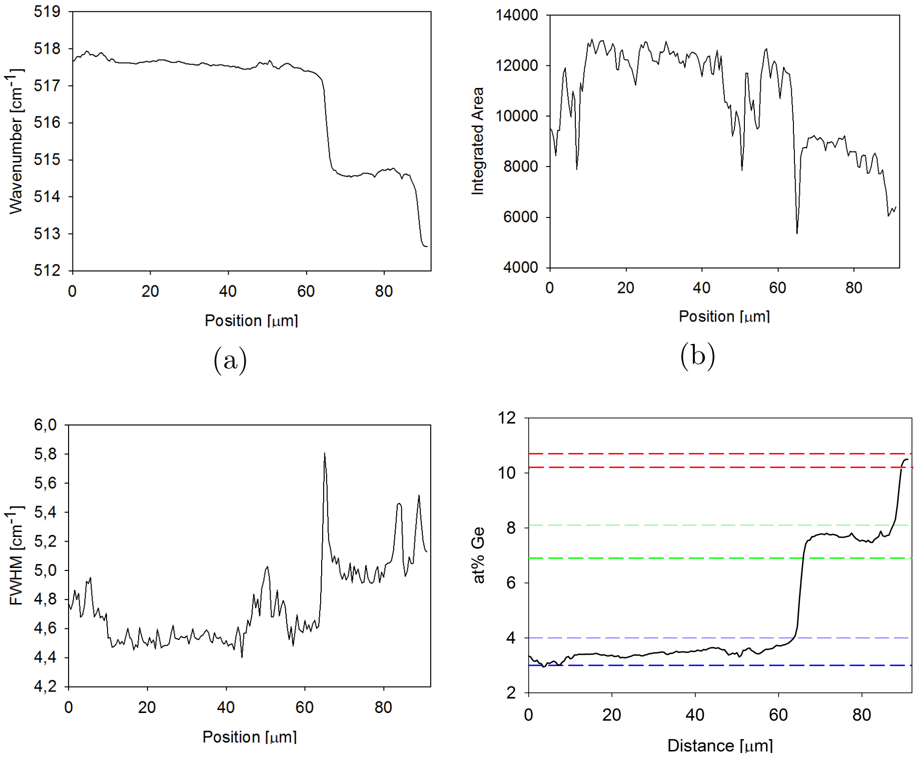

(a) (b) (c) (d)

Figure 4.34: Plots of the shift, integrated area and FWHM of the Si−Si peak of the spectra from the scanned line in 4.34. As the integrated area (b) and FWHM (c) depend strongly on external effects such as surface damage, the signal is noisy and not applicable for thorough analysis. The shift (a) is very little affected giving a good signal. Figure (d) present the virtual composition calculated using equation 4.5. The dashed lines in (d) show the upper and lower composition for each area determined by EDS.

analysis was performed on each of the grains to calculate the composition. The measured compositions were, following the scan, 3.43at%, 7.40at% and 10.18at%.

There does not appear to be strain associated with the discrete compositional changes, as the transition between grains is smooth, unlike the results presented by Usami *et al.* [69]. This confirms the results of a single crystalline face from EBSD. There is not a perfect overlap between the composition as calculated by µ-Raman and EDS. The largest discrepancy is approximately $\delta x = 0.31$at%. This is within the error of EDS measurements shown in section 4.2.

4.4.3 CAL100-2

A µ-Raman mapping was performed on a homogeneous CAL100 sample to investigate if the homogeneous samples contain any strain. Figure 4.35 shows a BSE SEM micrograph of the sample and the same image with the Raman map on the corresponding locations. The darkest shade of red corresponds to approximately $515.1\,\mathrm{cm}^{-1}$. The map shows the shift of the Si−Si peak at each position. The maximum shifts are approximately $1.2\,\mu\mathrm{m}^{-1}$. The physically damaged areas show the largest shifts, evident from the distinct scratches, whereas everywhere else the shift is in the order of $x \approx 0.7$, which is within the error of peak fitting [70]. The shifts in the damaged areas are mainly due to the decrease in intensity and increase in FWHM, making the peak harder to fit. Thus, no conclusion can be made on strain relatd to physical defects in the surface. Based on the results presented in figure 4.35 it appears that the homogeneous samples contain little or no stress compared to the untreated sample.

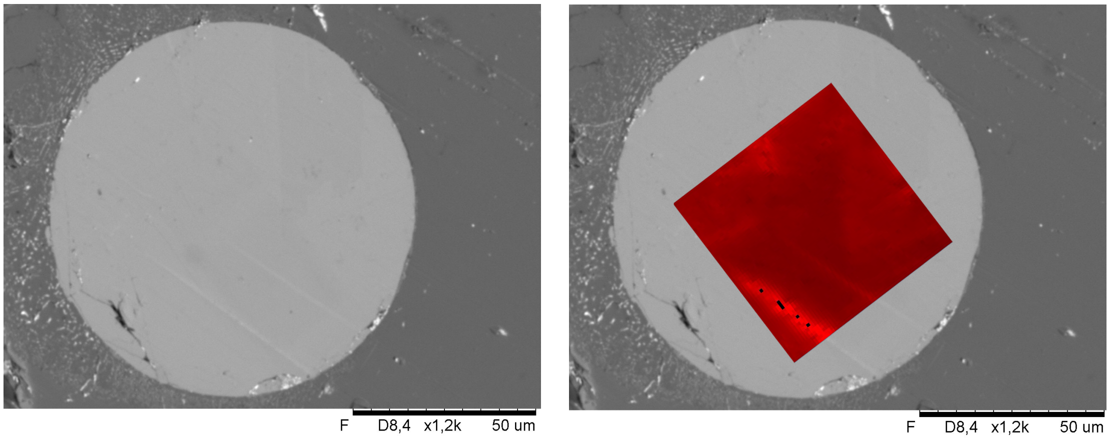

(a) (b)

Figure 4.35: BSE SEM image of a homogeneous sample (a), and with a Raman mapping layered on top of the SEM image (b). There are shifts related to physical defects on the surface, but outside damage areas the shift is constant within the expected error.

4.4.4 Strain Reduction

Section 4.4.1 showed that there is significant strain present in the Ge-rich regions of the untreated fibres. Comparing this to the results presented foor the samples CAO2B and CAL100-2 suggests that both heat treatments reduce the strain. As substantial strain is apparently only present in the areas of high Ge-content (> 30at%) in the untreated, removing the concentrated regions of Ge explains the reduction in strain.

Chapter 5

Conclusion

Theory suggests that the critical velocity for uniform crystal growth should be higher for reduced dimensions, stoichiometries close to the pure constituents, and high thermal gradients. In this project, two different recrystallisation techniques have been applied to SiGe fibres and the results investigated by several, complementary characterisation techniques. The main body of the work was on recrystallisation by zone melting using a CO_2 laser. Two different composition fibres were tested: low Ge content (5 at%) fibres drawn at Clemson University and high Ge content (40 at%) fibres hand-drawn at NTNU. As expected, a decrease in critical growth rate with increasing Ge content was shown, but it is not clear whether it is mainly due to changes in composition and liquidus slope, or if the thermal gradient changes due to less cladding. Based on filtered images of the melt zone, it is concluded that the CO_2 laser introduces extreme thermal gradients of $>14\,000\,°\mathrm{C\,cm^{-1}}$ for CA, allowing for the high growth velocities. By investigating two different core radii for each composition, it is shown that the reduced diameters increases the critical growth velocity for homogeneous growth significantly for CO_2 laser annealing. The high critical growth velocities between $200\,\mathrm{\mu m\,s^{-1}}$ and $1000\,\mathrm{\mu m\,s^{-1}}$ was surpassed by a substantial amount for the CR samples, with homogeneous growth at $1000\,\mathrm{\mu m\,s^{-1}}$. It is suspected that for the CR samples, a state of absolute interface stability is reached due to the small dimensions and the thermal diffusion induced by the extreme thermal gradients. EBSD analysis on both an untreated sample and a homogeneous, treated sample showed a single crystal face for both samples. Preliminary XRD results on a homogeneous, treated sample suggests that the entire treated section is a single crystal. µ-Raman analysis found approximately 1.3% strain related to a high Ge-content area in the untreated fibre, and no significant amount of sin the the homogeneous fibre. Zone recrystallisation using a CO_2 laser has been shown to be a very powerful technique for homogeneous, single crystalline growth of SiGe. In junction with the molten core fibre drawing technique, promising optical fibres have been made with preliminary measurements suggesting losses between 20 dB and 10 dB.

Oven annealing of CA fibres was performed to provide a baseline for these studies.

Two different cooling rates were tested, $1.5\,^{\circ}\mathrm{C\,min^{-1}}$ and $5\,^{\circ}\mathrm{C\,min^{-1}}$. Both horizontal and vertical positioning, though no apparent correlations were found in the resulting compositional distribution as a function of rate or positioning. CA samples recrystallised by slow cooling resulted in both homogeneous and inhomogeneous crystals, with no strain related to the discrete compositional variations. It is suspected that the homogeneous areas are of substantial size, but further investigations are needed. Cross-sectional investigation by EBSD of the inhomogeneous samples showed only one crystal orientation for the whole face. µ-Raman analysis over discrete compositional changes showed no significant amount of strain related to the changes. The absence of strain at the discrete compositional changes supports the claim that the face is single crystalline, as grain boundaries in polycrystalline SiGe has been show to have related strain.

Further Work

Zone recrystallisation with use of a CO_2 laser has been shown in this thesis to be a very powerful technique for production of homogeneous, single crystalline fibres, allowing for high growth velocities and control over the growth interface. The next step is to develop the technique with respect to the production of low-loss optical fibres from the molten core fibre drawing technique employed in the thesis. A thorough investigation on critical growth velocity should be made, investigating more scan velocities above $100\,\mu\mathrm{m\,s^{-1}}$ to determine the critical growth velocity more accurately. This includes ensuring that the melt zone is sustained at higher velocities. Additionally, radii between the two extremes tested ought to be investigated to further examine the effect of fibre size with respect to growth velocity. Production should be done in a fibre tower to ensure similar amounts of cladding, thus limiting any change of critical growth velocity to size effects.

More thorough investigations on losses in the recrystallised fibres should be done. The different scan velocities and radii fibres should be investigated, how losses depend on each parameter. Low-loss fibres recrystallised at a high velocity would be of great interest in combination with the rapid fibre production from the fibre tower. Part of the process should also be on different interface modifiers with the goal of reducing the overall oxygen levels in the fibres.

Due to problems with the XRT instrument at the end of the thesis, an in-depth study of several samples remains and should be done. Especially the homogeneous tube-furnace samples, to determine how large the homogeneous sections are. Additionally, the CO_2 set-up used allows for a high degree of control over the growth interface, which ought to allow for controlled compositional variations. This can be used to make e.g. compositional gratings in the fibres.

Bibliography

[1] A. Goetzberger, C. Hebling, and H. Schock. Photovoltaic materials, history, status and outlook. *Materials Science and Engineering: R: Reports*, 40:1–46, 2003.

[2] G. J. Snyder and E. S. Toberer. Complex thermoelectric materials. *Nature Materials*, 7:105–114, 2008.

[3] J. Bardeen and W. H. Brattain. The transistor, a semi-conductor triode. *Physical Review*, 74:230–231, 1948.

[4] D. J. Paul. Si/SiGe heterostructures: from material and physics to devices and circuits. *Semiconductor Science and Technology*, 19:R75–R108, 2004.

[5] F. Guarin, Z. Yang, and G. Freeman. Very high speed SiGe heterojunction bipolar transistor reliability overview. In *Proceedings of the 6th International Caribbean Conference on Devices, Circuits and Systems*, pages 131–136, 2006.

[6] T. P. Pearsall, J. M. Vandenberg, R. Hull, and J. M. Bonar. Structure and optical properties of strained ge-si superlattices grown on (001) ge. *Physical Review Letters*, 63:2104–2107, 1989.

[7] N. Usami, Y. Azuma, T. Ujihara, G. Sazaki, K. Nakajima, Y. Yakabe, T. Kondo, S. Koh, Y. Shiraki, B. Zhang, Y. Segawa, and S. Kodama. SiGe bulk crystal as a lattice-matched substrate to GaAs for solar cell applications. *Applied Physics Letters*, 77:3565–3567, 2000.

[8] J. Schilz and V. N. Romanenko. Bulk growth of silicon-germanium solid solutions. *Journal of Materials Science: Materials in Electronics*, 6:265–279, 1995.

[9] C. M. Bhandari and D. M. Rowe. Silicon-germanium alloys as high-temperature thermoelectric-materials. *Contemporary Physics*, 21:219–242, 1980.

[10] X. W. Wang, H. Lee, Y. C. Lan, G. H. Zhu, G. Joshi, D. Z. Wang, J. Yang, A. J. Muto, M. Y. Tang, J. Klatsky, S. Song, M. S. Dresselhaus, G. Chen, and Z. F. Ren.

Enhanced thermoelectric figure of merit in nanostructured n-type silicon germanium bulk alloy. *Applied Physics Letters*, 93:193121, 2008.

[11] H. Stöhr and W. Klemm. Über zweistoffsysteme mit germanium. i. germanium/aluminium, germanium/zinn und germanium/silicium. *Zeitschrift für anorganische und allgemeine Chemie*, 241:305–323, 1939.

[12] R. W. Olesinski and G. J. Abbaschian. The GeSi (Germanium-Silicon) system. *Bulletin of Alloy Phase Diagrams*, 5:180–183, 1984.

[13] I. Yonenaga. Growth and fundamental properties of SiGe bulk crystals. *Journal of Crystal Growth*, 275:91–98, 2005.

[14] E. R. Johnson and S. M. Christian. Some properties of germanium-silicon alloys. *Physical Review*, 95:560–561, 1954.

[15] G. A. Morton, M. L. Schultz, and W. E. Harty. Infrared photoconductive detectors using impurity-activated germanium-silicon alloys. *Rca Review*, 20:599–634, 1959.

[16] L. Ekstrom and J. P. Dismukes. Precipitation of phosphorus from solid solution in Ge$-$Si alloy. *Journal of Physics and Chemistry of Solids*, 27:857–863, 1966.

[17] H. Kimura, H. Winston, D. J. O'Connor, and J. A. Henige. Silicon-Germanium alloys for infrared detection. volume 285, page 155, 1981.

[18] M. Kürten and J. Schilz. Czochralski growth of $\mathrm{Si_xGe_{1\text{-}x}}$ single crystals. *Journal of Crystal Growth*, 139:1–5, 1994.

[19] N. V. Abrosimov, S. N. Rossolenko, W. Thieme, A. Gerhardt, and W. Schrder. Czochralski growth of Si- and Ge-rich SiGe single crystals. *Journal of Crystal Growth*, 174:182–186, 1997.

[20] I. Yonenaga, A. Matsui, S. Tozawa, K. Sumino, and T. Fukuda. Czochralski growth of $\mathrm{Ge_{1\text{-}x}Si_x}$ alloy crystals. *Journal of Crystal Growth*, 154:275–279, 1995.

[21] I Yonenaga and M Nonaka. Czochralski growth of bulk crystals of $\mathrm{Ge_{1x}Si_x}$ alloys: II. Si-rich alloys. *Journal of Crystal Growth*, 191:393–398, 1998.

[22] I Yonenaga. Czochralski growth of heavily impurity doped crystals of GeSi alloys. *Journal of Crystal Growth*, 226:47–51, 2001.

[23] M. Yildiz, S. Dost, and B. Lent. Growth of bulk SiGe single crystals by liquid phase diffusion. *Journal of Crystal Growth*, 280:151–160, 2005.

[24] W. A Tiller, K. A Jackson, J. W Rutter, and B Chalmers. The redistribution of solute atoms during the solidification of metals. *Acta Metallurgica*, 1:428–437, 1953.

[25] H. Y. S. Koh, S. L. Chen, P. B. Griffin, and J. D. Plummer. High quality single-crystal laterally graded SiGe on insulator by rapid melt growth. *Electrochemical and Solid-State Letters*, 13:H281–H283, 2010.

[26] H. Y. S. Koh. *Rapid Melt Growth of Silicon Germanium for Heterogeneous Integration on Silicon.* Stanford University, 2011.

[27] J. Ballato, T. Hawkins, P. Foy, B. Yazgan-Kokuoz, C. McMillen, L. Burka, S. Morris, R. Stolen, and R. Rice. Advancements in semiconductor core optical fiber. *Optical Fiber Technology*, 16:399–408, 2010.

[28] W. W. Mullins and R. F. Sekerka. Stability of a planar interface during solidification of a dilute binary alloy. *Journal of Applied Physics*, 35:444–451, 1964.

[29] S. O'hara and A. F. Yue. The effect of thermal diffusion on the constitutional supercooling criteriaa comment. *Journal of Physics and Chemistry of Solids*, 28:2105–2106, 1967.

[30] H. Fredriksson and U. Akerlind. *Solidification and Crystallization Processing in Metals and Alloys.* John Wiley & Sons, 2012.

[31] R. J. D. Tilley. *Understanding Solids: The Science of Materials.* John Wiley & Sons, 2004.

[32] W. D. Callister. *Fundamentals of Materials Science and Engineering.* John Wiley & Sons, Inc., 2001.

[33] J. W. Mullin. *Crystallization.* Butterworth-Heinemann, 2001.

[34] M. Volmer and 1885-1965. Kinetik der phasenbildung. 1939.

[35] J. A. Burton, R. C. Prim, and W. P. Slichter. The distribution of solute in crystals grown from the melt. part i. theoretical. *The Journal of Chemical Physics*, 21:1987–1991, 1953.

[36] W. A. Tiller and J. W. Rutter. The effect of growth conditions upon the solidification of a binary alloy. *Canadian Journal of Physics*, 34:96–121, 1956.

[37] J. P. Dismukes and W. M. Yim. A survey of interface stability criteria in the elemental alloy systems: Ge-si, bi-sb, and se-te. *Journal of Crystal Growth*, 22:287–294, 1974.

[38] F. C. Campbell. *Phase Diagrams: Understanding the Basics.* ASM International, 2012.

[39] R. W. Olesinski and G. J. Abbaschian. The Ge−Si (Germanium-Silicon) system. *Bulletin of Alloy Phase Diagrams*, 5:180–183, 1984.

[40] C. M. Bhandari and D. M. Rowe. Silicon-germanium alloys as high-temperature thermoelectric-materials. *Contemporary Physics*, 21:219–242, 1980.

[41] G. Joshi, H. Lee, Y. Lan, X. Wang, G. Zhu, D. Wang, R. W. Gould, D. C. Cuff, M. Y. Tang, M. S. Dresselhaus, G. Chen, and Z. Ren. Enhanced thermoelectric figure-of-merit in nanostructured p-type silicon germanium bulk alloys. *Nano Letters*, 8:4670–4674, 2008.

[42] G. Mahr Von Staszewski. Solidification of the GeSi (15 at% silicon) solid solution. *Journal of Materials Science Letters*, 10:451–454, 1991.

[43] I. Yonenaga, A. Matsui, S. Tozawa, K. Sumino, and T. Fukuda. Czochralski growth of $Ge_{1\text{-}x}Si_x$ alloy crystals. *Journal of Crystal Growth*, 154:275–279, 1995.

[44] A. Barz, P. Dold, U. Kerat, S. Recha, K. W. Benz, M. Franz, and K. Pressel. Germanium-rich SiGe bulk single crystals grown by the vertical bridgman method and by zone melting. *Journal of Vacuum Science & Technology B*, 16:1627–1630, 1998.

[45] J. K. Woodacre, D. Labrie, and M. Z. Saghir. Macrosegregation in vertical bridgman grown $Ge_{1\text{-}x}Si_x$ alloy with large melt volume: Limit of complete mixing. *Journal of Crystal Growth*, 327:35–41, 2011.

[46] M. Kürten and J. Schilz. Czochralski growth of $Si_xGe_{1\text{-}x}$ single crystals. *Journal of Crystal Growth*, 139:1–5, 1994.

[47] D. J. Paul. Si/SiGe heterostructures: from material and physics to devices and circuits. *Semiconductor Science and Technology*, 19:R75, 2004.

[48] D. J. Paul. Silicon-Germanium strained layer materials in microelectronics. *Advanced Materials*, 11:191–204, 1999.

[49] K. Kinoshita, H. Kato, M. Iwai, T. Tsuru, Y. Muramatsu, and S. Yoda. Homogeneous $In_{0.3}Ga_{0.7}As$ crystal growth by the traveling liquidus-zone method. *Journal of Crystal Growth*, 225:59–66, 2001.

[50] S. Adachi, Y. Ogata, N. Koshikawa, S. Matsumoto, K. Kinoshita, I. Yoshizaki, T. Tsuru, H. Miyata, M. Takayanagi, and S. Yoda. Homogeneous SiGe crystals grown by using the traveling liquidus-zone method. *Journal of Crystal Growth*, 280:372–377, 2005.

[51] H. Miyata, S. Adachi, Y. Ogata, T. Tsuru, Y. Muramatsu, K. Kinoshita, O. Odawara, and S. Yoda. Crystallographic investigation of homogeneous SiGe single crystals grown by the traveling liquidus-zone method. *Journal of Crystal Growth*, 303:607–611, 2007.

[52] P. J. Goodhew, J. Humphreys, and R. Beanland. *Electron Microscopy and Analysis, Third Edition.* CRC Press, 2000.

[53] J. I. Goldstein. Scanning electron microscopy and x-ray microanalysis, 2007.

[54] F. Mandl. *Quantum Mechanics.* John Wiley & Sons, 2013.

[55] P. Hovington, D. Drouin, and R. Gauvin. CASINO: A new monte carlo code in c language for electron beam interaction .1. description of the program. *Scanning*, 19:1–14, 1997.

[56] R. Shimizu and Ding Ze-Jun. Monte carlo modelling of electron-solid interactions. *Reports on Progress in Physics*, 55:487, 1992.

[57] K. Kanaya and S. Okayama. Penetration and energy-loss theory of electrons in solid targets. *Journal of Physics D: Applied Physics*, 5:43, 1972.

[58] R. Egerton. *Physical Principles of Electron Microscopy: An Introduction to TEM, SEM, and AEM.* Springer Science & Business Media, 2006.

[59] J. Goldstein. *Scanning Electron Microscopy and X-ray Microanalysis: Third Edition.* Springer US, 2003.

[60] D. B. Williams and C. B. Carter. High-resolution TEM. In *Transmission Electron Microscopy*, pages 483–509. Springer US, 2009.

[61] J. Als-Nielsen and D. McMorrow. *Elements of Modern X-ray Physics.* John Wiley & Sons, 2011.

[62] N. Colthup. *Introduction to Infrared and Raman Spectroscopy.* Elsevier, 2012.

[63] E. F. Nordstrand, A. N. Dibbs, A. J. Eraker, and U. J. Gibson. Alkaline oxide interface modifiers for silicon fiber production. *Optical Materials Express*, 3:651–657, 2013.

[64] C. Hou, X. Jia, L. Wei, S. C. Tan, X. Zhao, J. D. Joannopoulos, and Y. Fink. Crystalline silicon core fibres from aluminium core preforms. *Nature Communications*, 6:6248, 2015.

[65] A. Atkinson and S. C. Jain. Spatially resolved stress analysis using raman spectroscopy. *Journal of Raman Spectroscopy*, 30:885–891, 1999.

[66] F. Cerdeira, A. Pinczuk, Jc Bean, B. Batlogg, and Ba Wilson. Raman-scattering from gexsi1-x/si strained-layer superlattices. *Applied Physics Letters*, 45:1138–1140, 1984.

[67] K. Eberl, S. S. Iyer, S. Zollner, J. C. Tsang, and F. K. Legoues. Growth and strain compensation effects in the ternary $\mathrm{Si_{1\text{-}x}Y_x}$ alloy system. *Applied Physics Letters*, 60:3033–3035, 1992.

[68] J. C. Tsang, P. M. Mooney, F. Dacol, and J. O. Chu. Measurements of alloy composition and strain in thin $\mathrm{Ge_xSi_{1\text{-}x}}$ layers. *Journal of Applied Physics*, 75:8098–8108, 1994.

[69] N. Usami, T. Takahashi, K. Fujiwara, T. Ujihara, G. Sazaki, Y. Murakami, and K. Nakajima. Evidence of the presence of built-in strain in multicrystalline SiGe with large compositional distribution. *Japanese Journal of Applied Physics Part 1-Regular Papers Short Notes & Review Papers*, 41:4462–4465, 2002.

[70] T. S. Perova, J. Wasyluk, K. Lyutovich, E. Kasper, M. Oehme, K. Rode, and A. Waldron. Composition and strain in thin si1xGex virtual substrates measured by micro-raman spectroscopy and x-ray diffraction. *Journal of Applied Physics*, 109:033502, 2011.

[71] J. H. Parker, D. W. Feldman, and M. Ashkin. Raman scattering by silicon and germanium. *Physical Review*, 155:712–714, 1967.

[72] V. M. Glazov and O. D. Shchelikov. Volume changes during melting and heating of silicon and germanium melts. *High Temperature*, 38:405–412, 2007.

[73] A. Yariv and P. Yeh. *Photonics: Optical Electronics in Modern Communications (The Oxford Series in Electrical and Computer Engineering)*. Oxford University Press, Inc., 2006.

[74] F. A. Martinsen, B. K. Smeltzer, M. Nord, T. Hawkins, J. Ballato, and U. J. Gibson. Silicon-core glass fibres as microwire radial-junction solar cells. *Scientific Reports*, 4, 2014.

[75] T. Sato. Spectral emissivity of silicon. *Japanese Journal of Applied Physics*, 6:339, 1967.

[76] H. K. Lin, H. Y. Chen, and C. W. Lan. Adaptive phase field modeling of morphological instability and facet formation during directional solidification of SiGe alloys. *Journal of Crystal Growth*, 385:44–48, 2014.

Appendices

Appendix A

MatLab Code

A.1 Analysis.m

```
%%%%%%%%%%%%%%%%%%%%%%%%%%%%%%%%%%%%%%%%%%%%%%%%%%%%%%%%%%%%%%%%%%%%%%%%%
%%%%%%%%%%%%%%%%%%%% INFO %%%%%%%%%%%%%%%%%%%%%%%%%%%%%%%%%%%%%%%%%%%%%%%
%%%%%%%%%%%%%%%%%%%%%%%%%%%%%%%%%%%%%%%%%%%%%%%%%%%%%%%%%%%%%%%%%%%%%%%%%

%To do: Gjr om ting funksjon som tar inn filnavn og i tillegg lagrer
%figurene som produseres. Legg til figurtekst osv...
%Lag og excel-fil med ndvendig informasjon? Renskriv.

%%%%%%%%%%%%%%%%%%%%%%%%%%%%%%%%%%%%%%%%%%%%%%%%%%%%%%%%%%%%%%%%%%%%%%%%%
%%%%%%%%%%%%%%%%%%%% Load Image %%%%%%%%%%%%%%%%%%%%%%%%%%%%%%%%%%%%%%%%%
%%%%%%%%%%%%%%%%%%%%%%%%%%%%%%%%%%%%%%%%%%%%%%%%%%%%%%%%%%%%%%%%%%%%%%%%%

Image_map=imread('C205RC_Treated_adjusted.png');
Sample='C205RC_treated';

[Row, Col] = size(Image_map);

%%%%%%%%%%%%%%%%%%%%%%%%%%%%%%%%%%%%%%%%%%%%%%%%%%%%%%%%%%%%%%%%%%%%%%%%%
%%%%%%%%%%%%%%%%%%%% Split image in two %%%%%%%%%%%%%%%%%%%%%%%%%%%%%%%%%
%%%%%%%%%%%%%%%%%%%%%%%%%%%%%%%%%%%%%%%%%%%%%%%%%%%%%%%%%%%%%%%%%%%%%%%%%


format long
Image_left = [];
Image_right = [];
```

```
for i = 1:Row
    Line_left = Image_map(i, 1:floor(Col/2));
    Image_left = [Image_left; Line_left];

    Line_right = Image_map(i, ceil(Col/2):Col);
    Image_right = [Image_right; Line_right];
end

%%%%%%%%%%%%%%%%%%%%%%%%%%%%%%%%%%%%%%%%%%%%%%%%%%%%%%%%%%%%%%%%%%%%%%%%
%%%%%%%%%%%%%%%%%%% Calculate core edges %%%%%%%%%%%%%%%%%%%%%%%%%%%%%%%
%%%%%%%%%%%%%%%%%%%%%%%%%%%%%%%%%%%%%%%%%%%%%%%%%%%%%%%%%%%%%%%%%%%%%%%%

Derivative_left = [];
Derivative_right = [];

Edge_Indices_left = [];
Edge_Indices_right = [];

Row_values = [];

for i=1:Row

    %Calculate the derivative
    Derivative_line_left=diff(Image_left(i,:));

    %For right part of image: flip, then derivate.
    Image_right_flipped = fliplr(Image_right);
    Derivative_line_right_flipped=diff(Image_right_flipped(i,:));
    Derivative_line_right = fliplr(Derivative_line_right_flipped);

    %Determine position of maxima of derivative
    [Values_left,Indices_left] = sort(Derivative_line_left);
    Edge_Indices_left = [Edge_Indices_left;

    Indices_left(length(Indices_left))];
    [Values_right,Indices_right] = sort(Derivative_line_right);
    Edge_Indices_right = [Edge_Indices_right;

     Indices_right(length(Indices_right))+Col/2];
    %Write column index for maxima of each row
    Row_values = [Row_values i];

end

Row_values=flipud(Row_values);

%%%%%%%%%%%%%%%%%%%%%%%%%%%%%%%%%%%%%%%%%%%%%%%%%%%%%%%%%%%%%%%%%%%%%%%%
%%%%%%%%%%%%%%%%%%% Iterate to further determine edge  %%%%%%%%%%%%%%%%%
%%%%%%%%%%%%%%%%%%%%%%%%%%%%%%%%%%%%%%%%%%%%%%%%%%%%%%%%%%%%%%%%%%%%%%%%



%%%%%%%%%%%%%%%%%%%%%%%%%%%%%%%%%%%%%%%%%%%%%%%%%%%%%%%%%%%%%%%%%%%%%%%%
%%%%%%%%%%%%%%%%%%% Find Centre %%%%%%%%%%%%%%%%%%%%%%%%%%%%%%%%%%%%%%%%
%%%%%%%%%%%%%%%%%%%%%%%%%%%%%%%%%%%%%%%%%%%%%%%%%%%%%%%%%%%%%%%%%%%%%%%%

Edge_Indices = [Edge_Indices_left Edge_Indices_right];

%Determine mean value for x and y. Crude method for determining centre
x_position_LR = mean(Edge_Indices); %Gives one value per column
x_position = mean(x_position_LR)
y_position = mean(Row_values)  %%%WRONG!

%%%%%%%%%%%%%%%%%%%%%%%%%%%%%%%%%%%%%%%%%%%%%%%%%%%%%%%%%%%%%%%%%%%%%%%%
%%%%%%%%%%%%%%%%%%% Determine Core Radius %%%%%%%%%%%%%%%%%%%%%%%%%%%%%%
%%%%%%%%%%%%%%%%%%%%%%%%%%%%%%%%%%%%%%%%%%%%%%%%%%%%%%%%%%%%%%%%%%%%%%%%

%Calculate distance to all points, then find mean value

Distances = [];

for i=1:Row

    x_length_left = x_position-Edge_Indices_left(i,1);
    x_length_right = x_position-Edge_Indices_right(i,1);
    y_length_left = y_position - Row_values(i);
    y_length_right = y_position - Row_values(i);

    D_left = sqrt(x_length_left.^2 + y_length_left.^2);
    D_right = sqrt(x_length_right.^2 + y_length_right.^2);
    Distances = [Distances; D_left D_right];

end

Mean_distances = mean(Distances);
Radius = mean(Mean_distances)-15;

%%%%%%%%%%%%%%%%%%%%%%%%%%%%%%%%%%%%%%%%%%%%%%%%%%%%%%%%%%%%%%%%%%%%%%%%
%%%%%%%%%%%%%%%%%%% Integrate: Power in the Bucket %%%%%%%%%%%%%%%%%%%%%
%%%%%%%%%%%%%%%%%%%%%%%%%%%%%%%%%%%%%%%%%%%%%%%%%%%%%%%%%%%%%%%%%%%%%%%%

%Will integrate "intensity" contained inside a given radius R
%and compare to area
%"intensity" inside the whole core.

%Calculate a matrix with distances to all points
Distances_Matrix = [];
Distances_vector = [];
for k=1:Row
    for j=1:Col

        D=sqrt((j-x_position)^2 + (k-y_position)^2);
        Distances_vector = [Distances_vector D];
    end
    Distances_Matrix = [Distances_Matrix; Distances_vector];
    Distances_vector = [];
end

%Integrate PIB
Partial_sum = 0;
Total_sum = 0;
All_Partials = [];

%Calcuate total "intensity"
Total_Matrix = Distances_Matrix < Radius;
Points = nnz(Total_Matrix);                 %Calculates number of non-zeros
Total_Matrix = +Total_Matrix;               %convert to double
Image_Map_double = im2double(Image_map);    %Convrts image file to double.
%Image_Map_double = 4.*Image_Map_double;
Total_Sum_Matrix = Total_Matrix.*Image_Map_double;
Total_Sum = sum(Total_Sum_Matrix(:));
```

```
Average_Point_Value = Total_Sum/Points;

Average_Matrix = Average_Point_Value*ones(Row, Col).*Total_Matrix;

%Calculate partials
Radii=[];
Radii2=[];
All_Partials = [];
All_Averages= [];
for r=1:Radius/100:Radius
    Partial_matrix1 = Distances_Matrix < r+1;
    Partial_matrix2 = Distances_Matrix > r-1;
    Partial_matrix = Partial_matrix1.*Partial_matrix2;
    Partial_matrix = +Partial_matrix;


    Partial_Sum_Matrix = Partial_matrix.*Image_Map_double;
    Partial_Sum_Matrix = +Partial_Sum_Matrix;
    Partial_Sum = sum(Partial_Sum_Matrix(:));

    Partial_Average_Sum_Matrix = Partial_matrix.*Average_Matrix;
    Partial_Average_Sum = sum(Partial_Average_Sum_Matrix(:));

    All_Partials = [All_Partials Partial_Sum];
    All_Averages = [All_Averages Partial_Average_Sum];

    Radii = [Radii r];
    Radii2 = [Radii2 r/Radius];
end



%%%%%%%%%%%%%%%%%%%%%%%%%%%%%%%%%%%%%%%%%%%%%%%%%%%%%%%%%%%%%%%%%%%%%%%%
%%%%%%%%%%%%%%%%%%% Integrate: Angular Distribution %%%%%%%%%%%%%%%%%%%%
%%%%%%%%%%%%%%%%%%%%%%%%%%%%%%%%%%%%%%%%%%%%%%%%%%%%%%%%%%%%%%%%%%%%%%%%

%Calculate a matrix with angles
Angles_Matrix = [];
Angles_vector = [];
for k=1:Row
    for j=1:Col
```

```
        x=j-x_position;
        y=k-y_position;
        if y<0
        Angle = acos(x/(sqrt((j-x_position)^2 + (k-y_position)^2)));
        Angles_vector=[Angles_vector Angle];
        else
        Angle = acos(x/(sqrt((j-x_position)^2 + (k-y_position)^2)));
        Angles_vector=[Angles_vector (2*pi - Angle)];
        end

    end
    Angles_Matrix = [Angles_Matrix; Angles_vector];
    Angles_vector = [];
end

All_Partials_Angles = [];
All_Averages_Angles = [];
Angles = [];
Reduced_Angles_Matrix=Angles_Matrix.*Total_Matrix;
step = (2*pi)/40;
half_step=step/2;
%Total_Sum_Matrix=Average_Matrix;
for Theta=0:step:(2*pi)
    Partial_Matrix_Angles1=Reduced_Angles_Matrix < (Theta+half_step);
    Partial_Matrix_Angles2=Reduced_Angles_Matrix > (Theta-half_step);
    Partial_Matrix_Angles = Partial_Matrix_Angles1.*Partial_Matrix_Angles2;
    Partial_Matrix_Angles=+Partial_Matrix_Angles;
    Reduced_Partial_Matrix_Angles=Partial_Matrix_Angles.*Total_Sum_Matrix;


    %Reduced_Partial_Sum_Matrix_Angles=
    %Reduced_Partial_Matrix_Angles.*Image_Map_double;
    %Reduced_Partial_Sum_Matrix_Angles=+Reduced_Partial_Sum_Matrix_Angles;
    Partial_Sum_Angles = sum(Reduced_Partial_Matrix_Angles(:));

    Partial_Average_Sum_Matrix_Angles=Partial_Matrix_Angles.*Average_Matrix;
    Partial_Average_Sum_Angles = sum(Partial_Average_Sum_Matrix_Angles(:));

    All_Partials_Angles = [All_Partials_Angles Partial_Sum_Angles];
    All_Averages_Angles = [All_Averages_Angles Partial_Average_Sum_Angles];
    Angles = [Angles Theta];

end

ratiorama=All_Partials_Angles./All_Averages_Angles;

%%%%%%%%%%%%%%%%%%%%%%%%%%%%%%%%%%%%%%%%%%%%%%%%%%%%%%%%%%%%%%%%%%%%%%%%
%%%%%%%%%%%%%%%%%%% Plot Data %%%%%%%%%%%%%%%%%%%%%%%%%%%%%%%%%%%%%%%%%%
%%%%%%%%%%%%%%%%%%%%%%%%%%%%%%%%%%%%%%%%%%%%%%%%%%%%%%%%%%%%%%%%%%%%%%%%

%plot detected edges and calculated centre.
figure
subplot(2,2,3);
hold on
scatter(flipud(Edge_Indices_left(:,1)), Row_values)
subplot(2,2,3)
scatter(flipud(Edge_Indices_right(:,1)), Row_values, 'r')
xlabel('x');
ylabel('y');

subplot(2, 2,3)
title('Detected edge')
scatter(x_position, y_position,50, 'filled', 'g')

%Plot radial distribution.
Reduced_Ratios = (All_Partials)./All_Averages;
subplot(2,2, 1)
plot(Radii2, Reduced_Ratios)
title('Radial dependency')
xlabel('Radius of "bucket"')
ylabel('Greyscale sum')

%plot angular distribution.
Ratios_Angles = (All_Partials_Angles./All_Averages_Angles);
subplot(2,2,2)
plot(Angles, Ratios_Angles)
title('Angular dependency')
xlabel('Angle')
ylabel('Greyscale sum')
```

```
%plot histogram of greyscale values.
subplot(2,2,4)
histogram(Image_Map_double)
title('Histogram of greyscale values')
xlabel('Greyscale value')
ylabel('Intensity')

subplot(2,2,1)
axis([0, 1, 0.96, 1.04])

subplot(2,2,2)
axis([0, Theta, 0.96, 1.04])

%%%%%%%%%%%%%%%%%%%%%%%%%%%%%%%%%%%%%%%%%%%%%%%%%%%%%%%%%%%%%%%%%%%%%%%%
%%%%%%%%%%%%%%%%%%% Calculate Sum of Least Squares %%%%%%%%%%%%%%%%%%%%%
%%%%%%%%%%%%%%%%%%%%%%%%%%%%%%%%%%%%%%%%%%%%%%%%%%%%%%%%%%%%%%%%%%%%%%%%

Radial_Least_Squares = (Radial_dependency(:,2)-1).^2;

Radial_Sum_Least_Squares = sum(Radial_Least_Squares);

ending3 = 'RadialSLS.CSV';
filename3=strcat(Sample, ending3);

csvwrite(filename3, Radial_Sum_Least_Squares);


Angular_Least_Squares = (Angular_dependency(:,2)-1).^2;

Angular_Sum_Least_Squares = sum(Angular_Least_Squares);

ending4 = 'AngularSLS.CSV';
filename4=strcat(Sample, ending4);

csvwrite(filename3, Radial_Sum_Least_Squares);
csvwrite(filename4, Angular_Sum_Least_Squares);



%%%%%%%%%%%%%%%%%%%%%%%%%%%%%%%%%%%%%%%%%%%%%%%%%%%%%%%%%%%%%%%%%%%%%%%%
%%%%%%%%%%%%%%%%%%% Save Data for SigmaPlot %%%%%%%%%%%%%%%%%%%%%%%%%%%%
```

```
%%%%%%%%%%%%%%%%%%%%%%%%%%%%%%%%%%%%%%%%%%%%%%%%%%%%%%%%%%%%%%%%%%%%%%%%%

Radial_dependency = [transpose(Radii2) transpose(Reduced_Ratios)];
Angular_dependency = [transpose(Angles) transpose(Ratios_Angles)];

    ending1 = 'Radial.CSV';    %creates file type ending string
    ending2 = 'Angular.CSV';
    filename1 = strcat(Sample, ending1);
    filename2 = strcat(Sample, ending2);

%csvwrite(filename1, Radial_dependency)
%csvwrite(filename2, Angular_dependency)

%%%%%%%%%%%%%%%%%%%%%%%%%%%%%%%%%%%%%%%%%%%%%%%%%%%%%%%%%%%%%%%%%%%%%%%%%
%%%%%%%%%%%%%%%%%%% End %%%%%%%%%%%%%%%%%%%%%%%%%%%%%%%%%%%%%%%%%%%%%%%%%
%%%%%%%%%%%%%%%%%%%%%%%%%%%%%%%%%%%%%%%%%%%%%%%%%%%%%%%%%%%%%%%%%%%%%%%%%
```

A.2 BlackBody.m

```
%-------------------------------------------------------------------------%
%---------Black Body Radiation--------------------------------------------%
%-------------------------------------------------------------------------%

clc;
close all;
clear all;

%-------------------------------------------------------------------------%

c=3*10^8; % speed of light in vaccum
h=6.625*10.^-34; %  Planck constant
k=1.38*10.^-23; %   Boltzmann constant
T=[1360+273 ]; % Temperatures in Kelvin
Lam=(0.0:0.01:15).*1e-6;


figure(1)
for i=1:length(T)

%------------Wiens Displacement Law---------------------------------------%
```

```
I1(:,i)= ((2*h*c*c)./(Lam.^5)).*(exp(-(h*c)./(Lam*k*T(i))));

%------------Planks Law--------------------------------------------------%

I2(:,i)=(2*h*c*c)./((Lam.^5).*(exp((h.*c)./(k.*T(i).*Lam))-1));

%------------------------------------------------------------------------%


%plot(Lam,I1(:,i),'linewidth',2)
hold on
%plot(Lam,I2(:,i),'r','linewidth',2)

%   text(.55e-5,.7e8,'500K','fontSize',14)
%   text(.5e-5,2e8,'600K','fontSize',14)
%   text(.8e-5,5e8,'T=700K','fontSize',14)
%
%   line([1.2e-5 1.4e-5], [6e8 6e8],'color','r','linewidth',2)
%   line([1.2e-5 1.4e-5], [5e8 5e8],'linewidth',2)
%
%   text(1.45e-5,6e8,'Plancks Law','fontSize',14)
%   text(1.45e-5,5e8,'Wiens Law','fontSize',14)


  xlabel('\lambda','fontsize',14)
  ylabel('Intensity','fontsize',14)
  title('Blackbody Radiation','fontsize',14)

  fh = figure(1);
  set(fh, 'color', 'white');
end

%------------Introduce Emissivity----------------------------------------%
%Data fitted to article, for liquid Si.
e_func = 0.68;
e = [];   %Emissivity matrix
for j=(0.0:0.01:15).*10^-6
    e = [e e_func];  %insert value to matrix
end
```

```
%Fitted data for SiO2 at 2000K

%------------Calculate Radiation---------------------------------------%
Spectrum1 = [];
Psecturm2 = [];

size(I1)
size(e)

Spectrum1 = I1(:,1).*e(:,2);
Spectrum2 = I2(:,1).*e(:,2);


%Create filter delta-step function
filter=zeros(1501,1);
filter(635)=1;

Filtered_spectrum1 = Spectrum1.*filter;
Filtered_spectrum2 = Spectrum2.*filter;


%plot(Lam, Spectrum1, 'b');
%plot(Lam, Spectrum2, 'r');
plot(Lam, Filtered_spectrum1, 'b')
%plot(Lam, Filtered_spectrum2, 'r')
```

Appendix B

SEM Images

B.1 Tube Furnace Annealed

B.1.1 CAO1

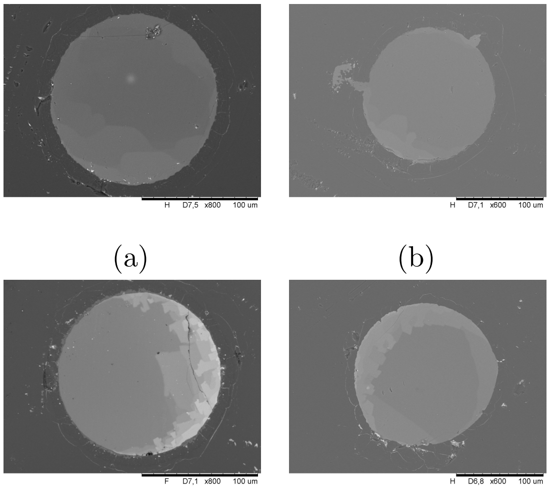
H D7,5 x800 100 um
H D7,1 x600 100 um
F D7,1 x800 100 um
H D6,8 x600 100 um

(a) (b)

(c) (d)

Figure B.1: BSE SEM micrograph of a reresentative untreated section of clemson fibre (a) and corresponding elemental EDS maps.

B.1.2 CAO2

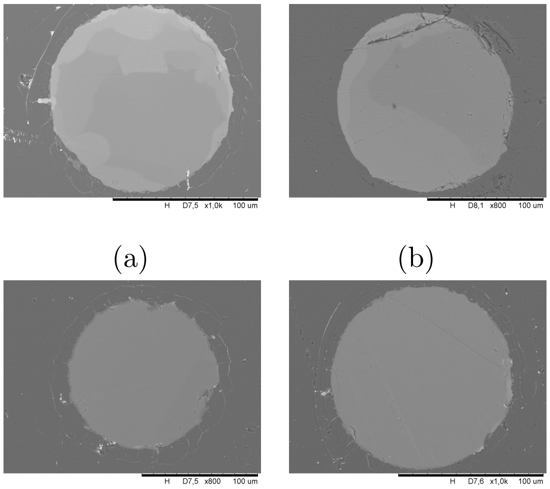
H D7,5 x1,0k 100 um
H D8,1 x800 100 um
H D7,5 x800 100 um
H D7,6 x1,0k 100 um

(a) (b)

(c) (d)

Figure B.2: BSE SEM micrograph of a reresentative untreated section of clemson fibre (a) and corresponding elemental EDS maps.

B.1.3 CAO3

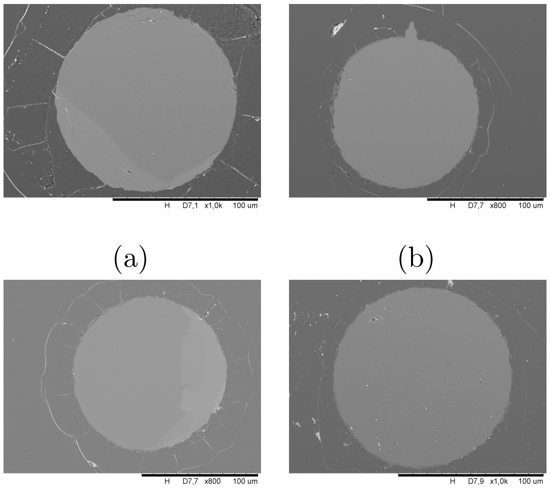
H D7,1 x1,0k 100 um
H D7,7 x800 100 um
H D7,7 x800 100 um
H D7,9 x1,0k 100 um

(a) (b)

(c) (d)

Figure B.3: BSE SEM micrograph of a reresentative untreated section of clemson fibre (a) and corresponding elemental EDS maps.

B.1.4 CAO4

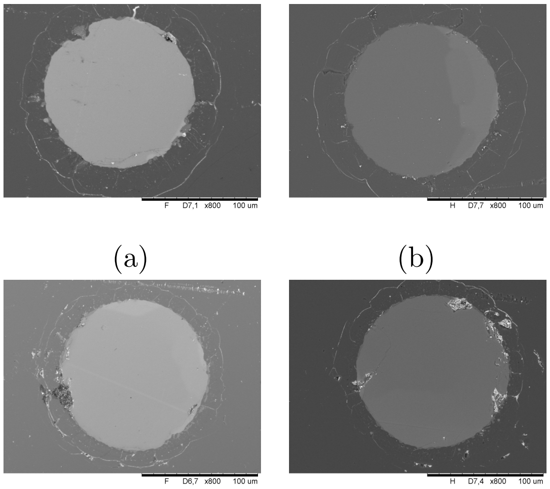
F D7,1 x800 100 um
H D7,7 x800 100 um
F D6,7 x800 100 um
H D7,4 x800 100 um

(a) (b)

(c) (d)

Figure B.4: BSE SEM micrograph of a reresentative untreated section of clemson fibre (a) and corresponding elemental EDS maps.

B.1.5 CAL

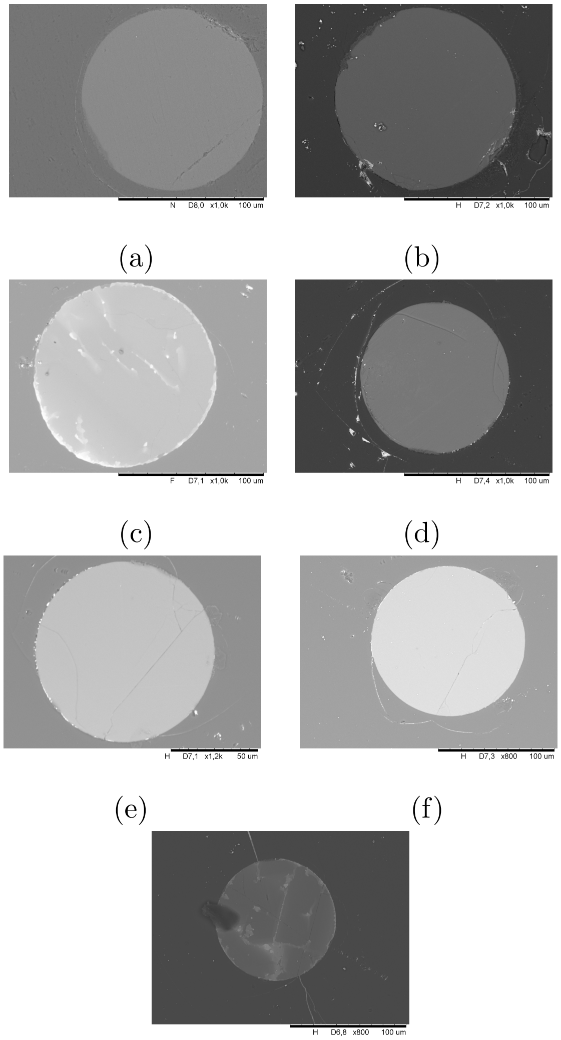
N D8,0 x1,0k 100 um
H D7,2 x1,0k 100 um
F D7,1 x1,0k 100 um
H D7,4 x1,0k 100 um
H D7,1 x1,2k 50 um
H D7,3 x800 100 um
H D6,8 x800 100 um

(a) (b)

(c) (d)

(e) (f)

(g)

Figure B.5: BSE SEM micrograph of a reresentative untreated section of clemson fibre (a) and corresponding elemental EDS maps.

B.2 NRL

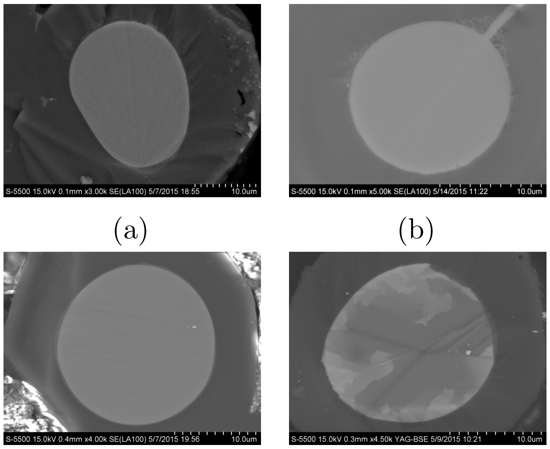
S-5500 15.0kV 0.1mm x3.00k SE(LA100) 5/7/2015 18:55 10.0um
S-5500 15.0kV 0.1mm x5.00k SE(LA100) 5/14/2015 11:22 10.0um
S-5500 15.0kV 0.4mm x4.00k SE(LA100) 5/7/2015 19:56 10.0um
S-5500 15.0kV 0.3mm x4.50k YAG-BSE 5/9/2015 10:21 10.0um

(a) (b)

(c) (d)

Figure B.6: BSE SEM micrograph of a reresentative untreated section of clemson fibre (a) and corresponding elemental EDS maps.

Appendix C

EDS Quantification Area Error

The area used for quantification in EDS does lead to some error. This is especially true for the measured oxygen content. Due to the interaction volume, measuring the whole core will show an increased oxygen content due to sampling from the SiO_2. Figure C.1 shows three different sampling areas and table C.1 summarises the compositions. An increase of 0.8at% is seen between the smallest and largest quantification areas. Additionally, with inhomogeneous Ge distribution, the measured composition further varies. These two effects add to the uncertainty of the technique.

Table C.1: Composition measured by EDS for the three different quantification areas marked in figure C.1. It is clear that an area close to the core measuredan increased oxygen content, which is due to the extent of the interaction volume into SiO_2.

	Composition [at%]		
Sample	Si	Ge	O
A	93.3	4.8	1.9
B	92.8	5.0	2.2
C	92.2	5.1	2.7

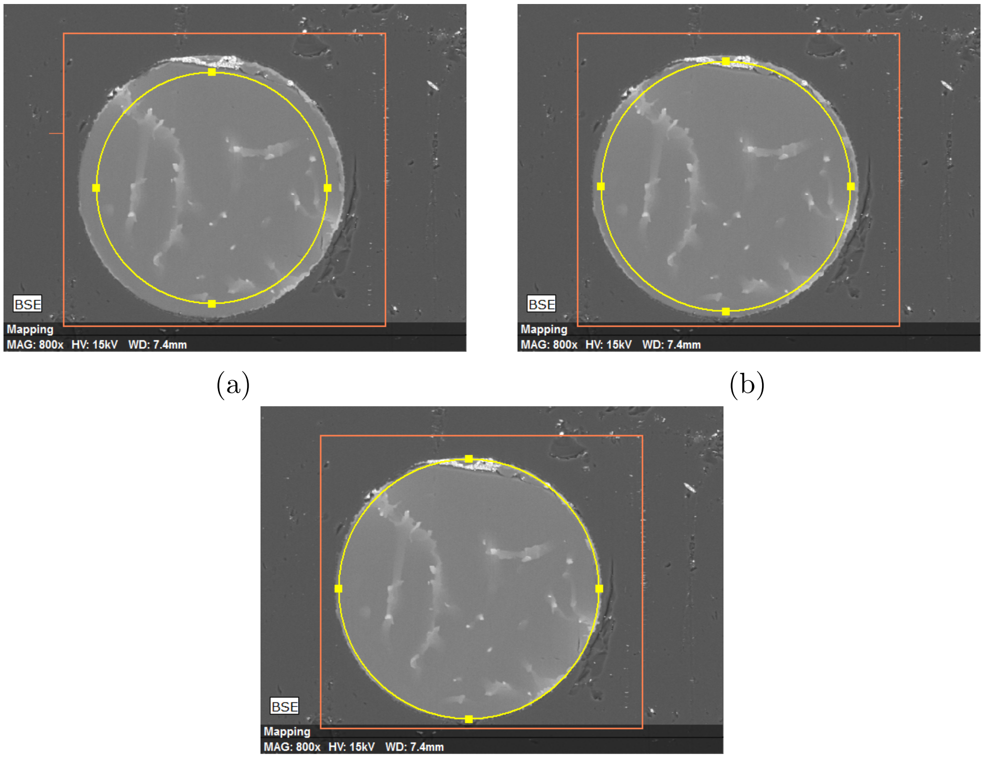
BSE
Mapping
MAG: 800x HV: 15kV WD: 7.4mm
BSE
Mapping
MAG: 800x HV: 15kV WD: 7.4mm
BSE
Mapping
MAG: 800x HV: 15kV WD: 7.4mm

(a) (b)

(c)

Figure C.1: BSE SEM micrographs of samples A (a), B (b) and C (c) with quantification area used in EDS marked by the yellow circles.

Appendix D

Critical Velocity of NAL

A baseline corrected intensity profile plot for NAL is presented in figure D.1. The ratio between the maximum and mminimum greyscale value in the melt is 1.10.

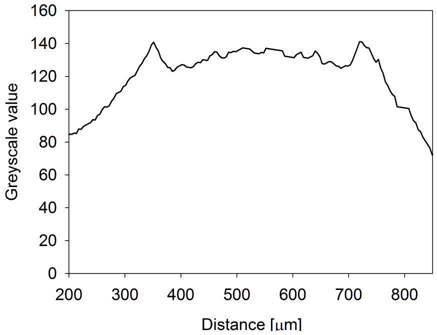

Figure D.1: Baseline corrected greyscale intensity plot across melt zone of the NAL sample.

The Ge-content of the fibre was determined, using EDS, as $41.36at\%$. Will assume the same recruitment range as for the Clemson fibres. The composition in the melt zone is calculated following the same assumptions as used as in section 4.1.3.1, giving a melt zone composition of 52.63%. Using equation 4.2, the interface temperature is then $1260°C$. The maximum temperature is determined, by using the same procedure as in section 4.1.3, to be 1363 °C. The melt zone length is approximately 420 µm, as the radius is 210 µm. This gives a thermal gradient in the liquid of approximately $2450\,°\mathrm{C\,cm^{-1}}$. The redistribution coefficient is then calculated using equation 2.10:

$$k = 0.37$$

The diffusion coefficient is:

$$D = 17.4 * 10^{-5}\mathrm{cm}^2\mathrm{s}^{-1}$$

Using equation4.4, the slope of the liquidus is calculated:

$$-790 * 0.5263 - 80 = -496.0$$

Using the values calculated above, equation 2.13 gives a critical growth velocity of:

$$v_c = 29.5\mu\mathrm{ms}^{-1}$$